Photoreaction and Proton Conduction of Graphene Oxide

March 2015

Kazuto Hatakeyama

Graduate School of Science and Technology

KUMAMOTO UNIVERSITY

PREFECE

Graphene is a monolayer of graphite structure and has excellent mechanical electrical optical properties. Because of these properties, Geim and Novoselov *et al.* got the Novel price in 2010. Graphene is produced by various methods such as epitaxial growth and chemical vapor deposition. In these methods, reduction of graphene oxide (GO) produced by exfoliation of graphite oxide is most inexpensive and easy route for mass production graphene. However, it is impossible to produce graphene with a perfect structure from GO.

GO, which is composed of hydrophobic π–conjugated sp^2 domains and sp^3 domains with hydrophilic oxygen functional groups, is not only a precursor for graphene but also one of the most promising materials because of its excellent properties such as high surface area, water solubility and tunable band gap. GO can be also produced very easily and cheaply from natural graphite as raw material. Therefore, GO has the potential to be key material for industrial applications in the future.

In this study, we report the photoreaction and proton conductivity of GO.

This thesis is composed of 7 chapters.

Chapter 1

Introduction

The general background, physical and chemical properties, synthesis of GO are described as introduction.

Chapter 2

Simple Photoreduction of Graphene Oxide Nanosheet under Mild Conditions

The photoreduction technique is demonstrated as new reduction method of GO. This method is very simple, easy and safety. It is investigated that the electron conductivity of GO rapidly increased through photoreduction. Moreover, it is possible to produce photopatterning a conducting section of micrometer size on insulating GO.

Chapter 3

Photoreaction of Graphene Oxide Nanosheets in Water

The photoreaction of GO in water is demonstrated. It is investigated that GO is reduced and H_2 and CO_2 are evolved from GO under UV irradiation in water. In addition, production of nanopores in GO through photoreaction process is observed. The mechanism of photoreaction of GO in water is also described.

Chapter 4

Photochemical Engineering of Graphene Oxide Nanosheets

Simple production of nanopores in GO via photoreaction in O_2 under UV irradiation at room temperature is reported. The total area of the nanopores can be controlled by irradiation time using this approach. The photoreaction mechanism in N_2 and O_2 is also described.

Chapter 5

Proton Conduction of Graphene Oxide

Proton conductivity of GO is described. It is demonstrated that GO is electronic insulator but, by contrast, has high proton conductivity. Optimization of proton conductivity in GO by filling sulfate ions is also presented. The mechanism of proton conductivity is discussed.

Chapter 6

Tunable Graphene Oxide Proton / Electron Mixed Conductor that Function at Room Temperature

The successful control of the proton and electron conductivities of GO using the photoirradiation and thermal reduction is presented. Both the electron and proton conduction mechanisms for GO are also discussed based on the concentrations of various functional groups and defects, changes in the interlayer distance, and the activation energy associated with proton conduction.

Chapter 7

Conclusions

In this chapter, the general conclusions of the thesis are described.

ACKNOWLEDGMENTS

I wish to express my sincerest thanks to Prof. Yasumichi Matsumoto, the professor of Kumamoto University, for his invaluable comments, suggestions stimulating discussions, inspiring guidance and encouragement through the course of the present investigation. I also wish to express gratitude to Prof. Michio Koinuma, Prof. Takaaki Taniguchi and Prof. Shinya Hayami at Kumamoto University. Their exact advices, valuable comments, stimulating discussions and great supports helped my work very much. I am deeply thanks to Ms. Kiyomi Tahara, office administrator in Matsumoto Lab., for their great continuing supports and helps.

I am greatly thanks to Prof. Yokoi Hiroyuki, Prof. Masahiro Hara, Prof. Seiji Kurihara, Prof. Toshihiro Ihara and Prof. Tetsuya Kida, the professors of Kumamoto University, for their stimulating discussions and critical comments. I also deeply thanks to Prof. Yutaka Kuwahara, Prof. Masayo Sakata, Prof. Hirotaka Matsuura and Prof. Yusuke Kitamura, at Kumamoto University, for their great helps. Dr. Mohammad Razaul Karim, at Shahjalal University, is thanked for his supports and helps very much.

I express my heartfelt thanks to Prof. Shintaro Ida, at Kyusyu University, Prof. Teppei Yamada, at Kyusyu University, Prof. Hiroshi Kitagawa, at Kyoto University, Prof. Noro Shinichiro, at Hokkaido University, Prof. Takayoshi Nakamura, at Hokkaido University, and Prof. Tomoyuki Akutagawa, at Tohoku University for their great supports.

I greatly acknowledge to Prof. T. Niidome, Prof. K. Nishiyama, Prof. M. Kunitake, Prof. S. Kim, Dr. A. Funatsu, Dr. K. Yamamuro, Dr. M. Morita, Mr. H. Tateishi, Mrs. C. Ogata, Mr. T. Sato, Mrs. Y. Onitsuka, Mr. Y. Watanabe, Mr. R. Motoda, Mr. S. Amano, Mr. Y. Kamei and Mr. K. Gezuhara for their helps.

Finally, I wish to express deep thanks to my family and friends for their support and hearty encouragement through my student life.

Kazuto Hatakeyama

March, 2015

CONTENTS

Chapter 1 Introduction 1

1.1 General background 1
1.2 Physical and chemical properties of GO 1
1.3 Synthesis of GO 2
References 3

Chapter 2 Simple Photoreduction of Graphene Oxide Nanosheet under Mild Conditions 7

2.1. Introduction.....7
2.2. Experiment.....7
2.3. Results and Discussion 9
2.4. Conclusions.....12
References.....13

Chapter 3 Photoreaction of Graphene Oxide Nanosheets in Water 23

3.1. Introduction.....23
3.2. Experiment.....23
3.3. Results and Discussion 25
3.4. Conclusions.....32
References.....31

Chapter 4 Photochemical Engineering of Graphene Oxide Nanosheets 45

4.1. Introduction.....45
4.2. Experiment.....45
4.3. Results and Discussion 46

4.4. Conclusions.....49
References.....50

Chapter 5 Proton Conduction of Graphene Oxide.....62

5.1. Introduction.....62
5.2. Experiment.....63
5.3. Results and Discussion 65
5.4. Conclusions.....69
References.....71

Chapter 6 Tunable Graphene Oxide Proton / Electron Mixed Conductor that Function at Room Temperature.....84

6.1. Introduction.....85
6.2. Experiment.....86
6.3. Results and Discussion 84
6.4. Conclusions.....90
References.....91

Chapter 7 Conclusions 107

Chapter 1

Introduction

1.1. General background

Graphene is a one of the carbon material made by monolayer of graphite structure (Figure 1-1a). Graphene is made out of carbon atoms arranged on a honeycomb structure made out of hexagons and can be thought of as composed of benzene rings stripped out from their hydrogen atoms[1-3]. This structure gives graphene unusual electronic properties such as the anomalous quantum Hall effect[4] and astonishing high carrier mobility at relatively high charge carrier concentrations and at room temperature[1, 5]. Graphene is produced by exfoliation of highly ordered pyrolytic graphite (HOPG)[1], epitaxial growth[6], chemical vapor deposition (CVD)[7]. Using these methods, it is possible to produce graphene with a relatively perfect structure and excellent properties. However, it is difficult to produce a large amount of graphene and need high cost in these methods[8]. Following this trend, reduction of graphene oxide (GO) produced by exfoliation of graphite oxide was reported by Ruoff et al. as new approach for production of graphene in 2007[9]. It is means that the history of GO has started as a precursor for graphene. Using this chemical method, a large amount of graphene can be easily produced at very low cost[8, 9]. However, it is well-known that reduced GO (rGO) has a lot of defect and excess oxygen function groups and is much different from graphene[8, 10].

Recently, GO has been considered as only a precursor for graphene but also one of the most promising materials because of its excellent properties such as photoluminescence[11, 12], ferromagnetism[13, 14], electrodes[15-18] and water permeation[19]. As it is now, it is said that GO has wider range of applications than graphene. GO has two important advantages: (1) it can be produced using inexpensive graphite as stating material by cost-effective chemical methods with a high yield, and (2) it is highly hydrophilic and can form stable aqueous colloids to facilitate the assembly of macroscopic structures by simple and cheap solution processes[8]. These advantages indicate that GO can be easily applicate and scale up to industrial level. Therefore, it is important for industrial development to study GO.

1.2. Physical and chemical properties of GO

GO is a one of the nanosheets. Figure 1-2 shows the AFM and TEM images of GO. Thickness of GO is generally about 1 nm, while their size is several micrometers[20, 21]. This ultimate 2D structure gives GO several advantages such as high surface area. The surface of GO is decorated by many oxygen functional groups such as epoxide, hydroxide, carbonyl and carboxide[8-10] (Figure 1-1b). Because of these oxygen functional groups, GO is highly hydrophilic and dissolves in water and other polar solvent, which facilitates some applications. GO is negatively charged in water solution because of their oxygen functional groups[8, 9]. Thus, positively charged species such as metal

cations, complex molecule and polymer can be assembled onto the surfaces of GO[17]. GO also has π–conjugated sp^2 domains similar to graphene. These sp^2 domains have high conductivity and are islands surrounded by an insulating matrix of the sp^3 domains with oxygen functional groups[8, 10]. GO has the band gap depending on the sp^2 domain size and acts as semiconductors[12, 13, 22]. rGO produced by several method such as thermal, chemical and photo reduction of GO is also promising materials[8]. rGO is good electron conductor and have a great potential for electric devices such as supercapacitor[18, 23]. Moreover, hydrophilic property, band gap and conductivity of GO is tunable via control of reduction degree[12, 24].

GO film can be produced easily and cheaply by depositing GO solutions by vacuum filtration, spraying, dip- or rod-coating and so on. It is reported that this GO film exhibits unique properties. For example, GO film is impermeable even for He gas under the low humid conditions, while it provide no barrier for water under the high humid conditions[19]. In addition, GO film act as molecular sieves allowing transport of small ions and blocking large ones[25] and gas separation membrane[26, 27]. GO film exhibits high proton conductivity, which indicate that GO film can be used as solid electrolyte for fuel cells[28].

1.3. Synthesis of GO

GO is produced by exfoliating graphite oxide[9]. In general, graphite oxide is synthesized by either the Hummers', Brodie's or Staudenmaier's method. Hummers' method is used more than other methods. In Hummers' method, $KMnO_4$ and H_2SO_4 are used as oxidizing agent. On the other hand, $KClO_3$ and HNO_3 are used as oxidizing agent in Brodie's and Staudenmaier's methods. There are some exfoliation methods of graphite oxide for production GO monolayer. In those exfoliation methods, ultrasonication of graphite oxide have been used extensively because it is easy, cheap and nontoxic.

References

1. Novoselov, K. S.; Geim, A. K.; Morozov, S. V.; Jiang, D.; Zhang, Y.; Dubonos, S. V.; Grigorieva, I. V.; Firsov, A. A., Electric Field Effect in Atomically Thin Carbon Films. *Science*, **306**, 666-669 (2004).
2. Geim, A. K.; Novoselov, K. S., The Rise of Graphene. *Nature Mater.*, **6**, 183-191 (2007).
3. Castro Neto, A. H.; Guinea, F.; Peres, N. M. R.; Novoselov, K. S.; Geim, A. K., The Electronic Properties of Graphene. *Rev. Mod. Phys.*, **81**, 109-162 (2009).
4. Novoselov, K. S.; Jiang, Z.; Zhang, Y.; Morozov, S. V.; Stormer, H. L.; Zeitler, U.; Maan, J. C.; Boebinger, G. S.; Kim, P.; Geim, A. K., Room-Temperature Quantum Hall Effect in Graphene. *Science*, **315**, 1379-1379 (2007).
5. Bolotin, K. I.; Sikes, K. J.; Jiang, Z.; Klima, M.; Fudenberg, G.; Hone, J.; Kim, P.; Stormer, H. L., Ultrahigh Electron Mobility in Suspended Graphene. *Solid State Commun.* , **146**, 351-355 (2008).
6. Berger, C.; Song, Z. M.; Li, X. B.; Wu, X. S.; Brown, N.; Naud, C.; Mayou, D.; Li, T. B.; Hass, J.; Marchenkov, A. N.; Conrad, E. H.; First, P. N.; de Heer, W. A., Electronic Confinement and Coherence in Patterned Epitaxial Graphene. *Science*, **312**, 1191-1196 (2006).
7. Kim, K. S.; Zhao, Y.; Jang, H.; Lee, S. Y.; Kim, J. M.; Ahn, J. H.; Kim, P.; Choi, J. Y.; Hong, B. H., Large-Scale Pattern Growth of Graphene Films for Stretchable Transparent Electrodes. *Natur*e, **457**, 706-710 (2009).
8. Pei, S. F.; Cheng, H. M., The Reduction of Graphene Oxide. *Carbon*, **50**, 3210-3228 (2012).
9. Stankovich, S.; Dikin, D. A.; Piner, R. D.; Kohlhaas, K. A.; Kleinhammes, A.; Jia, Y.; Wu, Y.; Nguyen, S. T.; Ruoff, R. S., Synthesis of Graphene-Based Nanosheets via Chemical Reduction of Exfoliated Graphite Oxide. *Carbon*, **45**, 1558-1565 (2007).
10. Koinuma, M.; Ogata, C.; Kamei, Y.; Hatakeyama, K.; Tateishi, H.; Watanabe, Y.; Taniguchi, T.; Gezuhara, K.; Hayami, S.; Funatsu, A.; Sakata, M.; Kuwahara, Y.; Kurihara, S.; Matsumoto, Y., Photochemical Engineering of Graphene Oxide Nanosheets. *J. Phys. Chem. C*, **116**, 19822-19827 (2012).
11. Pan, D.; Zhang, J.; Li, Z.; Wu, M., Hydrothermal Route for Cutting Graphene Sheets into Blue-Luminescent Graphene Quantum Dots. *Adv. Mater.*, **22**, 734-738 (2010).
12. Loh, K. P.; Bao, Q.; Eda, G.; Chhowalla, M., Graphene Oxide as a Chemically Tunable Platform for Optical Applications. *Nature Chem.*, **2**, 1015-1024 (2010).
13. Matsumoto, Y.; Koinuma, M.; Ida, S.; Hayami, S.; Taniguchi, T.; Hatakeyama, K.; Tateishi, H.; Watanabe, Y.; Amano, S., Photoreaction of Graphene Oxide Nanosheets in Water. *J. Phys. Chem. C*, **115**, 19280-19286 (2011).
14. Wang, Y.; Huang, Y.; Song, Y.; Zhang, X.; Ma, Y.; Liang, J.; Chen, Y., Room-Temperature Ferromagnetism of Graphene. *Nano Lett.*, **9**, 220-224 (2009).

15. Zhu, Y. W.; Murali, S.; Stoller, M. D.; Ganesh, K. J.; Cai, W. W.; Ferreira, P. J.; Pirkle, A.; Wallace, R. M.; Cychosz, K. A.; Thommes, M.; Su, D.; Stach, E. A.; Ruoff, R. S., Carbon-Based Supercapacitors Produced by Activation of Graphene. *Science*, **332**, 1537-1541 (2011).
16. Liang, Y. Y.; Li, Y. G.; Wang, H. L.; Zhou, J. G.; Wang, J.; Regier, T.; Dai, H. J., Co_3O_4 Nanocrystals on Graphene as a Synergistic Catalyst for Oxygen Reduction Reaction. *Nature Mater.*, **10**, 780-786 (2011).
17. Taniguchi, T.; Tateishi, H.; Miyamoto, S.; Hatakeyama, K.; Ogata, C.; Funatsu, A.; Hayami, S.; Makinose, Y.; Matsushita, N.; Koinuma, M.; Matsumoto, Y., A Self-Assembly Route to an Iron Phthalocyanine/Reduced Graphene Oxide Hybrid Electrocatalyst Affording an Ultrafast Oxygen Reduction Reaction. *Parti. Part. Syst. Charact.*, **30**, 1063-1070 (2013).
18. Matsumoto, Y.; Tateishi, H.; Koinuma, M.; Kamei, Y.; Ogata, C.; Gezuhara, K.; Hatakeyama, K.; Hayami, S.; Taniguchi, T.; Funatsu, A., Electrolytic graphene oxide and its electrochemical properties. *J. Electroanal. Chem.*, **704**, 233-241 (2013).
19. Nair, R. R.; Wu, H. A.; Jayaram, P. N.; Grigorieva, I. V.; Geim, A. K., Unimpeded Permeation of Water Through Helium-Leak-Tight Graphene-Based Membranes. *Science*, **335**, 442-444 (2012).
20. Matsumoto, Y.; Morita, M.; Kim, S. Y.; Watanabe, Y.; Koinuma, M.; Ida, S., Photoreduction of Graphene Oxide Nanosheet by UV-Light Illumination under H_2. *Chem. Lett.*, **39**, 750-752 (2010).
21. Matsumoto, Y.; Koinuma, M.; Kim, S. Y.; Watanabe, Y.; Taniguchi, T.; Hatakeyama, K.; Tateishi, H.; Ida, S., Simple Photoreduction of Graphene Oxide Nanosheet under Mild Conditions. *ACS Appl. Mater. Interfaces*, **2**, 3461-3466 (2010).
22. Eda, G.; Lin, Y. Y.; Mattevi, C.; Yamaguchi, H.; Chen, H. A.; Chen, I. S.; Chen, C. W.; Chhowalla, M., Blue Photoluminescence from Chemically Derived Graphene Oxide. *Adv. Mater.*, **22**, 505-509 (2010).
23. Wu, Z. S.; Parvez, K.; Feng, X. L.; Mullen, K., Graphene-Based In-Plane Micro-Supercapacitors with High Power and Energy Densities. *Nature Commun.*, **4**, 2487 (2013).
24. Hatakeyama, K.; Tateishi, H.; Taniguchi, T.; Koinuma, M.; Kida, T.; Hayami, S.; Yokoi, H.; Matsumoto, Y., Tunable Graphene Oxide Proton / Electron Mixed Conductor that Functions at Room Temperature. *Chem. Mater.*, **26**, 5598-5604 (2014).
25. Joshi, R. K.; Carbone, P.; Wang, F. C.; Kravets, V. G.; Su, Y.; Grigorieva, I. V.; Wu, H. A.; Geim, A. K.; Nair, R. R., Precise and Ultrafast Molecular Sieving Through Graphene Oxide Membranes. *Science*, **343**, 752-754 (2014).
26. Kim, H. W.; Yoon, H. W.; Yoon, S. M.; Yoo, B. M.; Ahn, B. K.; Cho, Y. H.; Shin, H. J.; Yang, H.; Paik, U.; Kwon, S.; Choi, J. Y.; Park, H. B., Selective Gas Transport Through Few-Layered Graphene and Graphene Oxide Membranes. *Science*, **342**, 91-95 (2013).
27. Li, H.; Song, Z. N.; Zhang, X. J.; Huang, Y.; Li, S. G.; Mao, Y. T.; Ploehn, H. J.; Bao, Y.; Yu, M.,

Ultrathin, Molecular-Sieving Graphene Oxide Membranes for Selective Hydrogen Separation. *Science*, **342**, 95-98 (2013).

28. Tateishi, H.; Hatakeyama, K.; Ogata, C.; Gezuhara, K.; Kuroda, J.; Funatsu, A.; Koinuma, M.; Taniguchi, T.; Hayami, S.; Matsumoto, Y., Graphene Oxide Fuel Cell. *J. Electrochem. Soc.*, **160**, F1175-F1178 (2013).

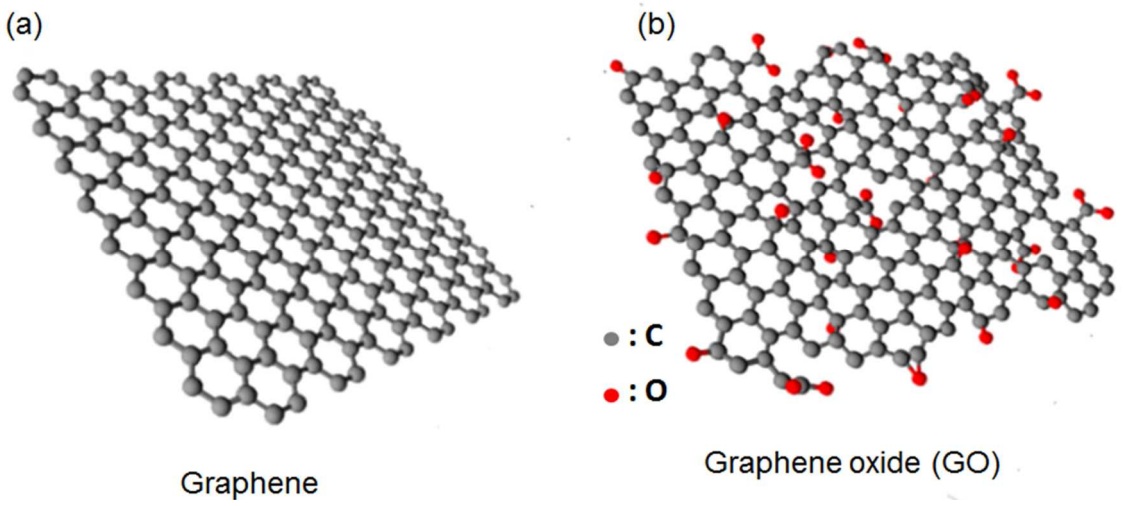

Figure 1-1. Schematic of (a) graphene and (b) GO.

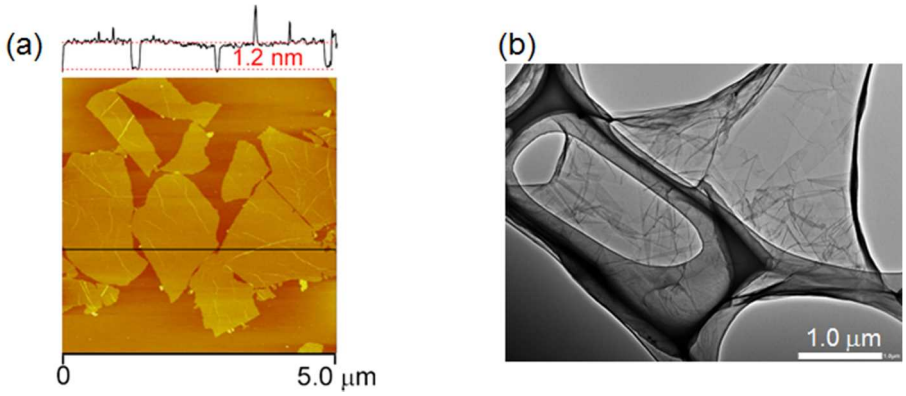

Figure 1-2. (a) AFM and (b) TEM images of GO.

Chapter 2

Simple Photoreduction of Graphene Oxide Nanosheet under Mild Conditions

2.1. Introduction

Graphene nanosheet is a promising material for some devices in many fields, because it has many excellent physical properteis[1-4]. Graphene nanosheet is produced by various processes[1, 5, 6]. The process via graphite oxide to prepare graphene or reduced graphene oxide (GO) nanosheet is very simple and has an ability to produce in large-scale in low cost[7-9]. Moreover, GO nanosheet can be used as a nanoparts to fabricate nanohybrid materials combined with other functional molecules by electrostatic principle[9] and/or reactive oxygenated functions existed at the surface[7-9]. GO nanosheet with low conductivity must be reduced to graphene or reduced GO nanosheet with high conductivity in order to be used practically in some devices with high conductivity. In this process, GO nanosheet is initially produced by exfoliation of graphite oxide, and then the GO nanosheet is generally reduced by hydrazine, heat treatment in a reducing environment[7], or TiO_2 and ZnO photocatalysis[10-12]. However, there are some disadvantages for these reduction processes. In the cases of the chemical and photocatalytic methods for reduction, heteroatomic and/or adsorbed impurities at the GO surface will be introduced. On the other hand, high temperature in the case of the heat treatment method will be sometimes undesirable for fabrication of devises. Thus, a development of more simple reduction process under mild conditions is desirable for extension in application of GO.

In this chapter, more simple reduction process of the GO under mild condition (room temperature) using light illumination in H_2 or N_2 without photocatalyst, and photopatterning using the present photoreduction process are demonstrated, together with a catalytic effect of Ag^+ on the photo-reduction, comparing with the GO reduced by traditional reduction technique using hydrazine. In the conduction of the reduced GO, a hopping and/or tunneling mechanism is proposed, where electron moves via sp^2 islands produced by reduction in sp^3 area of some epoxy and hydroxyl groups at the reduced GO surface[13, 14]. In this chapter, the conductivities of the GO reduced by the present method were also measured and discussed. As a result, the conductivity of the GO increased by 10^5~10^7 times by the present reduction process.

2.2. Experiment

Pure graphite (New Metals and Chemicals Ltd., 99.9999%) powder (0.5 g) was oxidized by Hummers' method[15] in which $NaNO_3$ (0.5 g), H_2SO_4 (23 mL), and $KMnO_4$ (3 g) were mixed in an ice bath and H_2O_2 solution (30%, 3 mL) and H_2O (40 mL, distilled water) were then added at a high temperature (35-95 °C). The resulting mixture was washed several times with distilled water and then dried in an oven. The resulting GO was suspended in distilled water (1.2 mg / mL),

sonicated in an ultrasonic bath for 2 h, and centrifuged to remove any aggregated GO. Exfoliated GO was collected in a vial (nanosheet suspension). Unless otherwise stated, the following five samples were irradiated for 2 h with light from a 500 W high-pressure Hg lamp where 99.99% H_2 or N_2 at 1 atm was flowed through a quartz cell containing the GO sample at a rate of about 50 mL / min. The light intensity was about 67 mW / cm^2, and the light source was positioned at a distance of about 40 cm from the sample surface. Samples 1 and 2 were aggregated GO nanosheet films that had been prepared by dropping the nanosheet suspension onto Pt metal and ITO glass substrates, respectively, and then drying them in a vacuum. Sample 1 was used for X-ray photoelectron spectroscopy (XPS) analysis because the Pt substrate has a high conductivity and contains very little oxygen on its surface, making it the most suitable substrate for this measurement. XPS (Sigma Probe, Thermo Scientific, US) was performed in a vacuum better than 10^{-7} Pa. The spectrometer is equipped with a monochromatized X-ray source (Al Kα, $h\nu$ = 1486.6 eV). Electrons emitted from the samples were detected by a hemispherical energy analyzer equipped with six channeltrons. The overall energy resolution for XPS was below 0.55 eV (on Ag $3d_{3/2}$ with a pass energy of 15 eV). The XPS peaks were deconvoluted using Gaussian components after Shirley background subtraction. Raman spectroscopy was performed using a micro Raman spectrometer (NRS-3100, Jasco, Japan) with a 532 nm excitation source at room temperature. Scanning electron microscopy (SEM) measurements were performed using a field-emission scanning electron microscope (Hitachi, SU-8000, Japan) at 5 kV in secondary electron imaging mode. Sample 2 was used for the photopatterning procedure because of the good adhesion between GO and the ITO substrate.

Sample 3 was a GO nanosheet film prepared by dipping a mica substrate into the nanosheet suspension. It was used for atomic force microscopy (AFM; Nanoscope V, Digital Instruments, US) measurements because it has a smooth atomic level surface and good adhesion between the film and the substrate. Almost all the nanosheets of samples prepared by dipping were single. Sample 4 was a GO nanosheet film prepared by dipping highly oriented pyrolytic graphite (HOPG; ZYB quality, NT-MDT) into the nanosheet suspension. It was used for conductivity measurements by conductive atomic force microscopy (C-AFM; Digital Instruments, Nanoscope V, US) using a Pt-Ir AFM tip. The *I-V* curves measured by this technique represent the conductivity perpendicular to a single nanosheet. HOPG is the most suitable substrate because the surface has a smooth atomic level surface and a high conductivity. HOPG was cleaved using scotch tape immediately prior to immersion. A twoelectrode system was used to measure the conductivities parallel to single and aggregated nanosheet films. Single GO and aggregated nanosheet films were prepared by dipping and dropping methods, respectively, using a glass substrate with two comb Au electrodes which were 90 nm thick and were separated by 2 μm. The electrode comb consisted of 60 pairs in the electrode bars (Figure 2-1). Sample 5 was the nanosheet suspension. The suspension was directly irradiated, and their UV-vis spectra (V-550, Jasco, Japan) were obtained before and after the

photoreduction in H_2. For hydrazine reduction, a GO suspended solution (10 mL) was loaded in a round-bottom flask, hydrazine hydrate (19.3 mmol) was added, and the solution was heated in an oil bath at 100 °C under a water-cooled condenser for 24 h. Over this time, the reduced GO gradually precipitated out as a black solid [8].

2.3. Results and Discussion

Figure 2-2 shows C (1s) XPS spectra of sample 1. The deconvoluted peak at a binding energy of 285 eV is attributed to C-C, C=C, and C-H bonds. The deconvoluted peaks centered in the binding energy ranges of 286.8-287.0, 287.8-288.0, and 289.0-289.3 eV are, respectively, attributed to the CO (COC and COH), C=O, and COOH oxygen-containing carbonaceous bands[8, 16, 17]. The peak intensities of the binding energies of oxygenated groups such as epoxy COC (which probably contains hydroxyl COH) decreased with the present photoreduction (Figure 2-2b-e), and the reduction degree increased with increasing irradiation time (Figure 2-2b,c). Similar photoreduction occurred even in N_2 (Figure 2-2d). These results suggest that mainly the COC epoxy bond is decomposed (probably with release of O_2) to produce sp^2 domains (islands) during light irradiation, because the COC peak intensity is mainly reduced by photoreduction. The result for GO treated by hydrazine is also shown to compare it with the present photoreduction treatment, where mainly COC is reduced on the basis of the reduction in the COC peak intensity (Figure 2-2f). There is an additional component at 285.9 eV, which corresponds to carbon in the C-N bonds[8, 18]. Thus, hydrazine treatment is very effective for the reduction. The XPS spectrum of the sample adsorbed with Ag^+ was measured after photoreduction; Ag^+ was adsorbed on GO nanosheets by immersing sample 1 in 0.04 M $AgNO_3$ solution and then washing it with water. Figure 2-2e shows the XPS spectrum of the Ag^+ adsorbed sample. Photoreduction of the GO nanosheet is promoted by the adsorbed Ag^+ (by comparing the two spectra of the 2 h irradiated samples shown in Figure 2-2b,e). Photoreduction occurred even when a UV cutoff filter (<420 nm) was used to generate visible light irradiation, although the degree of reduction was low. On the other hand, UV irradiation using a visible light cutoff filter (>390 nm) caused photoreduction with the same degree of reduction as when no filter was used. This demonstrates that UV irradiation is very effective in reducing GO nanosheets. Table 2-1 lists the peak area ratios of the oxygenated groups and the atomic ratios of O / C of all the samples. Although the degree in the reduction of GO using the present method was lower than those using the heat treatment method[7], it was almost the same as the cases using the photocatalytic reduction method[10] .

Epoxy groups are present on the basal planes of GO, and they are relatively unstable[9, 19]. In the reduction process, π-π^* excitation of electrons in sp^2 domains on the GO surface initially occurs during UV irradiation. The generated electron-hole pairs then move to the epoxy groups and break C-O-C bonds, releasing O_2 and forming relatively large sp^2 domains. Ag^+ may promote the

destruction of the C-O bond and/or O_2 release in the present photoreduction. Shen *et al.*[20] have reported that the reduction of GO proceeds with formation of Ag nanoparticles from Ag^+ under the presence of ethylene glycol and $NaBH_4$. They have suggested that the strong interaction may exist between the Ag nanoparticles and the remaining surface hydroxyl O atoms.

The usual characteristics of Raman spectra of carbon materials are the G band (~1580 cm^{-1}), which is generally attributed to the E_{2g} phonon of sp^2 atoms, and the D band (~1350 cm^{-1}), which is a breathing mode of κ-point phonons with A_{1g} symmetry[21, 22] and is attributed to local defects and disorder[23]. All the spectra contain the G and D bands. The Raman spectra shown in Figure 2-3 contain the G band at about 1603 cm^{-1} and the D band at about 1347 cm^{-1}. The ratio of the intensities of the D and G bands (I_D/I_G) are also presented in Table 2-1. I_D / I_G decreases from 1.12 to 1.02 and 1.03 after 2 h of photoreduction in H_2 and N_2, respectively. Since I_D/I_G is inversely proportional to the in-plane sp^2 domain size[21, 24], this result indicates the formation of relatively large sp^2 domains after photoreduction of the GO, which agrees well with the XPS results. Similar results have been reported for thermal and photocatalytic reduction processes[25, 26]. A greater reduction in I_D / I_G was observed when Ag^+ was adsorbed on the sample (0.98), which implies that Ag^+ has a catalytic effect during photoreduction. On the other hand, for reduction by hydrazine, the I_D / I_G ratio increased to 1.20, indicating that the sizes of sp^2 domains of graphene were reduced by hydrazine treatment[8]. The most remarkable feature in the Raman spectra of GO is the 2D band, and its position and shape can be used to distinguish the thickness of the films. As shown in Figure 2-4, all the samples had broad 2D bands at about 2704 cm^{-1}, indicating that the present GO films exist as multinanosheet layers[21, 27].

Figure 2-5 shows some typical AFM images of the nanosheets. The GO nanosheets were about 1.2 nm thick prior to photoreduction, whereas they were about 0.8 and 0.7 nm thick after photoreduction in H_2 for 2 and 5 h, respectively. All of the obtained values in the thickness contained about 20% errors. The thicknesses measured between the GO nanosheets and the substrate are almost the same as those of the GO single nanosheets reported already (about 1.0 nm)[8, 28]. This implies that almost all the GO and reduced GO nanosheets in sample 2-5 are single. The thicknesses measured between the nanosheets (measured in the overlapping region between the nanosheets) were about 1.0, 0.7, and 0.6 nm for samples before photoreduction and after photoreduction in H_2 for 2 and 5 h, respectively; these thicknesses are smaller than those stated above. This observation is in agreement with that reported by Fernandez *et al.*[29]. The GO nanosheet thickness increases with increasing degree of oxidation because oxygen containing functional groups at the graphene surface increase the nanosheet thickness[28, 29]. Consequently, the reduction in the nanosheet thickness by UV irradiation is due to photoreduction of the GO nanosheet.

Figure 2-6 shows *I-V* curves of the GO nanosheets (sample 4) measured by C-AFM. They represent the conductivity perpendicular to single GO nanosheets and the condition of the basal

plane but not the edge of the GO nanosheet. The currents are small due to the very small contact area of the Pt-Ir AFM tip (10-10^2 nm). The nanosheet conductivity increased dramatically on UV irradiation in H_2 (which is similar to a semimetal). The *I-V* curve of the reduced GO nanosheet (sandwich sample consisting of HOPG/nanosheet/ Pt-Ir AFM tip) was similar to that obtained when there was direct contact between HOPG and the Pt-Ir AFM tip. This implies that the conductivity of the reduced GO nanosheet is very high (especially at the basal plane but not at the edges). That is, the high conductivity is due to reduction of the epoxy group at the basal plane, as described above. On the other hand, the GO nanosheet was nearly insulating in the present applied voltage range. We were unable to distinguish between the conductivity of the sp^2 domain and that of the other oxygenated areas because these areas were much smaller (probably <10 nm^2) than the AFM tip.

Figure 2-7 shows *I-V* curves of nanosheet films prepared by (sample a) dipping a glass substrate with two Au electrodes into a nanosheet suspension and by (sample b) dropping the suspension onto the substrate. These *I-V* curves indicate the conductivities parallel to the GO nansoheets. Samples a and b, respectively, correspond to a single nanosheet and aggregated nanosheets (about 20 nm thick). AFM and SEM images of these samples are also shown in Figure 2-7. In sample a, some single nanosheets were deposited on the two Au electrodes. Consequently, the current in sample a was much smaller than that in sample b after photoreduction. Before photoreduction, the currents in both samples were less than about 0.1 pA at 1 V, whereas the currents were, respectively, about 50 nA and 20 μA for samples a and b after photoreduction (see Figure 2-7). The measured currents were almost the same for both samples photoreduced in H_2 and N_2. This indicates that the high conductivity is due to the destruction of C-O-C bonds in GO and the formation of relatively large sp^2 domains, but that it is not due to H addition (which may occur in H_2). The high conductivity of the reduced GO nanosheets is due to the increase in the sizes and numbers of sp^2 domains in the 2D carbon network on reduction; electron hopping occurs between sp^2 domains (islands) in the sp^3 matrix formed by the oxygenated groups on the basal plane[14]. The conductivities of the GO nanosheets reduced by the present technique were estimated to be higher than 10^3 Sm^{-1} if the conductivity of the GO increases by 10^5-10^6 times by the reduction from Figure 2-7, where the value of 0.0206 Sm^{-1} of GO powder[8] is used for the estimation. This value is almost in agreement with those of the GO nanosheets reduced by other techniques[28].

Photoreduction occurred even in the nanosheet suspension (sample 5). The suspension temperature did not change after photoreduction. The color of the suspension changed from light brown to black on photoreduction (see Figure 2-8a). Figure 2-8b shows UV-vis absorption spectra of the nanosheet suspensions. The black color and absorption in the visible region are due to the restoration of a sp^2 π-conjugated network[30] in the photoreduced GO nanosheets and their aggregation. AFM observations revealed that the nanosheets had various thicknesses ranging from 0.8 nm for a single nanosheet to 3 nm for aggregated nanosheets. Aggregation occurs due to the

hydrophobic interaction between the photoreduced nanosheets in water; in contrast, a sufficiently oxidized graphene nanosheet is hydrophilic[18, 31]. Figure 2-9 shows an XPS spectrum of the aggregated nanosheets after photoreduction for a sample prepared by dropping the suspension onto a Pt metal substrate. Photoreduction clearly reduces the intensities of the peaks at the binding energy of oxygenated groups. XPS analysis revealed that photoreduction in the suspension occurred for UV irradiation but not for visible light irradiation. These results reveal that photoreduction proceeds in the suspension only for UV irradiation.

Figure 2-10 shows photopatterning of sample 2. Figure 2-10a shows a schematic diagram of photopatterning using a carbon grid mesh as the photomask. Figure 2-10b shows SEM images of the photopatterned GO film. The white squares in the SEM images correspond to the irradiated GO surface that has a high conductivity. Thus, the present photoreduction process is very useful for photopatterning conductive areas of micrometer size on a GO nanosheet.

2.3. Conclusions

Photoreduction of GO nanosheet without a photocatalyst proceeded easily under UV irradiation in H_2 or N_2, and it increased the conductivity of the nanosheet. In particular, UV irradiation when adsorbed Ag^+ was present resulted in very effective photoreduction. XPS and Raman spectroscopy analysis revealed that epoxy groups attached to the interior of aromatic domains in the GO nanosheet are mainly destroyed by UV irradiation and that they form relatively large sp^2 islands; this gives rise to the high conductivity. *I-V* curves measured by C-AFM (perpendicular to a single nanosheet) and by a two-electrode system (parallel to a nanosheet) revealed that photoreduced GO nanosheets had high conductivities, whereas nonreduced GO was nearly insulating. Flash photopatterning of graphite oxide has been reported; it is quite different from our UV photoreduction process in principle because it is based on a photothermal effect (i.e., heat effect at temperatures higher than about 200 °C) obtained using a high power light source[32]. This is similar to the case of laser photopatterning in the mechanism, as stated in Introduction section. Our photoreduction process will be more useful because the nanosheet temperature increases by very little (the surface temperatures of films during photoreduction were lower than about 40 °C) and micrometer size photopatterning is possible. Moreover, as stated above, the present process is useful even in suspension with no temperature change. When there are no impurities present (i.e., with no Ag^+), the present photoreduction technique is very useful as a simple photopatterning process that uses mild conditions. It will, thus, extend the applications of GO in many fields.

References

1. Novoselov, K. S.; Geim, A. K.; Morozov, S. V.; Jiang, D.; Zhang, Y.; Dubonos, S. V.; Grigorieva, I. V.; Firsov, A. A., Electric Field Effect in Atomically Thin Carbon Films. *Science*, **306**, 666-669 (2004).
2. Geim, A. K.; Novoselov, K. S., The Rise of Graphene. *Nature Mater.*, **6**, 183-191 (2007).
3. Castro Neto, A. H.; Guinea, F.; Peres, N. M. R.; Novoselov, K. S.; Geim, A. K., The Electronic Properties of Graphene. *Rev. Mod. Phys.*, **81**, 109-162 (2009).
4. Bolotin, K. I.; Sikes, K. J.; Jiang, Z.; Klima, M.; Fudenberg, G.; Hone, J.; Kim, P.; Stormer, H. L., Ultrahigh Electron Mobility in Suspended Graphene. *Solid State Commun.*, **146**, 351-355 (2008).
5. Berger, C.; Song, Z. M.; Li, X. B.; Wu, X. S.; Brown, N.; Naud, C.; Mayou, D.; Li, T. B.; Hass, J.; Marchenkov, A. N.; Conrad, E. H.; First, P. N.; de Heer, W. A., Electronic Confinement and Coherence in Patterned Epitaxial Graphene. *Science*, **312**, 1191-1196 (2006).
6. Kim, K. S.; Zhao, Y.; Jang, H.; Lee, S. Y.; Kim, J. M.; Ahn, J. H.; Kim, P.; Choi, J. Y.; Hong, B. H., Large-Scale Pattern Growth of Graphene Films for Stretchable Transparent Electrodes. *Nature*, **457**, 706-710 (2009).
7. Pei, S. F.; Cheng, H. M., The Reduction of Graphene Oxide. *Carbon*, **50**, 3210-3228 (2012).
8. Stankovich, S.; Dikin, D. A.; Piner, R. D.; Kohlhaas, K. A.; Kleinhammes, A.; Jia, Y.; Wu, Y.; Nguyen, S. T.; Ruoff, R. S., Synthesis of Graphene-Based Nanosheets via Chemical Reduction of Exfoliated Graphite Oxide. *Carbon*, **45**, 1558-1565 (2007).
9. Dreyer, D. R.; Park, S.; Bielawski, C. W.; Ruoff, R. S., The Chemistry of Graphene Oxide. *Chem. Soc. Rev.*, **39**, 228-240 (2010).
10. Akhavan, O.; Ghaderi, E., Photocatalytic Reduction of Graphene Oxide Nanosheets on TiO_2 Thin Film for Photoinactivation of Bacteria in Solar Light Irradiation. *J. Phys. Chem. C*, **113**, 20214-20220 (2009).
11. Williams, G.; Seger, B.; Kamat, P. V., TiO_2-Graphene Nanocomposites. UV-Assisted Photocatalytic Reduction of Graphene Oxide. *ACS Nano*, **2**, 1487-1491 (2008).
12. Wu, Z. S.; Parvez, K.; Feng, X. L.; Mullen, K., Graphene-Based In-Plane Micro-Supercapacitors with High Power and Energy Densities. *Nature Commun.*, **4**, 2487 (2013).
13. Kaiser, A. B.; Gomez-Navarro, C.; Sundaram, R. S.; Burghard, M.; Kern, K., Electrical Conduction Mechanism in Chemically Derived Graphene Monolayers. *Nano Lett.*, **9**, 1787-1792 (2009).
14. Eda, G.; Lin, Y. Y.; Mattevi, C.; Yamaguchi, H.; Chen, H. A.; Chen, I. S.; Chen, C. W.; Chhowalla, M., Blue Photoluminescence from Chemically Derived Graphene Oxide. *Adv. Mater.*, **22**, 505-509 (2010).
15. Hummers, W. S.; Offemen, R. E., Preparation of Graphitic Oxide. *J. Am. Chem. Soc.*, **80**, 1339

(1958).

16. Shan, C. S.; Yang, H. F.; Song, J. F.; Han, D. X.; Ivaska, A.; Niu, L., Direct Electrochemistry of Glucose Oxidase and Biosensing for Glucose Based on Graphene. *Anal. Chem.*, **81**, 2378-2382 (2009).
17. Cao, L. Y.; Liu, Y. L.; Zhang, B. H.; Lu, L. H., In situ Controllable Growth of Prussian Blue Nanocubes on Reduced Graphene Oxide: Facile Synthesis and Their Application as Enhanced Nanoelectrocatalyst for H_2O_2 Reduction. *ACS Appl. Mater. Interfaces*, **2**, 2339-2346 (2010).
18. Becerril, H. A.; Mao, J.; Liu, Z.; Stoltenberg, R. M.; Bao, Z.; Chen, Y., Evaluation of Solution-Processed Reduced Graphene Oxide Films as Transparent Conductors. *ACS Nano*, **2**, 463-470 (2008).
19. Kim, S.; Zhou, S.; Hu, Y. K.; Acik, M.; Chabal, Y. J.; Berger, C.; de Heer, W.; Bongiorno, A.; Riedo, E., Room-Temperature Metastability of Multilayer Graphene Oxide Films. *Nature Mater.*, **11**, 544-549 (2012).
20. Shen, J. F.; Shi, M.; Li, N.; Yan, B.; Ma, H. W.; Hu, Y. Z.; Ye, M. X., Facile Synthesis and Application of Ag-Chemically Converted Graphene Nanocomposite. *Nano Res.*, **3**, 339-349 (2010).
21. Ferrari, A. C., Raman spectroscopy of graphene and graphite: Disorder, Electron-Phonon Coupling, Doping and Nonadiabatic Effects. *Solid State Commun.*, **143**, 47-57 (2007).
22. Ferrari, A. C.; Robertson, J., Interpretation of Raman Spectra of Disordered and Amorphous Carbon. *Phys. Rev. B*, **61**, 14095-14107 (2000).
23. Graf, D.; Molitor, F.; Ensslin, K.; Stampfer, C.; Jungen, A.; Hierold, C.; Wirtz, L., Spatially Resolved Raman Spectroscopy of Single- and Few-layer graphene. *Nano Lett.*, **7**, 238-242 (2007).
24. Cancado, L. G.; Takai, K.; Enoki, T.; Endo, M.; Kim, Y. A.; Mizusaki, H.; Jorio, A.; Coelho, L. N.; Magalhaes-Paniago, R.; Pimenta, M. A., General Equation for the Determination of the Crystallite Size L_a of Nanographite by Raman Spectroscopy. *Appl. Phys. Lett.*, **88** (2006).
25. Akhavan, O., Photocatalytic Reduction of Graphene Oxides Hybridized by ZnO Nanoparticles in Ethanol. *Carbon*, **49**, 11-18 (2011).
26. Akhavan, O.; Abdolahad, M.; Esfandiar, A.; Mohatashamifar, M., Photodegradation of Graphene Oxide Sheets by TiO_2 Nanoparticles after a Photocatalytic Reduction. *J. Phys. Chem. C*, **114**, 12955-12959 (2010).
27. Dato, A.; Radmilovic, V.; Lee, Z.; Phillips, J.; Frenklach, M., Substrate-Free Gas-Phase Synthesis of Graphene Sheets. *Nano Lett.*, **8**, 2012-2016 (2008).
28. Park, S.; Ruoff, R. S., Chemical Methods for the Production of Graphenes. *Nature Nanotechnol.*, **4**, 217-224 (2009).
29. Solis-Fernandez, P.; Paredes, J. I.; Villar-Rodil, S.; Martinez-Alonso, A.; Tascon, J. M. D.,

Determining the Thickness of Chemically Modified Graphenes by Scanning Probe Microscopy. *Carbon*, **48**, 2657-2660 (2010).

30. Li, D.; Muller, M. B.; Gilje, S.; Kaner, R. B.; Wallace, G. G., Processable Aqueous Dispersions of Graphene Nanosheets. *Nature Nanotechnol.*, **3**, 101-105 (2008).
31. Li, X. L.; Zhang, G. Y.; Bai, X. D.; Sun, X. M.; Wang, X. R.; Wang, E.; Dai, H. J., Highly Conducting Graphene Sheets and Langmuir-Blodgett Films. *Nature Nanotechnol.*, **3**, 538-542 (2008).
32. Cote, L. J.; Cruz-Silva, R.; Huang, J. X., Flash Reduction and Patterning of Graphite Oxide and Its Polymer Composite. *J. Am. Chem. Soc.*, **131**, 11027-11032 (2009).

Table 2-1. Peal area (A) ratios of oxygen-containing bonds to CC Bonds (obtained by XPS) and peak intensity ratios of I_D / I_G (obtained by Raman analysis)

	XPS				Raman
	$A_{C\text{-}O}/A_{CC}$	$A_{C=O}/A_{CC}$	A_{OCOH}/A_{CC}	O/C	I_D/I_G
Graphene Oxide	0.52	0.09	0.08	0.44	1.12
Photoreduction in H_2 for 2h	0.27	0.08	0.06	0.24	1.02
Photoreduction in H_2 for 5h	0.20	0.06	0.06	0.22	0.96
Photoreduction in N_2 for 2h	0.32	0.08	0.07	0.29	1.03
Ag^+ adsorption and photoreduction in H_2 for 2h	0.26	0.01	0.02	0.18	0.98
Reduction by Hydrazine	0.20	0.06	0.15	0.24	1.20

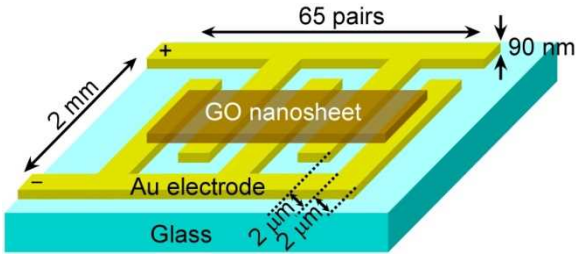

Figure 2-1. Electrode substrate model for determining the conductivity of a GO nanosheet film.

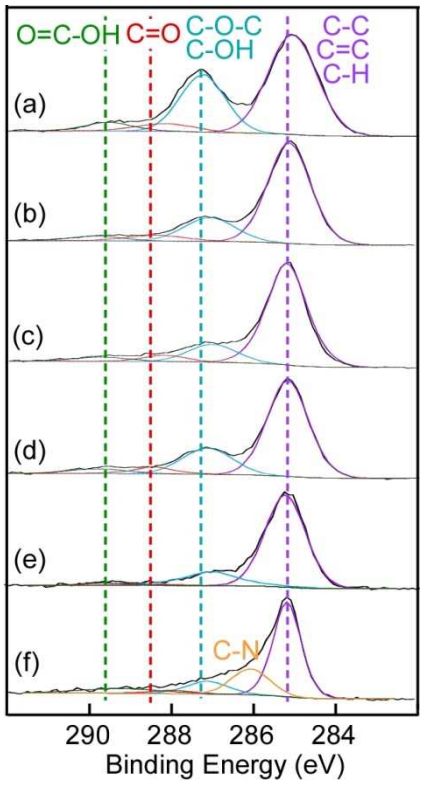

Figure 2-2. XPS spectra of C (1s) for aggregated nanosheet samples (sample 1): GO nanosheet (a) before photoreduction, (b) after photoreduction in H_2 for 2 h, (c) after photoreduction in H_2 for 5 h, and (d) after photoreduction in N_2 for 2 h. (e) Ag^+ adsorbed sample after photoreduction in H_2 for 2 h and (f) reduction by hydrazine. The substrate temperature was lower than 40 °C during photoreduction.

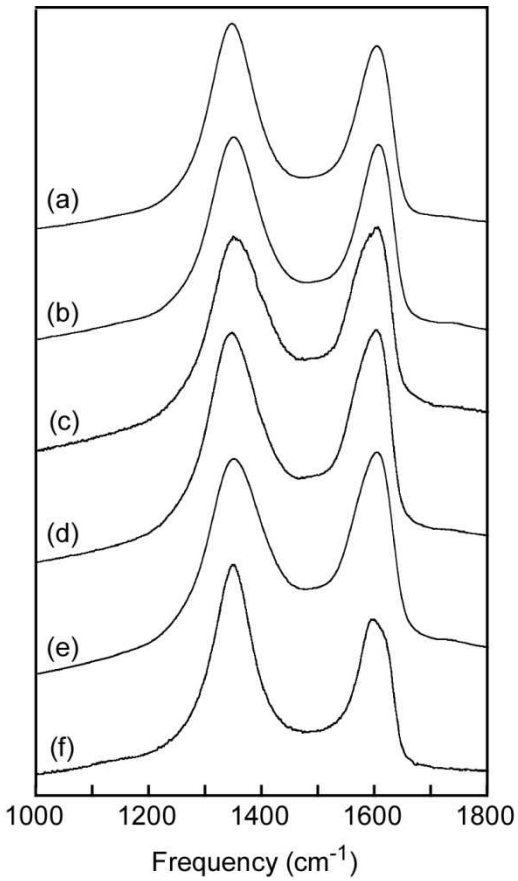

Figure 2-3. Raman spectra of aggregated nanosheet samples (sample 1): GO nanosheet (a) before photoreduction, (b) after photoreduction in H_2 for 2 h, (c) after photoreduction in H_2 for 5 h, and (d) after photoreduction in N_2 for 2 h. (e) Ag+ adsorbed sample after photoreduction in H_2 for 2 h and (f) reduction by hydrazine.

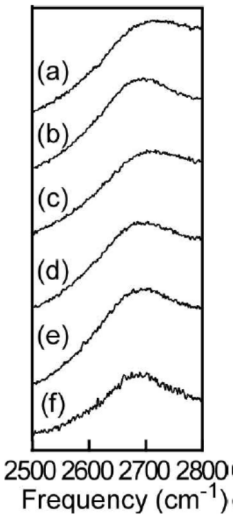

Figure 2-4. Raman spectra of 2D peaks of aggregated nanosheet samples (sample 1): GO nanosheet (a) before photoreduction, (b) after photoreduction in H_2 for 2 h, (c) after photoreduction in H_2 for 5 h, and (d) after photoreduction in N_2 for 2 h. (e) Ag+ adsorbed sample after photoreduction in H_2 for 2 h and (f) reduction by hydrazine.

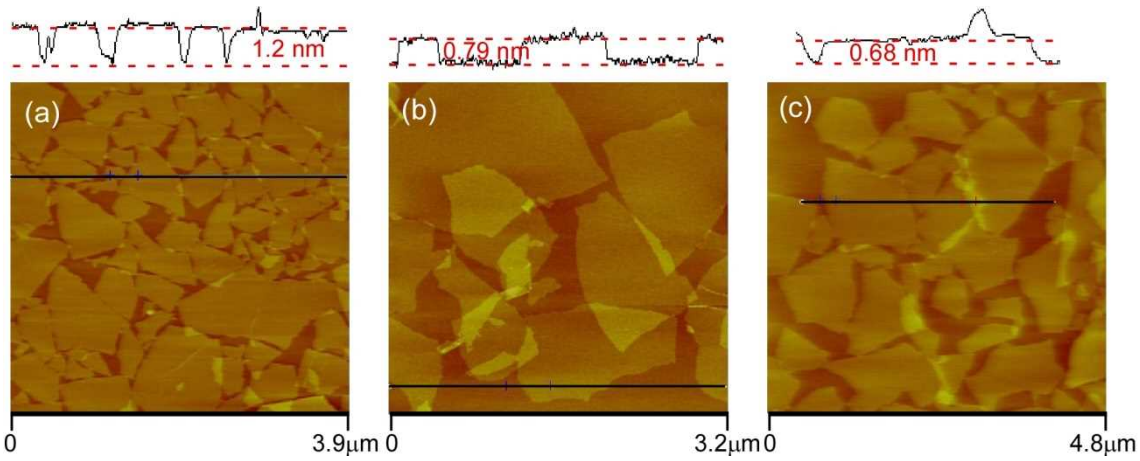

Figure 2-5. AFM images of single nanosheets (sample 3): (a) GO nanosheet, (b) after photoreduction in H_2 for 2 h, and (c) after photoreduction in H_2 for 5 h. Nanosheets a, b, and c are about 1.2, 0.8, and 0.7 nm thick, respectively.

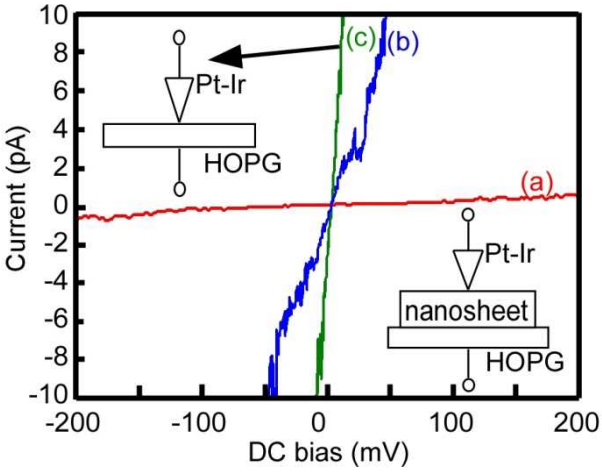

Figure 2-6. *I-V* curves of single nanosheets (sample 4): GO nanosheet (a) before and (b) after photoreduction in H_2 for 2 h and (c) HOPG. The conductivity increased dramatically after photoreduction in H_2.

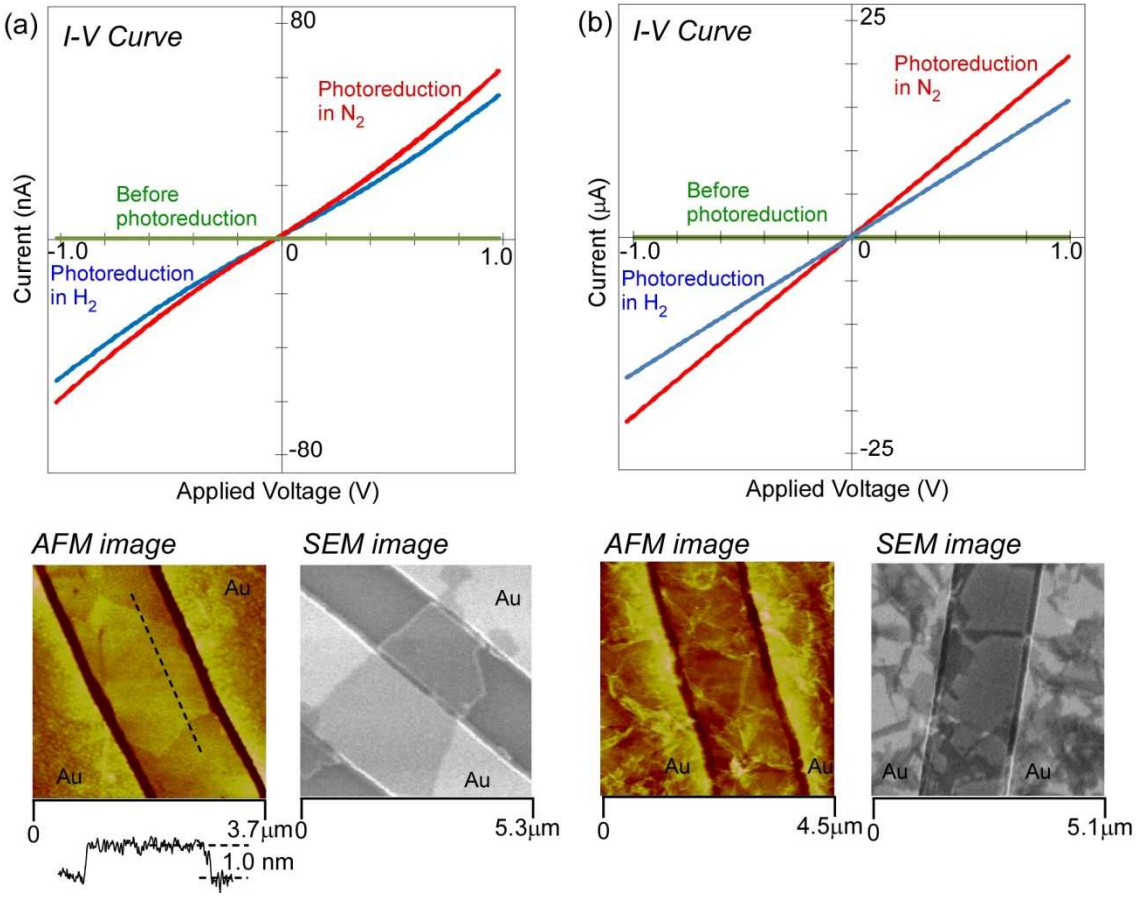

Figure 2-7. *I-V* curves and AFM and SEM images of GO nanosheets on a comb electrode: (a) single GO nanosheet and (b) aggregated GO nanosheets. Photoreduction increased the conductivities by about 10^5-10^7 times. The AFM and SEM images in (a) confirm the presence of a single GO nanosheet on the electrodes.

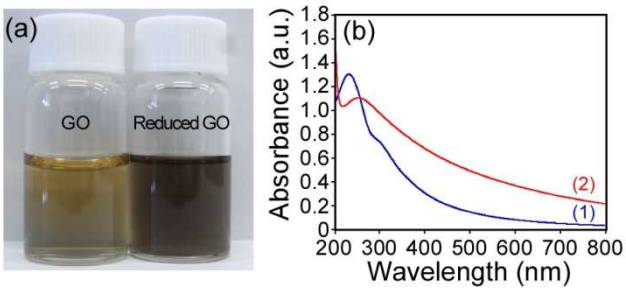

Figure 2-8. (a) Color depth and (b) UV-vis spectra of nanosheet suspensions (1) before and (2) after photoreduction in H_2 for 2 h (sample 5). Its color was black after photoreduction.

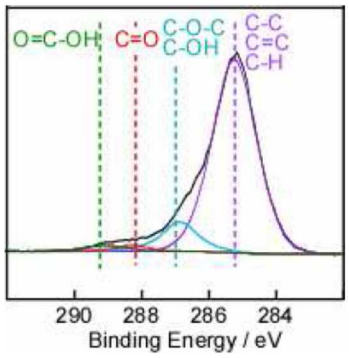

Figure 2-9. XPS spectrum of C(1s) of an aggregated nanosheet sample after photoreduction in suspension (sample 5): The peak intensities of the binding energies based on oxygenated groups are clearly reduced by photoreduction (compared with Figure 1a).

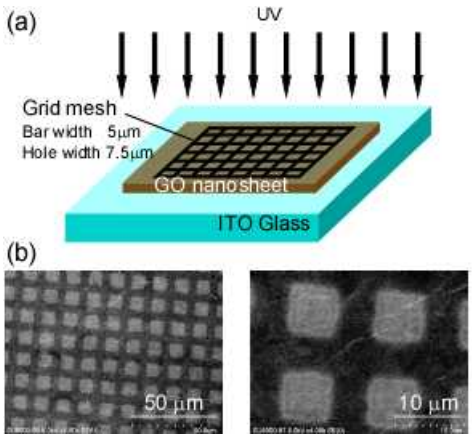

Figure 2-10. Photopatterning of GO nanosheets. (a) Schematic diagram of photopatterning and (b) SEM images of sample after photopatterning for 1h in H_2.

Chapter 3
Photoreaction of Graphene Oxide Nanosheets in Water

3.1. Introduction

Graphene nanosheets have many excellent physical properties[1-5] and thus have been intensively researched with a view to producing new devices in many fields. Graphene oxide (GO) nanosheets are another promising nanomaterial owing to their interesting chemical and physical properties including optoelectronic, fluorescence, and ferromagnetic properties[6-12], and GO nanosheets are suitable components for fabricating hybrid nanomaterials[13-15]. Mainly arising from the presence of oxygen-containing functional groups the properties of GO nanosheets can be controlled and tuned by reduction[9, 11, 12, 16-25], although doing so generates defects in the nanosheets[7, 17, 26-31].

Several models of GO nanosheets have been reported. They consist of two main regions[17, 32-34]: hydrophobic π-conjugated sp^2 domains and sp^3 domains with hydrophilic oxygen-containing functional groups. In GO nanosheets, the sp^2 domains have high conductivity and are islands surrounded by an insulating matrix of the sp^3 domains. The band gap of sp^2 domains depends on the domain size[6, 7, 34-36], whereas graphene nanosheets have zero band gap[5]. Thus, the sp^2 domains act as semiconductors and exhibit a photoresponse or photoreactivity when irradiated with light of energy exceeding their band gap. In other words, the sp^2 domains act as a photocatalyst under light (e.g., in the UV region); by photoexcitation, an electron is excited into the π^* conduction band and a hole is created in the π valence band. The electron and hole, respectively, contribute to reduction and oxidation of the GO nanosheets and water molecules. In this chapter, this new concept that GO nanosheets act as a semiconducting photocatalyst (bringing about photoreaction themselves) in water is demonstrated. Thus far, for semiconducting GO nanosheets in water, no fundamental photoreaction has been reported and no photoelectrochemical properties have been measured.

This chapter presents the photochemical properties of GO nanosheets and reports new photoreactions where H_2 and CO_2 are evolved from a suspension of GO nanosheets in water under UV irradiation. Reduced GO (rGO) nanosheets are formed after the photoreaction is run for 48 h. The rGO nanosheets have a unique morphology with many holes formed by the photoreaction and have ferromagnetic properties. Here, the features of the photoreaction or photocatalytic process involving GO nanosheets are investigated in detail.

3.2. Experiment

Graphite powder (98%) was purchased from Wako Ltd.; the 2% of impurities was oxygen according to X-ray photoelectron spectroscopy (XPS). The graphite power was oxidized by Hummers' method[37] using $NaNO_3$, H_2SO_4, $KMnO_4$, and H_2O_2 solutions. The resulting mixture was

washed several times with distilled water and dried in an oven. The produced graphite oxide was suspended in distilled water by bath sonication for 2 h, and the suspension was ultracentrifuged to remove aggregated GO nanosheets. The 99.999% graphite was compared with 98% graphite, and both graphite samples gave almost identical results; because 98% purity graphite was easier to exfoliate, all measurements were performed using GO nanosheets made from this graphite. The exfoliated GO nanosheets were collected in a vial as a nanosheet suspension with a concentration of 240 mg / L. Gas evolution tests were conducted using a mixture of 120 mL of water and 30 mL of nanosheet suspension. A quartz cell (400 mL) was used as the reaction chamber and irradiated with light from a 500 W Xe lamp (Ushio, SX-UI500XQ). The gas evolution rate from the reaction cell was measured by online gas chromatography (Shimadzu, GC-8A).

A GO nanosheet electrode for measuring the photoelectrochemical properties of the GO nanosheet was prepared by electrophoretic deposition of GO onto an ITO glass substrate, followed by drying under vacuum. In the electrophoretic deposition, a 10 V bias voltage was applied for 20 min at an electrode separation of 1 cm in the nanosheet suspension and GO was deposited onto the ITO anode (GO / ITO). Although electrodes with an ITO, a Pt, or a Au substrate perform similarly in photoelectrochemical tests, ITO was selected as the most suitable substrate because GO nanosheets strongly adhere to it. The photoelectrochemical properties were measured with a threeelectrode system consisting of working (GO / ITO), counter (Pt), and reference (Ag / AgCl) electrodes. A 0.1 M Na_2SO_4 solution in a quartz cell was used as the electrolyte. A high-pressure 500 W Hg lamp was used as the light source in the photoelectrochemical measurements.

XPS (Thermo Scientific, Sigma Probe) was used to analyze the surface of the GO nanosheets. The GO films were also analyzed by UV photoelectron spectroscopy (UPS) on the same system. A monochromatized X-ray source (Al Kα, $h\nu$ = 1486.6 eV) was used for XPS, and a discharge source (He I, $h\nu$ = 21.2 eV) was used for UPS. In this measurement, a Pt substrate (in GO/Pt film) was used to determine the Fermi level. To conduct Fourier transform infrared spectroscopy (FT-IR), a KBr disk containing GO or rGO sample was dried under vacuum and then scanned from 4000 to 750 cm^{-1} on an FT-IR spectrometer system (Perkin-Elmer, Spectrum One) in transmission mode. Raman spectroscopy (Jasco, NRS-3100) was performed using a 532 nm excitation source at room temperature. The GO nanosheet solutions and films were also analyzed by UVvis absorption spectroscopy (Jasco, V-550). To perform transmission electron microscopy (TEM; Hitachi, HF-2000, 200 kV), one drop of the aqueous nanosheet suspension was deposited on a holey carbon film. For atomic force microscopy (AFM; Digital Instruments, Nanoscope V, tapping mode), the samples were prepared by dipping a mica substrate into the aqueous nanosheet suspension. Model structures of GO were generated with CS Chem 3D Ultra 9.0 (Cambridge Soft) by molecular mechanics (MM2).

After performing the photoreduction test on the suspension, the reaction mixture was

passed through a polytetrafluoroethylene (PTFE) membrane filter with a pore size of 0.5 μm to obtain an rGO sample (about 1.0 mg) for magnetization measurements. Magnetization measurements were performed on a Quantum Design MPMS XL-5 superconducting quantum interference device (SQUID) magnetometer. A sample was placed in the SQUID chamber, and the field dependence of magnetization was measured at 2 and 300 K. To compare the magnetic properties of the present rGO sample with previously reported rGO samples, GO was reduced to a large extent by using hydrazine; the starting GO nanosheet suspension was the same for both reduction methods. Hydrazine hydrate was added to the nanosheet suspension, and then the mixture was heated in an oil bath at 100 °C in air for 24 h. A precipitate formed and was collected by filtration. The black solid was thoroughly washed with water and methanol and dried under vacuum. To analyze the metal contaminants in rGO, inductively coupled plasma atomic emission spectroscopy was performed using a CID plasma photoemission spectrophotometer (IRIS Advantage, Nippon Jarrell Ash). The samples were prepared by dissolving rGO in aqueous HNO_3 and then filtering the solution with a PTFE membrane filter.

3.3. Results and Discussion

Hydrogen Production by Photoreaction between GO and Water.

H_2 evolution from an aqueous suspension of GO nanosheets occurred when it was irradiated with light. Figure 1a shows the amount of H_2 evolution from a water suspension of GO nanosheets as a function of irradiation time. No H_2 evolution occurred in the dark. The amount of H_2 evolved decreased dramatically when a 390 nm cutoff filter was placed in front of the lamp (i.e., when only visible light (>390 nm) was used). The H_2 production rate increased with increasing irradiation time. Figure 3-1b shows the effect onH_2 production of reusing the GO nanosheets. In this test, nanosheets that had been used in the H_2 production test were reused after the suspension had been degassed; the lowest H_2 production rate (3×10^{-3} μmol / h) was observed in the first test, and the highest H_2 production rate (1.3×10^{-2} μmol / h) was observed in the third test.

Figure 3-2a, b, and c, respectively, shows XPS spectra, oxygen content, and FT-IR spectra before and after the photoreaction tests. The XPS peaks associated with oxygen-containing functional groups (especially epoxy groups, COC, and hydroxyl groups, COH) of the GO nanosheets decreased with increasing reaction time and disappeared at 48 h, indicating that the light-induced reduction proceeded smoothly. On the other hand, the peak due to the carboxy group disappeared only at 48 h. XPS analysis revealed that the O / C atomic ratio decreased from 0.48 (O, 32 atom% in virgin GO sample) to 0.10 (O, 9 atom% in rGO after photoreaction) as shown in Figure 3-2b. The FT-IR spectra in Figure 3-2c show results similar to the XPS results: the peaks associated with epoxy, hydroxyl, and carbonyl groups decreased or disappeared, but peaks associated with C=C[7, 9, 38] appeared at 48 h. Thus, the total π-conjugated sp^2 area (probably the number of sp^2 domains)

increased as a result of the present photoreduction.

On the other hand, the relative intensity of Raman peaks associated with defects (or sp^3 bonding, D band)[21, 39, 40] in the graphene sp^2 network (G band) decreased slightly after photoreduction (Figure 3-3). The rGO nanosheet mainly consisted of carbon and had a graphene-like structure with large defect areas. Figure 3-4 shows UV-vis absorption spectra measured from GO nanosheets suspended in water and reveals that the main excitation process for H_2 evolution involves UV and visible light. Almost all the absorption peaks can be attributed to π-π^* excitation in the π-conjugated sp^2 domains of the GO nanosheets[15, 35]. Consequently, H_2 evolution occurred via the photoreaction, based on π-π^* excitation, between water and defect carbons (at defects, edges, or both). On the other hand, the low H_2 production rate of the virgin sample is due to the dominant reduction of oxygen-containing functional groups (before degassing, Figure 3-1b).

Formation of defects in the graphene basal planes by thermal reduction of GO nanosheets (sometimes in conjunction with CO_2 evolution) has been predicted theoretically[21, 23, 24] and observed by high-resolution transmission electron microscopy[25]. H_2O molecules are known to be important in this reduction. Some defect carbons produced by thermal reduction are predicted to exist as carbonyl and ether groups[14, 21]. According to XPS and FT-IR analyses (Figure 3-2a and c), however, these groups were scarcely present in the rGO produced by the present photoreduction, in contrast to rGO produced by thermal reduction. After the photoreaction, the rGO nanosheets aggregated in the suspension, because their hydrophobicity increased. Using AFM and TEM, we observed morphologic changes before and after the photoreaction (Figure 3-5). The photoreduction resulted in the nanosheets being broken into smaller sheets and in many holes with ~20 nm radius being formed (Figure 3-5d). In other words, the present photoreaction produces many edges. This is another unique aspect of this photoreduction method. The GO nanosheets were about 1.2 nm thick before the photoreaction, whereas they were about 0.9 nm thick after the photoreaction was run for 48 h. A decrease in the oxygen-containing functional groups in the GO nanosheet brought about the decrease in film thickness[16, 31].

The present rGO nanosheets have many holes and therefore many edges. To evaluate the states of defect carbons in holes and edges of the rGO nanosheets, we measured the magnetic properties of rGO nanosheets after running the photoreduction for 48 h (Figure 3-6). Zero-field-cooled (ZFC) and field-cooled (FC) magnetization curves obtained at 100 Oe start to diverge at about 300 K, whereas no divergence was observed for the GO virgin sample (nearly zero magnetization). The contamination of metals such as 3d transition metals in the rGO was below the limit of detection (<0.001% in ICP-AES). Furthermore, the present rGO nanosheets exhibited magnetic hysteresis at 2 and 300 K (inset of Figure 3-6). No hysteresis was observed for the hydrazine-reduced rGO samples. Consequently, the ferromagnetic behavior is attributable to the photoreduction, not contamination. For a 1.0 mg rGO sample containing 0.001% Fe metal

(saturation magnetization, 220 emu/g) as an impurity, the magnetization would be about 2.2×10^{-6} emu in the present test, which is much smaller than the results shown in Figure 3-6 ($>5 \times 10^{-5}$ emu). Graphene generally has zigzag and armchair edges. Armchair edges have no localized spin because they consist of only π and π^* bands. On the other hand, the zigzag edges have localized spins because they have an antibonding flat band with π and π^* bands. Thus, the ferromagnetic behavior of the rGO nanosheets (there is a similar report for other rGO prepared by thermal annealing with hydrazine treatment[10]) produced by the photoreaction indicates that there are zigzag edges[41] and/or CH bonds[36, 42] in holes and / or edges.

Figure 3-7 shows a model of defect carbons in relatively small holes with a zigzag edge produced by photoreduction (CH bonds are not shown in this figure for clarity). Consequently, the ferromagnetic properties of the present rGO arise from the many holes formed and therefore the many zigzag edges.

No O_2 evolution occurred in the photoreaction. Therefore, we measured the amount of CO_2 generated under light irradiation. Figure 3-8 shows the amount of CO_2 as a function of irradiation time. The amount of CO_2 evolution was much higher than that of H_2 evolution, especially in the initial stage of the reaction, but the rate of CO_2 evolution levels off in the final stage. On the basis of the above results, we propose the following photoreaction mechanism for the initial stage; the epoxy group is chosen as a typical reactive species of the GO nanosheets.

$$\text{C-O-C (GO)} + H_2O + 2h+ \rightarrow \text{C (defect carbon)} + CO_2 + 2H^+ \quad (3\text{-}1)$$

$$\text{C-O-C (GO)} + 2H^+ + 2e^- \rightarrow \text{C-C (defect carbon)} + H_2O \quad (3\text{-}2)$$

In these reactions holes h^+ and electrons e^- are produced by π-π^*band UV excitation in the π-conjugated domains.

In the final stage, almost all the oxygen-containing functional groups have been reduced to defect carbons. The following H_2 production reaction is thought to occur at defect carbons because the H_2 production rate increases with increasing irradiation time (see Figure 3-1b).

$$2H_2O \text{ (or } H^+) + 2e^- \rightarrow H_2 + 2OH^- \text{ (at defect carbon)} \quad (3\text{-}3)$$

The defect carbons in the rGO nanosheets are considered important active sites since no H_2 evolution occurred when graphite powder was used. In this final stage, together with reaction 3-3, direct CO_2 production occurs via the following reaction involving defect carbons.

$$\text{C (defect)} + 2H_2O + 4h^+ \rightarrow CO_2 + 4H^+ \quad (3\text{-}4)$$

The rate of CO_2 production of reaction 4 is much lower than that of reaction 3-1 and will be similar to that of reaction 3-3. Thus, CO_2 evolution levels off (Figure 3-8) at long reaction times; reactions 3-3 and 3-4 in the final stage can be summarized by the following photoreaction of rGO under UV irradiation.

$$C + 2H_2O \rightarrow 2H_2 + CO_2 \quad (3\text{-}5)$$

Consequently, the above photoreactions, especially the CO_2 evolution reaction, result in formation of

many holes and defects. This is another unique aspect of this photoreaction process.

Photoelectrochemistry.

We measured the photoelectrochemical properties of the GO nanosheets to investigate the photoreaction mechanism in detail. Figure 3-9a shows current potential curves of GO nanosheet electrodes under chopped light irradiation. The GO electrodes produced clear anodic photocurrent and low cathodic photocurrent; the anodic photocurrent was always much greater than the cathodic photocurrent. The observed photocurrents originate from the GO film rather than the ITO substrate, because the ITO substrate generated only weak photocurrent (a few microamperes) and did not generate a cathodic photocurrent since ITO is an n-type semiconductor. The fact that the anodic photocurrent was much larger than the cathodic photocurrent suggests that the present GO nanosheets are closer to n-type semiconductors than p-type semiconductors. Because the number of electron carriers in the n-type conduction band is larger than the number of electron carriers produced by band gap excitation, the cathodic photocurrent is low. Thus, the present GO nanosheets act as n-type semiconductors in the photoelectrochemical test, although they have been reported to be p-type semiconductors based on the results of other measurements[20]. Figure 3-9b shows the anodic photocurrent at 0.8 V as a function of wavelength of monochromatic light. The onset wavelength for the photocurrent was about 450 nm, which corresponds to a band gap of about 2.8 eV in the GO nanosheets. The observed absorption spectrum (Figure 3-10) was similar to the photocurrent spectrum. Thus, the photocurrent is generated by UV irradiation, which is consistent with the photoreaction given above. A similar photocurrent and photocurrent spectrum (Figure 3-11) were also observed for rGO (after the photoreaction was run for 48 h in water), indicating that the semiconducting character of the sp^2 domains was been retained. However, the photocurrent decreased as a result of reactions 3-3 and 3-4, becoming relatively slow due to the small amount of oxygen in rGO; the changing potential of rGO (about 0.2 V) was more negative than that in Figure 3-9a.

After electrochemical reduction at 0.8 V and oxidation at 0.8 V under light irradiation for 20 min, the GO films were analyzed by XPS (Figure 3-12). The GO nanosheets on the electrode substrate were reduced to a small extent during electrophoretic deposition (Figure 3-12b)[43]. After photoelectrochemical reduction, the GO nanosheets were further reduced as indicated by the general reduction in the intensity of peaks corresponding to oxygen-containing functional groups such as the COC group (Figure 3-12c). A similar reduction occurred for the photoelectrochemically oxidized sample (Figure 3-12d). Thus, the samples photoelectrochemically reduced and oxidized under light irradiation were reduced by reactions 3-1 and 3-2, respectively. Consequently, the cathodic photocurrent is generated via reactions 3-2 and 3-3, whereas the anodic photocurrent is assigned to CO_2 production reactions 3-1 and 3-4. The changing potential from cathodic to anodic photocurrent corresponds to the flatband potential (E_{fb}) of the GO nanosheet semiconductor (Figure 3-9a). Figure

3-13 shows a plot of E_{fb} as a function of electrolyte pH. The pH dependence of E_{fb} had a gradient of about 60 mV / pH. This value is the same as that of the oxide semiconductor, indicating that oxygen-containing functional groups on the GO surface react with H^+ ions, OH ions, or both[44].

Figure 3-14 compares the UPS spectrum of platinum with the UPS spectra obtained by excitation with He I radiation ($h\nu$ = 21.2 eV) for the valence band of the GO nanosheets. The low-energy region of the UPS spectrum provides information about the energy of the top of the valence band in GO nanosheets relative to the Fermi level[45]. The top of the valence band corresponds to the π valence band consisting of various sp^2 domains. The UPS spectrum reveals that the top of the valence band of the GO nanosheet is shifted by about 2.0 eV relative to the Fermi level of platinum. Consequently, the energy difference between the Fermi level and the bottom of the π^* conduction band is estimated to be about 0.8 eV, assuming that the band gap is about 2.8 eV, as stated above.

From the above results, we estimated the energy positions of the bands of the semiconducting GO electrode; Figure 3-15 shows the band structure of the main sp^2 domains that produce the photocurrent and photoreaction. Although there are many sp^2 domains with various band gaps depending on their size, only the band structure of the main sp^2 domains responsible for the photocurrent and photoreaction is illustrated in this figure. A 2.8 eV band gap (calculated by time-dependent density functional theory using Gaussian basis sets) corresponds to a domain consisting of 3-7 aromatic rings[6]. Large domains probably have small band gaps where the energy positions of the conduction band (containing electrons excited by light) and the valence band (containing holes created by excitation of electrons into the conduction band) will be unsuitable for photoreactions.

To evaluate the photoreaction that produces H_2, a photoelectrolysis reaction was tested under a bias of 1.1 V, which is lower than the theoretical electrochemical decomposition voltage of water (1.23 V). Pt and GO nanosheet electrodes were, respectively, used as the cathode and anode in 0.1 M Na_2SO_4 solution. The GO nanosheet electrodes were continuously irradiated with light during electrolysis because no evolution of H_2 or CO_2 was observed in the dark. Figure 3-16 shows the amounts of H_2 and CO_2 evolution as a function of electrolysis time. The amount of H_2 was almost the same as that calculated from the current that flowed between the two electrodes (the current efficiency was about 90%), but no O_2 evolution was observed. In this case, H_2 evolution occurred at the Pt electrode (reaction 3-3) and CO_2 evolution occurred at the GO electrode (reactions 3-1 and 3-4). The H_2 / CO_2 molar ratio is expected to be 1 in the initial stage (reactions 3-1 and 3-3) and 2 in the final stage (reactions 3-3 and 3-4). The value would be about 1.5 in the initial stage if reaction 3-6 (for hydroxyl groups) in Figure 3-9 instead of reaction 1 (for epoxy groups) occurs. The experimental H_2 / CO_2 ratios were about 0.8 (14 h) and 1.4 (48 h) for the initial and final stages, respectively, which are close to the expected values; the experimental ratio must always be smaller

than 2 in the final stage because it includes the ratio in the initial stage. Consequently, the results from the photoelectrolysis test indicate that the above-mentioned photoreactions proceed during the photoreaction test.

3.4. Conclusions

We reported a new photoreaction of GO nanosheets that producesH_2 and CO_2 by reactions between GO and water under UV irradiation, where a photoprocess similar to that of semiconducting photocatalyst in the mechanism occurs. GO was reduced to rGO containing 9 atom% oxygen. The rGO nanosheets had many holes formed by CO_2 release from GO basal planes. This morphological change is a unique aspect of the rGO nanosheets prepared by the present photoreaction. The rGO nanosheets exhibited ferromagnetic behavior probably due to zigzag edges, CH bonding, or both in the many holes formed. Both anodic and cathodic photocurrents were observed for a GO nanosheet (GO / ITO) electrode. The energy positions of the π and π^* bands of the photoactive π-conjugated sp^2 domains were estimated from various photoelectrochemical results. The photoreaction was also investigated in terms of band energy position. In a photoelectrolysis test using a GO / ITO anode and a Pt cathode under light irradiation, H_2 evolution and CO_2 evolution, respectively, occurred at the GO / ITO and Pt electrodes, supporting the proposed mechanism of the photoreaction between GO nanosheets and water.

References

1. Novoselov, K. S.; Geim, A. K.; Morozov, S. V.; Jiang, D.; Zhang, Y.; Dubonos, S. V.; Grigorieva, I. V.; Firsov, A. A., Electric Field Effect in Atomically Thin Carbon Films. *Science*, **306**, 666-669 (2004).
2. Geim, A. K.; Novoselov, K. S., The Rise of Graphene. *Nature Mater.*, **6**, 183-191 (2007).
3. Lee, C.; Wei, X. D.; Kysar, J. W.; Hone, J., Measurement of the Elastic Properties and Intrinsic Strength of Monolayer Graphene. *Science*, **321**, 385-388 (2008).
4. Balandin, A. A.; Ghosh, S.; Bao, W. Z.; Calizo, I.; Teweldebrhan, D.; Miao, F.; Lau, C. N., Superior Thermal Conductivity of Single-Layer Graphene. *Nano Lett.*, **8**, 902-907 (2008).
5. Zhang, Y. B.; Tan, Y. W.; Stormer, H. L.; Kim, P., Experimental Observation of the Quantum Hall Effect and Berry's Phase in Graphene. *Nature*, **438**, 201-204 (2005).
6. Eda, G.; Lin, Y. Y.; Mattevi, C.; Yamaguchi, H.; Chen, H. A.; Chen, I. S.; Chen, C. W.; Chhowalla, M., Blue Photoluminescence from Chemically Derived Graphene Oxide. *Adv. Mater.*, **22**, 505-509 (2010).
7. Loh, K. P.; Bao, Q.; Eda, G.; Chhowalla, M., Graphene Oxide as a Chemically Tunable Platform for Optical Applications. *Nature Chem*., **2**, 1015-1024 (2010).
8. Eda, G.; Chhowalla, M., Chemically Derived Graphene Oxide: Towards Large-Area Thin-Film Electronics and Optoelectronics. *Adv. Mater.*, **22**, 2392-2415 (2010).
9. Eda, G.; Fanchini, G.; Chhowalla, M., Large-Area Ultrathin Films of Reduced Graphene Oxide as a Transparent and Flexible Electronic Material. *Nature Nanotechnol.*, **3**, 270-274 (2008).
10. Wang, Y.; Huang, Y.; Song, Y.; Zhang, X.; Ma, Y.; Liang, J.; Chen, Y., Room-Temperature Ferromagnetism of Graphene. *Nano Lett.*, **9**, 220-224 (2009).
11. Williams, G.; Kamat, P. V., Graphene-Semiconductor Nanocomposites: Excited-State Interactions between ZnO Nanoparticles and Graphene Oxide. *Langmuir*, **25**, 13869-13873 (2009).
12. Dreyer, D. R.; Park, S.; Bielawski, C. W.; Ruoff, R. S., The Chemistry of Graphene Oxide. *Chem. Soc. Rev.*, **39**, 228-240 (2010).
13. Wang, H. L.; Robinson, J. T.; Diankov, G.; Dai, H. J., Nanocrystal Growth on Graphene with Various Degrees of Oxidation. *J. Am. Chem. Soc.*, **132**, 3270-3271 (2010).
14. Wang, H. L.; Cui, L. F.; Yang, Y. A.; Casalongue, H. S.; Robinson, J. T.; Liang, Y. Y.; Cui, Y.; Dai, H. J., Mn_3O_4-Graphene Hybrid as a High-Capacity Anode Material for Lithium Ion Batteries. *J. Am. Chem. Soc.*, **132**, 13978-13980 (2010).
15. Karousis, N.; Economopoulos, S. P.; Sarantopoulou, E.; Tagmatarchis, N., Porphyrin Counter Anion in Imidazolium-Modified Graphene-Oxide. *Carbon*, **48**, 854-860 (2010).
16. Park, S.; Ruoff, R. S., Chemical Methods for the Production of Graphenes. *Nature Nanotechnol.*, **4**, 217-224 (2009).

17. Bagri, A.; Mattevi, C.; Acik, M.; Chabal, Y. J.; Chhowalla, M.; Shenoy, V. B., Structural Evolution During the Reduction of Chemically Derived Graphene Oxide. *Nature Chem.*, **2**, 581-587 (2010).
18. Stankovich, S.; Dikin, D. A.; Piner, R. D.; Kohlhaas, K. A.; Kleinhammes, A.; Jia, Y.; Wu, Y.; Nguyen, S. T.; Ruoff, R. S., Synthesis of Graphene-Based Nanosheets via Chemical Reduction of Exfoliated Graphite Oxide. *Carbon*, **45**, 1558-1565 (2007).
19. Cote, L. J.; Cruz-Silva, R.; Huang, J. X., Flash Reduction and Patterning of Graphite Oxide and Its Polymer Composite. *J. Am. Chem. Soc.*, **131**, 11027-11032 (2009).
20. Akhavan, O., The Effect of Heat Treatment on Formation of Graphene Thin Films from Graphene Oxide Nanosheets. *Carbon*, **48**, 509-519 (2010).
21. Williams, G.; Seger, B.; Kamat, P. V., TiO_2-Graphene Nanocomposites. UV-Assisted Photocatalytic Reduction of Graphene Oxide. *ACS Nano*, **2**, 1487-1491 (2008).
22. Pei, S. F.; Cheng, H. M., The Reduction of Graphene Oxide. *Carbon*, **50**, 3210-3228 (2012).
23. Shao, Y. Y.; Wang, J.; Engelhard, M.; Wang, C. M.; Lin, Y. H., Facile and Controllable Electrochemical Reduction of Graphene Oxide and Its Applications. *J. Mater. Chem.*, **20**, 743-748 (2010).
24. Zhang, Y. L.; Guo, L.; Wei, S.; He, Y. Y.; Xia, H.; Chen, Q. D.; Sun, H. B.; Xiao, F. S., Direct Imprinting of Microcircuits on Graphene Oxides Film by Femtosecond Laser Reduction. *Nano Today*, **5**, 15-20 (2010).
25. Ramesha, G. K.; Sampath, S., Electrochemical Reduction of Oriented Graphene Oxide Films: An in Situ Raman Spectroelectrochemical Study. *J. Phys. Chem. C*, **113**, 7985-7989 (2009).
26. Acik, M.; Mattevi, C.; Gong, C.; Lee, G.; Cho, K.; Chhowalla, M.; Chabal, Y. J., The Role of Intercalated Water in Multilayered Graphene Oxide. ACS Nano, 4, 5861-5868 (2010).
27. Sun, T.; Fabris, S.; Baroni, S., Surface Precursors and Reaction Mechanisms for the Thermal Reduction of Graphene Basal Surfaces Oxidized by Atomic Oxygen. *J. Phys. Chem. C*, **115**, 4730-4737 (2011).
28. Gomez-Navarro, C.; Meyer, J. C.; Sundaram, R. S.; Chuvilin, A.; Kurasch, S.; Burghard, M.; Kern, K.; Kaiser, U., Atomic Structure of Reduced Graphene Oxide. *Nano Lett.*, **10**, 1144-1148 (2010).
29. Bagri, A.; Grantab, R.; Medhekar, N. V.; Shenoy, V. B., Stability and Formation Mechanisms of Carbonyl- and Hydroxyl-Decorated Holes in Graphene Oxide. *J. Phys. Chem. C*, **114**, 12053-12061 (2010).
30. Matsumoto, Y.; Morita, M.; Kim, S. Y.; Watanabe, Y.; Koinuma, M.; Ida, S., Photoreduction of Graphene Oxide Nanosheet by UV-light Illumination under H_2. *Chem. Lett.*, **39**, 750-752 (2010).
31. Matsumoto, Y.; Koinuma, M.; Kim, S. Y.; Watanabe, Y.; Taniguchi, T.; Hatakeyama, K.; Tateishi, H.; Ida, S., Simple Photoreduction of Graphene Oxide Nanosheet under Mild Conditions. *ACS*

Appl. Mater. Interfaces, **2**, 3461-3466 (2010).

32. Kudin, K. N.; Ozbas, B.; Schniepp, H. C.; Prud'homme, R. K.; Aksay, I. A.; Car, R., Raman Spectra of Graphite Oxide and Functionalized Graphene Sheets. *Nano Lett.*, **8**, 36-41 (2008).
33. Mkhoyan, K. A.; Contryman, A. W.; Silcox, J.; Stewart, D. A.; Eda, G.; Mattevi, C.; Miller, S.; Chhowalla, M., Atomic and Electronic Structure of Graphene-Oxide. *Nano Lett.*, **9**, 1058-1063 (2009).
34. Lee, G.; Cho, K., Electronic Structures of Zigzag Graphene Nanoribbons with Edge Hydrogenation and Oxidation. *Phys. Rev. B*, **79**, 165440 (2009).
35. Kudin, K. N., Zigzag Graphene Nanoribbons with Saturated Edges. *ACS Nano*, **2**, 516-522 (2008).
36. Singh, A. K.; Yakobson, B. I., Electronics and Magnetism of Patterned Graphene Nanoroads. *Nano Lett.*, **9**, 1540-1543 (2009).
37. Hummers, W. S.; Offemen, R. E., Preparation of Graphitic Oxide. *J. Am. Chem. Soc.*, **80**, 1339 (1958).
38. Abdelsayed, V.; Moussa, S.; Hassan, H. M.; Aluri, H. S.; Collinson, M. M.; El-Shall, M. S., Photothermal Deoxygenation of Graphite Oxide with Laser Excitation in Solution and Graphene-Aided Increase in Water Temperature. *J. Phys. Chem. Lett.*, **1**, 2804-2809 (2010).
39. Ferrari, A. C.; Robertson, J., Interpretation of Raman Spectra of Disordered and Amorphous Carbon. *Phys. Rev. B*, **61**, 14095-14107 (2000).
40. Graf, D.; Molitor, F.; Ensslin, K.; Stampfer, C.; Jungen, A.; Hierold, C.; Wirtz, L., Spatially Resolved Raman Spectroscopy of Single- and Few-Layer Graphene. *Nano Lett.*, **7**, 238-242 (2007).
41. Nakada, K.; Fujita, M.; Dresselhaus, G.; Dresselhaus, M. S., Edge State in Graphene Ribbons: Nanometer Size Effect and Edge Shape Dependence. *Phys. Rev. B*, **54**, 17954-17961 (1996).
42. Zhou, J.; Wang, Q.; Sun, Q.; Chen, X. S.; Kawazoe, Y.; Jena, P., Ferromagnetism in Semihydrogenated Graphene Sheet. *Nano Lett.*, **9**, 3867-3870 (2009).
43. An, S. J.; Zhu, Y. W.; Lee, S. H.; Stoller, M. D.; Emilsson, T.; Park, S.; Velamakanni, A.; An, J. H.; Ruoff, R. S., Thin Film Fabrication and Simultaneous Anodic Reduction of Deposited Graphene Oxide Platelets by Electrophoretic Deposition. *J. Phys. Chem. Lett.*, **1**, 1259-1263 (2010).
44. Matsumoto, Y.; Yoshikawa, T.; Sato, E., Dependence of the Band Bending of the Oxide Semiconductors on pH. *J. Electrochem. Soc.*, **136**, 1389-1391 (1989).
45. Shaposhnikov, A. V.; Gritsenko, D. V.; Petrenko, I. P.; Pchelyakov, O. P.; Gritsenko, V. A.; Erenburg, S. B.; Bausk, N. V.; Badalyan, A. M.; Shubin, Y. V.; Smirnova, T. P.; Wong, H.; Kim, C. W., The Atomic and Electron Structure of ZrO_2. *J. Exp. Theor. Phys.*, **102**, 799-809 (2006).

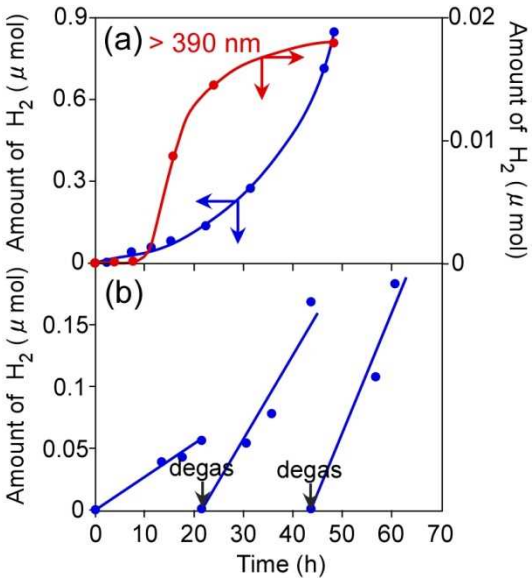

Figure 3-1. Amount of H_2 produced from a water suspension of GO nanosheets irradiated with light as a function of irradiation time with and without a 390 nm cutoff filter. (a) Amount of H_2 evolution and (b) amount of H_2 evolution after H_2 degassing (after photoreduction of GO nanosheet).

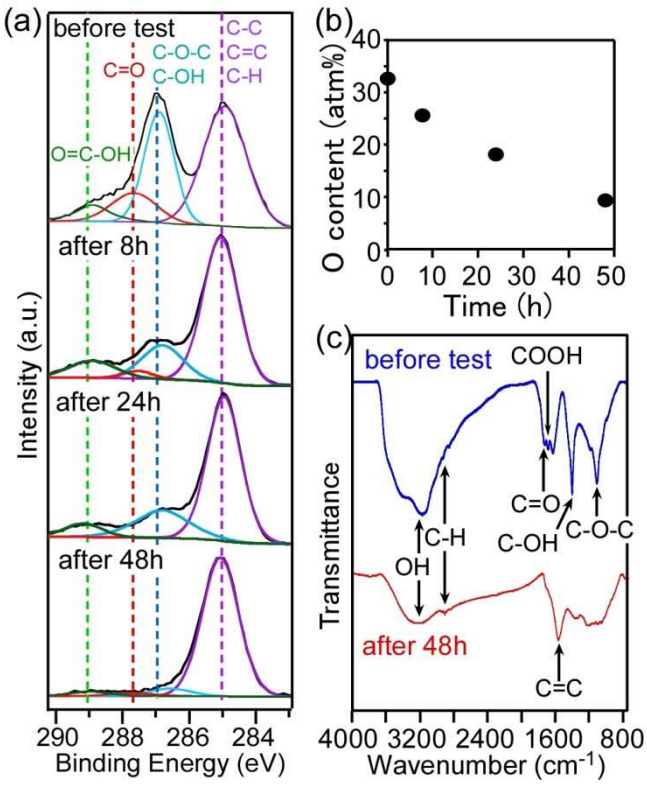

Figure 3-2. XPS spectra, oxygen content, and FT-IR spectra of GO nanosheet samples before (virgin sample) and after the photoreaction test (~48 h). (a) XPS spectra of C1s. (b) Oxygen content as a function of irradiation time. (c) FT-IR spectra. In the XPS spectra (a), the deconvoluted peak at a binding energy of 285 eV is attributed to C-C, C=C, and C-H bonds. The deconvoluted peaks centered in binding energy ranges of 286.8-287.1, 287.8-288.0, and 289.0-289.3 eV are attributed to CO (COC and COH), C=O, and COOH bands, respectively[18, 19, 43].

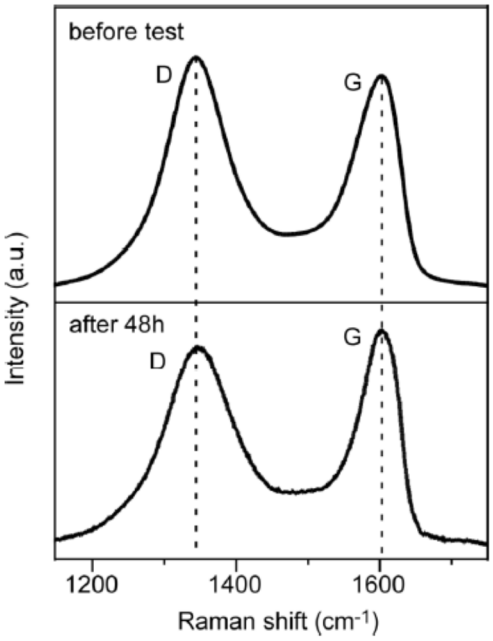

Figure 3-3. Raman spectra of GO nanosheets before and after 48 h photoreaction test. The relative intensity of Raman peaks associated with defects (or sp^3 bonding, D band) in the graphene sp^2 network (G band) decreases slightly after the photoreduction.

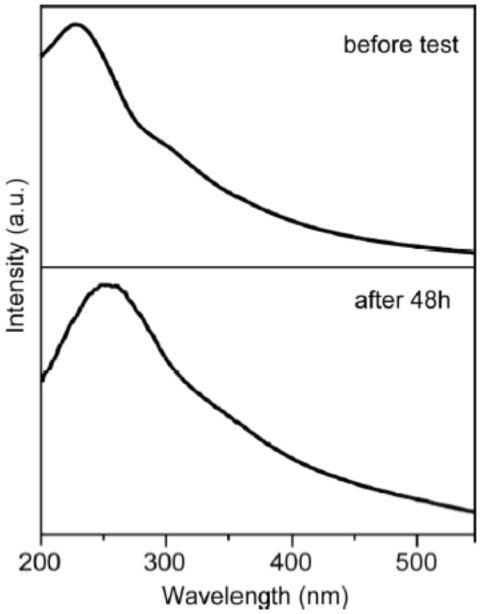

Figure 3-4. UV-vis absorption spectra of the GO nanosheet suspension obtained by subtracting adsorption of water from that of the suspension, before and after 48 h photoreaction test.

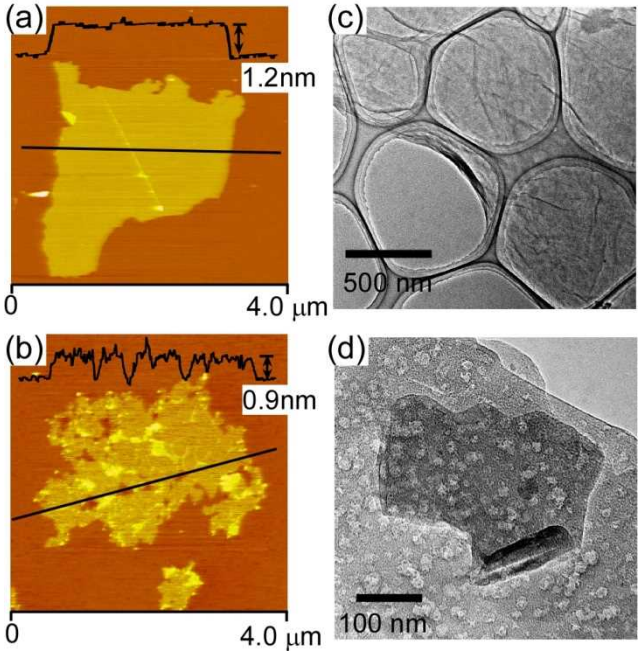

Figure 3-5. Surface morphology of GO and rGO nanosheets. AFM images and cross-sectional analysis of nanosheets (a) before and (b) after the photoreaction test (48 h). TEM images of nanosheets (c) before and (d) after the photoreaction test (48 h).

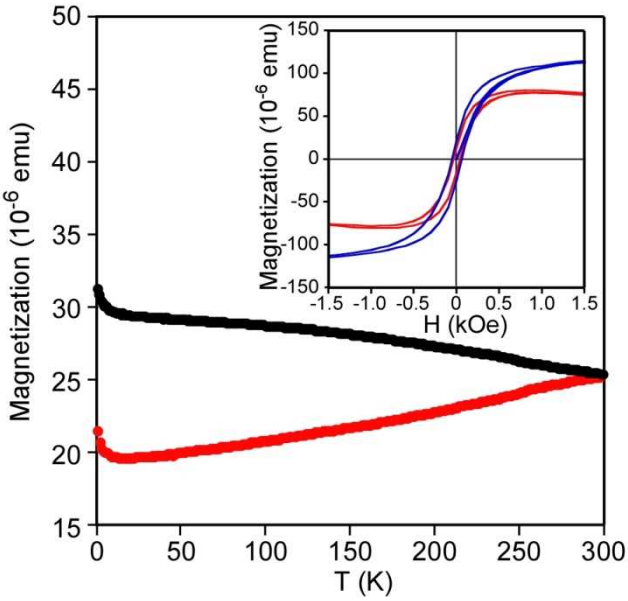

Figure 3-6. Magnetic properties of rGO prepared by photoreduction. Temperature dependence of ZFC (red dots) and FC (black dots) magnetizations acquired for rGO at 100 Oe. (Inset) Field dependence of the magnetizations of rGO at 2 (blue line) and 300 K (red line). Magnetic hysteresis loops are observed at both temperatures.

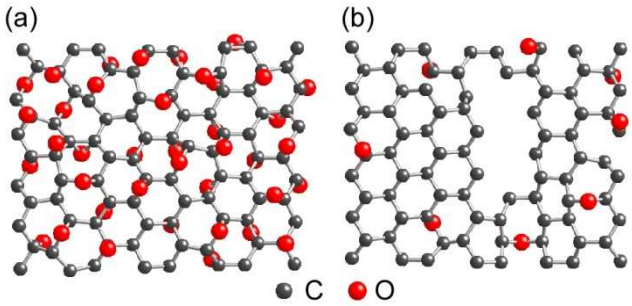

Figure 3-7. Structural models of nanosheet samples (a) before (virgin sample) and (b) after the photoreaction. Various oxygen-containing functional groups (especially epoxy COC and hydroxyl COH) were reduced to produce holes (defects) with zigzag edges.

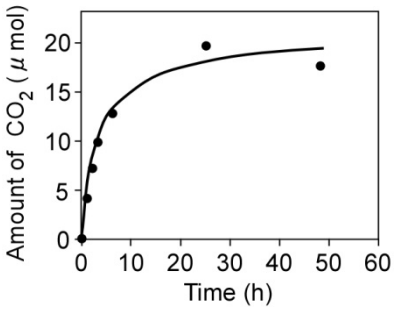

Figure 3-8. Amount of CO_2 produced form an aqueous suspension of GO nanosheets irradiated with light as a function of irradiation time.

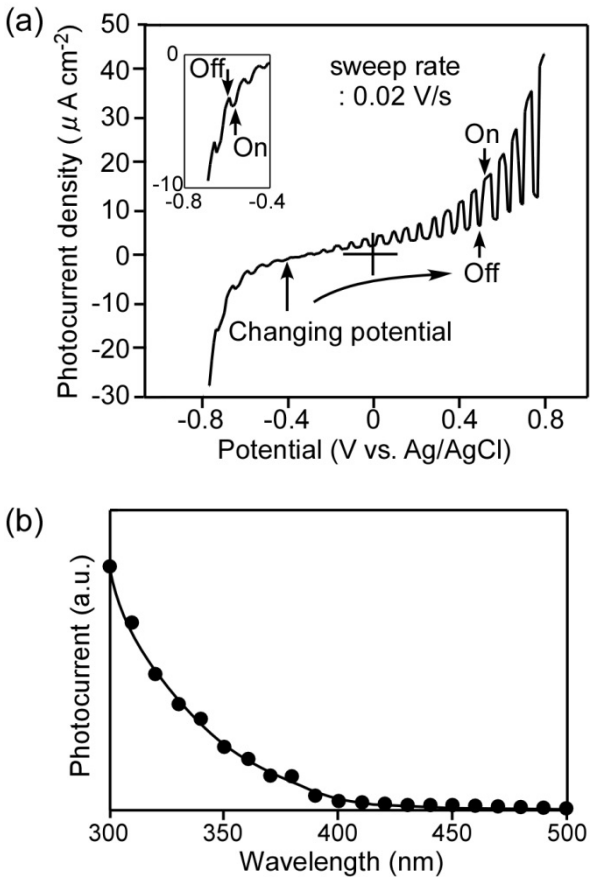

Figure 3-9. Photoelectrochemical tests of GO nanosheets. (a) Current-potential curve of GO nanosheet electrode under chopped light irradiation. (b) Anodic photocurrent (difference between dark current and current with irradiation) at +0.8 V as a function of the wavelength of monochromatic light.

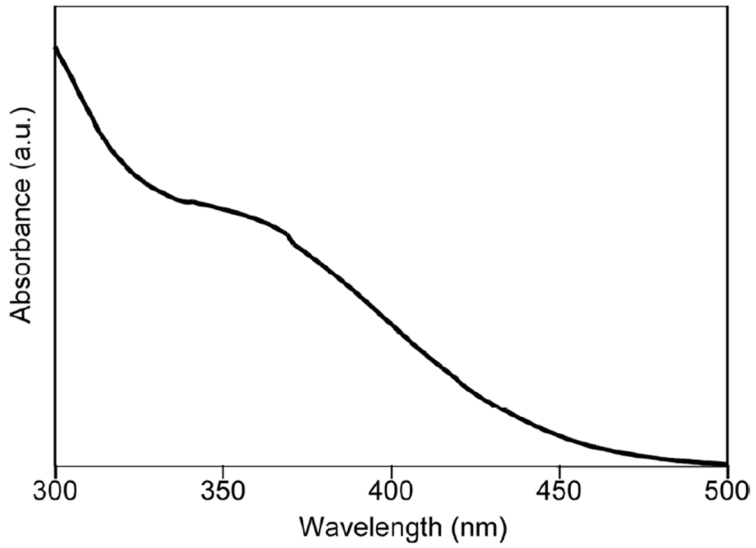

Figure 3-10. UV-vis sdsorption spectrum of the GO nanosheet electrode (GO / ITO) obtained by subtracting adsorption of the ITO substrate from that of GO / ITO.

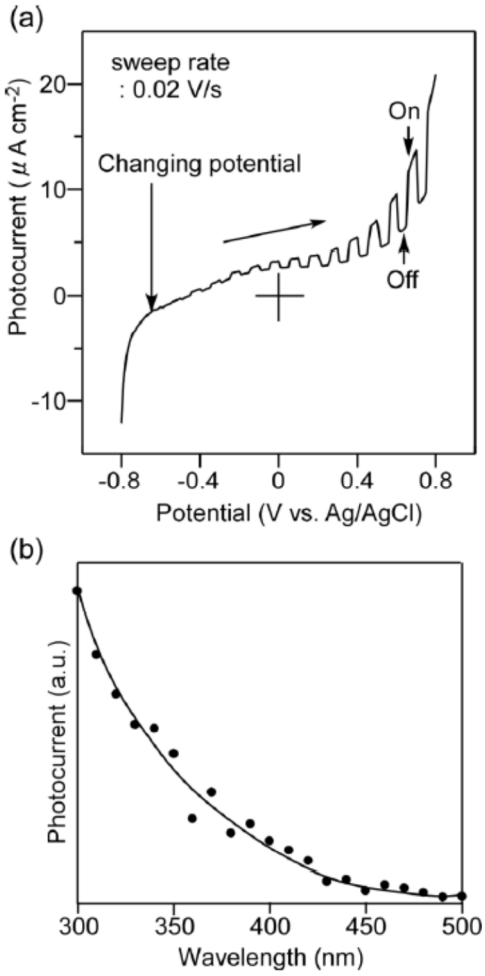

Figure 3-11. Photoelectrochemical tests of rGO nanosheets (rGO / ITO electrode). (a) Current-potential curve of rGO nanosheet electrode under chopped light irradiation. (b) Anodic photocurrent (difference between dark current and current with irradiation) at +0.8 V as a function of wavelength of irradiated monochromatic light.

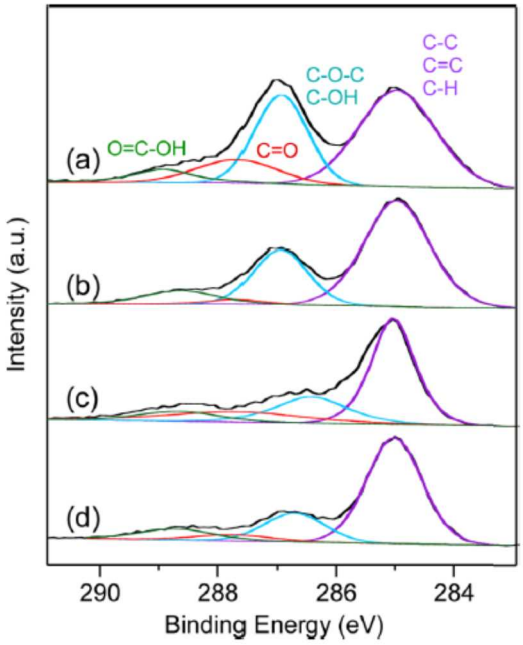

Figure 3-12. XPS spectra of C1s at the GO / ITO electrodes. (a) Virgin GO sample. (b) Sample after electrophoretic deposition. (c) After electrolysis for 20 min under irradiation at -0.8 V vs. Ag / AgCl. (d) After electrolysis for 20 min under irradiation at 0.8 V vs. Ag / AgCl.

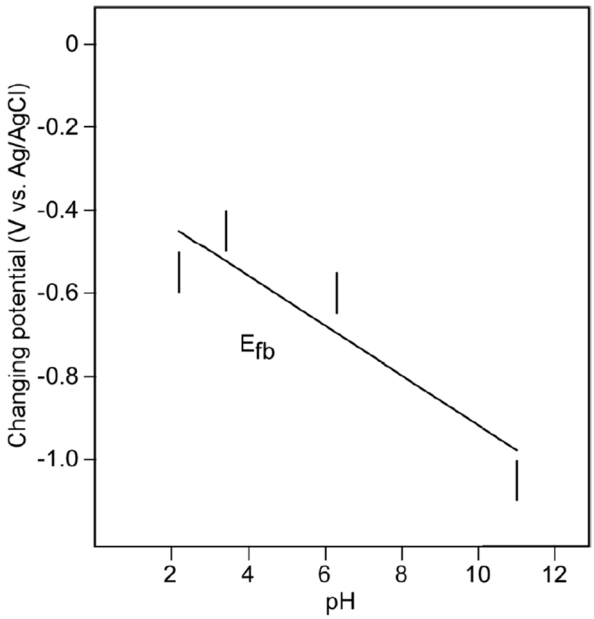

Figure 3-13. pH dependence of E_{fb} for the GO nanosheet electrode. E_{fb} corresponds to the potential changing from the cathodic and anodic photocurrents in Figure 7a. The pH was adjusted by adding H_2SO_4 or NaOH to the Na_2SO_4 electrolyte.

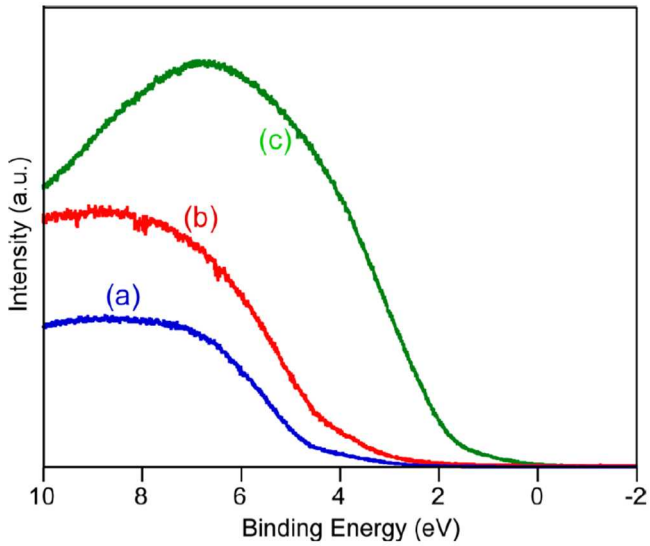

Figure 3-14. UPS spectra (obtained using He I radiation with $h\nu = 21.2$ eV) of the valence band of the GO nanosheets (GO / Pt). (a) Virgin GO nanosheet. (b) rGO nanosheet. (c) platinum for calibration. The low-energy region of the UPS spectrum provides information about the energy positions of the top of the valence band of GO and rGO nanosheets.

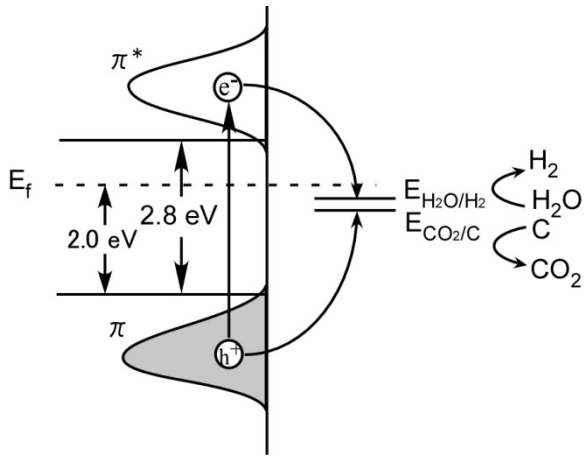

Figure 3-15. Energy diagram of the bands of GO nanosheets (π-conjugated sp^2 domains consisting of 3-7 aromatic rings). Equilibrium potentials $E_{H2O/H2}$ and $E_{CO2/C}$ ($C + 2H_2O \rightarrow CO_2 + 4H^+ + 4e^-$) were calculated to be -0.57 and -0.36 V vs Ag / AgCl, respectively.

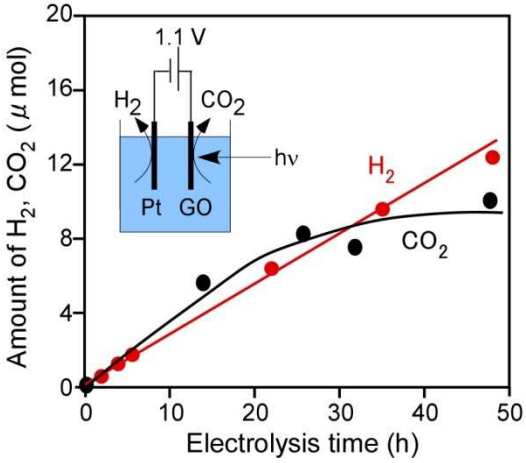

Figure 3-16. Amounts of H_2 and CO_2 evolution during photoelectrolysis. In the photoelectrolysis test, H_2 evolution and CO_2 evolution, respectively, occurred at the Pt cathode and the GO / ITO anode (2 cm^2) under a bias of 1.1 V in 0.1 M Na_2SO_4 when the anode was irradiated with light.

Chapter 4
Photochemical Engineering of Graphene Oxide Nanosheets

4.1. Introduction

Graphene Oxide (GO) nanosheets have interesting properties such as photoluminescence[1, 2], ferromagnetism[3-5], electrodes[6-8], and water permeation[9]. Reduced graphene oxide (rGO) nanosheets are highly conductive and can be used in various electrical devices. They are prepared from GO nanosheets by various reduction methods, such as thermal and hydrazine treatments[10-12]. Simple photoreduction methods using UV light at room temperature have also been developed[13, 14]. Irradiation in water produces many nanopores and results in ferromagnetic properties, which arise from the edges of the pores and small broken pieces of rGO[4].

The production of nanopores in conductive graphene and rGO is particularly interesting because the nanopores can be used for DNA sequencing[15, 16]. The GO film can also be used for gas separation, which can be controlled by the size of the nanopore[17, 18]. The production of many nanopores creates a highly specific surface, known as porous GO, which may have interesting properties for catalysts and sensors. There are few studies on the production of nanopores or porous GO[4]. Although the number and type of oxygenated groups have been altered by changing the conditions of the photoreduction process, they have never been quantitatively analyzed in GO and rGO. Here, we present a fast, simple photoreaction method to produce porous GO for short time which contains many nanopores.

Recently, GO and rGO have been well-known as an excellent amphiphilic soft material due to its oxygenated groups[19, 20] and these materials can be adopted for applications including proton conductors[21-24] and supercapacitors[25-28]. However, proton conduction of GO have been unexplored yet. Although there have been a few reports on the fabrication of GO/Nafion nanocomposites[21-23], the proton transport properties of the resultant materials is mainly perpendicularly affected to the basal plane of GO. In this work, we also demonstrate that proton conduction at the basal plane occurred through epoxide groups, and quantitatively analyze the oxygenated groups during the photoreaction process.

4.2. Experiment

The GO was prepared using Hummers' method[29]. The degree of GO oxidation was controlled by the amount of $KMnO_4$ used and the oxidation time (Figure 4-1). The suspension was diluted with pure water, placed on mica, and then dried under vacuum. A 500 W high-pressure mercury lamp was used to irradiate the samples at room temperature. The surfaces of the GO single nanosheets were observed using atomic force microscopy (AFM; Digital Instruments, Nanoscope V). The composition of the oxygenated groups was analyzed by X-ray photoelectron spectroscopy (XPS;

Thermo Scientific, Sigma Probe). The calibration curve for the quantitative analysis of the oxygen atomic percent (O / (C+O)) from the C1s binding peak areas was obtained using GO or rGO on a Pt substrate during photoreduction, which was controlled by the irradiation time. After the GO photoreaction, the XPS measurements were carried out on the glass substrates. The surface charging in the XPS measurements was compensated for using an electron flood gun. The DC current and the AC resistance of the GO were measured with a comb electrode. Almost all the GO on the electrode existed in the form of single nanosheets, which is consistent with previous results[12]. Products, such as CO_2 and H_2, were analyzed using online gas chromatography (Shimadzu, GC-8A) during the irradiation[4].

4.3. Results and Discussion

GO consists of π-conjugated sp^2 and oxygenated sp^3 carbon bonding domains[30], and oxygenated sp^3 carbon domains were selectively oxidized by UV irradiation in O_2 as described in the later section. Figure 4-2 shows the AFM images and height profiles of the GO nanosheets before irradiation (O / (C+O) = 40 at%, C=O = 10 at%; Figure 4-3a and Figure 4-4c) and after irradiation in O_2. Nanopores were produced and porous rGO was formed after 1 h of irradiation. The total area of the nanopores increased as the irradiation time increased and the thickness decreased. When the atomic percent of oxygen in the starting GO sample was small (26 at%), especially for C=O groups (5 at%), the production rate for the nanopores was slow (Figure 4-5). The amount of O and the number of C=O groups can be controlled by the GO preparation conditions. During the oxidation, CO_2 was produced at the C=O groups, which were present at defects in the GO basal plane[31].

Pores were scarcely produced in O_2 in the dark or in N_2 under the same irradiation conditions; therefore the production of the nanopores requires O_2 and UV irradiation. The evolution of CO_2 was also observed during UV irradiation. XPS analysis showed that rGO was produced during irradiation in O_2 and N_2 for 3 h (Figure 4-3b, c). No pores was produced in graphene nanosheets by UV irradiation in O_2, which indicates that O_2 selectively oxidizes the sp^3 oxygenated groups in the basal plane to produce CO_2 and nanopores. Consequently the nanopores roughly correspond to the positions of the sp^3 oxygenated groups and the sp^2 π-conjugated domains on the basal plane of the initial GO sheets. Thus, relatively large sp^2 π-conjugated domains exist in GO with a low degree of oxidation (Figure 4-5, irradiation time of 6 h).

Figure 4-4a,b shows that time dependence of XPS spectra of rGO by UV irradiation in N_2 and O_2, respectively. The XPS spectra were used to perform quantitative analysis of the GO samples. The C1s deconvolution analysis of 5 peaks for C=C, C-C, CH, epoxide (COC), hydroxide (COH), carbonyl (C=O), and carboxide (COOH) as shown in Figure 4-3, was the clearest[23, 32, 33]. This is because the COH group, which was produced by the photoreaction in water and various alcohols, could only be analyzed using this deconvolution method (Figure 4-6 and Table 4-1). The content of

each oxygenated group and the oxygen atomic percent can be calculated for the GO samples, even on oxide substrates such as glass and mica, (Figure. 4-4c) using the calibration curve (Figure. 4-7). The oxygen content decreased from 34 at% to 24 at% and 19 at% after the photoreaction in O_2 and N_2 for 72 h. While the content decreased from immediately after photoreaction in N_2, it hardly changed in O_2 until 30 min of UV irradiation. This result suggests that a different mechanism in O_2 and N_2 has occurred in the early stage of the photoreaction. The content of COC and C=O groups decreased whereas that of the COH group increased until 1h for photoreaction (Figure 4-4c). The COOH content increased only during the O_2 photoreaction and is thus likely to be related to the production of nanopores.

The following photoreactions for the oxygenated groups will occur in O_2 and N_2. They are based on holes and electrons photo-produced in the π valence and π^* conduction bands of the sp^2 π-conjugated domains, as previously reported[4].

$$2C{=}O + H2O\ (ad) \rightarrow COH + COOH\ (\text{in } O_2 \text{ and } N_2) \quad (4\text{-}1)$$

$$C{=}O + COOH \rightarrow CO_2 + COH\ (\text{in } O_2 \text{ and } N_2) \quad (4\text{-}2)$$

$$COC + H_2O\ (ad) \rightarrow 2COH\ (\text{in } O_2 \text{ and } N_2) \quad (4\text{-}3)$$

$$2COC \rightarrow 2C{=}O + C{=}C\ (\text{mainly in } N_2) \quad (4\text{-}4)$$

$$4COH + O_2 \rightarrow 4C{=}O + 2H_2O\ (\text{in } O_2) \quad (4\text{-}5)$$

Reaction 4-1 is the trigger reaction for the production of nanopores. Some of the COOH groups could react with C=O to evolve CO_2 (reaction 4-2), which may produce very small size nanopores. In O_2, many C=O will be produced by the reaction 4-5, leading to promote the reaction 4-2 increasing the sizes and/or number of the nanopores. The increase of COH and decrease of COC will occur mainly by the reaction 4-3 (Figure 4-4c). The water generated by the reaction 4-5 will promote the production of COOH (reaction 4-1) and COH (reactions 4-1 and 4-3) in O_2. Thus, the water which produced at photoreaction only in O_2 could play an important role for the formation of the nanopores. It is also supported that the nanopores are produced under N_2 atmosphere containing H_2O. On the other hand, some of COC groups could also form C=C bonds (sp^2 π-conjugated domain) in N_2 (reaction 4-4), which would increase the electron conductivity.

Photoreduction of GO was also conducted in an aqueous solution of hydrazine (0.01%). Reduction occurred, although no pores were produced and there was no CO_2 evolution (Figure 4-8). Hydrazine directly reacts with the oxygen in the oxygenated groups in GO to reduce them under UV irradiation. UV irradiation promoted the hydrazine reduction (Figure 4-6 and Table 4-1); the reduction was very slow at low concentrations (0.01%) in the dark.

Electron conduction at the basal plane (DC current at 1.0 V) increased with the irradiation time for the reaction in N_2, although the material behaved as an insulator in O_2 under DC bias (Figure 4-9a). When the total oxygen content was below 25~26 at% in N_2, the electron conduction increased because of the increase in the number of sp^2 carbon domains (Eq. 4-4). The rGO electron

conductivity scarcely increased even when the oxygen content was below 25~26 at% for the photoreduction in O_2. This is because of the production of nanopores in the sp^3 areas, where the total oxygen content apparently decreased, while number of sp^2 carbon domains did not increase in the rGO basal plane (Figure 4-10a).

Proton conduction at the basal plane was observed in the samples before the photoreaction and after the photoreaction in O_2. The relative AC resistance (impedance) was measured as a function of the relative humidity (RH; Figure 4-9b). The relative AC resistance was measured at 100 Hz under a 50 mV AC bias using an impedance meter (Hokuto Denko, IVIUM TECHNOLOGIES) at 13 °C. The proton conduction at the basal plane increased from <5% RH and was saturated ~40% RH for the virgin GO, whereas it increased from about 60% RH for the sample irradiated in O_2 for 3 h. This indicates that the proton conduction at the basal plane occurs even at very low humidity for the GO with a large number of epoxide groups. The epoxide groups attached to H_2O molecules act as proton hopping sites, even at low humidity (Figure 4-10b). Buchsteiner *et al.* have reported that water molecules in the interlayer space of the graphite oxide were bound via hydrogen bonds to oxygen atoms of epoxide and OH groups and moved locally through those oxygenated groups in the low humidity[34]. In contrast, the OH and COOH groups, particularly the COOH groups in rGO prepared in O_2, act as the proton conducting sites at high humidity. The H_3O^+ ion probably acts as a proton carrier, because there are a large number of OH and COOH groups. The rGO sample irradiated for 3 h in N_2 had the highest electron conductivity in all the samples, and its DC resistance was about 10^7 Ω (Figure 4-9a) higher than that of AC resistance (10^5 Ω, Figure 4-9b). This difference will be based on the contact resistance between Au electrode and rGO nanosheets, although some proton conduction independent of RH may somewhat affect the AC resistance. H_2O and/or some oxygenated groups will exist between Au and the rGO nanosheets, and will act as an electrochemical resistance. The contact resistance largely affects the DC resistance when the rGO resistivity decreases, but little for the AC resistance. Therefore, the AC resistance will be near the electron resistivity of the rGO nanosheet itself. As a result, the AC resistance of the rGO did not depend on RH, as shown in Figure 4-9b. The electron conductivity of the present rGO single nanosheet was roughly estimated from the AC resistance using the comb electrode dimensions; it was about ~10^{-2} Scm^{-1} and near the reported values[35]. On the other hand, the proton conductivity at the basal plane (in plane) of the GO nanosheet before photoreduction is a little lower (10^{-2}–10^{-3} Scm^{-1}) than the electron conductivity of the present rGO, according to the same calculation using the result in Figure 4-9b. It should be noted that this value is very high compared with the through-plane resistivity of GO paper (10^{-4} Scm^{-1})[23]. However, the accurate values of the electron and proton conductivities of rGO and GO nanosheets must be measured using four probe methods.

4.4. Conclusions

In conclusion, porous GO nanosheets can be easily produced by photoreaction under UV light irradiation in O_2 for several hours. The nanopores were produced in the oxygenated group domains, where CO_2 evolved through photooxidation and the GO was photoreduced. Quantitative XPS analysis showed that the number of epoxide and carbonyl groups decreased during the photoreaction, whereas the number of hydroxide and carboxyl groups increased. The increase in the number of carboxyl groups was significant for the photoreaction in O_2. A pronounced increase in electron conductivity was observed for rGO produced in N_2 below an oxygen content of about 25 at%, but not in the case of O_2 photoreaction. In virgin GO, the proton conduction at the basal plane occurred at the epoxide groups, even at low humidity, and at the carboxyl groups in the porous rGO at high humidity. This is the first demonstration of proton conduction through epoxide groups at the basal plane. Thus, GO and rGO samples with various morphologies, oxygenated functional groups, and conduction types can be easily fabricated by controlling the photoreaction conditions.

References

1. Pan, D.; Zhang, J.; Li, Z.; Wu, M., Hydrothermal Route for Cutting Graphene Sheets into Blue-Luminescent Graphene Quantum Dots. *Adv. Mater.*, **22**, 734-738 (2010).
2. Loh, K. P.; Bao, Q.; Eda, G.; Chhowalla, M., Graphene Oxide as a Chemically Tunable Platform for Optical Applications. *Nature Chem.*, **2**, 1015-1024 (2010).
3. Matte, H.; Subrahmanyam, K. S.; Rao, C. N. R., Novel Magnetic Properties of Graphene: Presence of Both Ferromagnetic and Antiferromagnetic Features and Other Aspects. *J. Phys. Chem. C*, **113**, 9982-9985 (2009).
4. Matsumoto, Y.; Koinuma, M.; Ida, S.; Hayami, S.; Taniguchi, T.; Hatakeyama, K.; Tateishi, H.; Watanabe, Y.; Amano, S., Photoreaction of Graphene Oxide Nanosheets in Water. *J. Phys. Chem. C*, **115**, 19280-19286 (2011).
5. Wang, Y.; Huang, Y.; Song, Y.; Zhang, X.; Ma, Y.; Liang, J.; Chen, Y., Room-Temperature Ferromagnetism of Graphene. *Nano Lett.*, **9**, 220-224 (2009).
6. Miller, J. R.; Outlaw, R. A.; Holloway, B. C., Graphene Double-Layer Capacitor with ac Line-Filtering Performance. *Science*, **329**, 1637-1639 (2010).
7. Zhu, Y. W.; Murali, S.; Stoller, M. D.; Ganesh, K. J.; Cai, W. W.; Ferreira, P. J.; Pirkle, A.; Wallace, R. M.; Cychosz, K. A.; Thommes, M.; Su, D.; Stach, E. A.; Ruoff, R. S., Carbon-Based Supercapacitors Produced by Activation of Graphene. *Science*, **332**, 1537-1541 (2011).
8. Liang, Y. Y.; Li, Y. G.; Wang, H. L.; Zhou, J. G.; Wang, J.; Regier, T.; Dai, H. J., Co_3O_4 Nanocrystals on Graphene as a Synergistic Catalyst for Oxygen Reduction Reaction. *Nature Mater.*, **10**, 780-786 (2011).
9. Nair, R. R.; Wu, H. A.; Jayaram, P. N.; Grigorieva, I. V.; Geim, A. K., Unimpeded Permeation of Water Through Helium-Leak-Tight Graphene-Based Membranes. *Science*, **335**, 442-444 (2012).
10. Stankovich, S.; Dikin, D. A.; Piner, R. D.; Kohlhaas, K. A.; Kleinhammes, A.; Jia, Y.; Wu, Y.; Nguyen, S. T.; Ruoff, R. S., Synthesis of Graphene-Based Nanosheets via Chemical Reduction of Exfoliated Graphite Oxide. *Carbon*, **45**, 1558-1565 (2007).
11. Becerril, H. A.; Mao, J.; Liu, Z.; Stoltenberg, R. M.; Bao, Z.; Chen, Y., Evaluation of Solution-Processed Reduced Graphene Oxide Films as Transparent Conductors. *ACS Nano*, **2**, 463-470 (2008).
12. Yang, D.; Velamakanni, A.; Bozoklu, G.; Park, S.; Stoller, M.; Piner, R. D.; Stankovich, S.; Jung, I.; Field, D. A.; Ventrice, C. A.; Ruoff, R. S., Chemical Analysis of Graphene Oxide Films after Heat and Chemical Treatments by X-ray Photoelectron and Micro-Raman Spectroscopy. *Carbon*, **47**, 145-152 (2009).
13. Matsumoto, Y.; Koinuma, M.; Kim, S. Y.; Watanabe, Y.; Taniguchi, T.; Hatakeyama, K.; Tateishi, H.; Ida, S., Simple Photoreduction of Graphene Oxide Nanosheet under Mild Conditions. *ACS Appl. Mater. Interfaces*, **2**, 3461-3466 (2010).

14. Matsumoto, Y.; Morita, M.; Kim, S. Y.; Watanabe, Y.; Koinuma, M.; Ida, S., Photoreduction of Graphene Oxide Nanosheet by UV-light Illumination under H_2. *Chem. Lett.*, **39**, 750-752 (2010).
15. Garaj, S.; Hubbard, W.; Reina, A.; Kong, J.; Branton, D.; Golovchenko, J. A., Graphene as a Subnanometre Trans-Electrode Membrane. *Nature*, **467**, 190-193 (2010).
16. Bayley, H., Nanotechnology: Holes with an Edge. *Nature*, **467**, 164-165 (2010).
17. Du, H.; Li, J.; Zhang, J.; Su, G.; Li, X.; Zhao, Y., Separation of Hydrogen and Nitrogen Gases with Porous Graphene Membrane. *J. Phys. Chem. C*, **115**, 23261-23266 (2011).
18. Schrier, J., Fluorinated and Nanoporous Graphene Materials as Sorbents for Gas Separations. *ACS Appl. Mater. Interfaces*, **3**, 4451-4458 (2011).
19. Dreyer, D. R.; Park, S.; Bielawski, C. W.; Ruoff, R. S., The Chemistry of Graphene Oxide. *Chem. Soc. Rev.*, **39**, 228-240 (2010).
20. Cote, L. J.; Cruz-Silva, R.; Huang, J. X., Flash Reduction and Patterning of Graphite Oxide and Its Polymer Composite. *J. Am. Chem. Soc.*, **131**, 11027-11032 (2009).
21. Ansari, S.; Kelarakis, A.; Estevez, L.; Giannelis, E. P., Oriented Arrays of Graphene in a Polymer Matrix by in situ Reduction of Graphite Oxide Nanosheets. *Small*, **6**, 205-209 (2010).
22. Choi, B. G.; Hong, J.; Park, Y. C.; Jung, D. H.; Hong, W. H.; Hammond, P. T.; Park, H., Innovative Polymer Nanocomposite Electrolytes: Nanoscale Manipulation of Ion Channels by Functionalized Graphenes. *ACS Nano*, **5**, 5167-5174 (2011).
23. Zarrin, H.; Higgins, D.; Jun, Y.; Chen, Z. W.; Fowler, M., Functionalized Graphene Oxide Nanocomposite Membrane for Low Humidity and High Temperature Proton Exchange Membrane Fuel Cells. *J. Phys. Chem. C*, **115**, 20774-20781 (2011).
24. Karim, M. R.; Hatakeyama, K.; Matsui, T.; Takehira, H.; Taniguchi, T.; Koinuma, M.; Matsumoto, Y.; Akutagawa, T.; Nakamura, T.; Noro, S.; Yamada, T.; Kitagawa, H.; Hayami, S., Graphene Oxide Nanosheet with High Proton Conductivity. *J. Am. Chem. Soc.*, **135**, 8097-8100 (2013).
25. Wang, Y.; Shi, Z. Q.; Huang, Y.; Ma, Y. F.; Wang, C. Y.; Chen, M. M.; Chen, Y. S., Supercapacitor Devices Based on Graphene Materials. *J. Phys. Chem. C*, **113**, 13103-13107 (2009).
26. Chen, S.; Zhu, J.; Wu, X.; Han, Q.; Wang, X., Graphene Oxide-MnO_2 Nanocomposites for Supercapacitors. *ACS Nano*, **4**, 2822-2830 (2010).
27. Liu, C.; Yu, Z.; Neff, D.; Zhamu, A.; Jang, B. Z., Graphene-Based Supercapacitor with an Ultrahigh Energy Density. *Nano Lett.*, **10**, 4863-4868 (2010).
28. Gao, W.; Singh, N.; Song, L.; Liu, Z.; Reddy, A. L. M.; Ci, L. J.; Vajtai, R.; Zhang, Q.; Wei, B. Q.; Ajayan, P. M., Direct Laser Writing of Micro-Supercapacitors on Hydrated Graphite Oxide Films. *Nature Nanotechnol.*, **6**, 496-500 (2011).
29. Hummers, W. S.; Offemen, R. E., Preparation of Graphitic Oxide. *J. Am. Chem. Soc.*, **80**, 1339

(1958).

30. Eda, G.; Lin, Y. Y.; Mattevi, C.; Yamaguchi, H.; Chen, H. A.; Chen, I. S.; Chen, C. W.; Chhowalla, M., Blue Photoluminescence from Chemically Derived Graphene Oxide. *Adv. Mater.*, **22**, 505-509 (2010).
31. Dimiev, A.; Kosynkin, D. V.; Alemany, L. B.; Chaguine, P.; Tour, J. M., Pristine Graphite Oxide. *J. Am. Chem. Soc.*, **134**, 2815-2822 (2012).
32. Ganguly, A.; Sharma, S.; Papakonstantinou, P.; Hamilton, J., Probing the Thermal Deoxygenation of Graphene Oxide Using High-Resolution In Situ X-ray-Based Spectroscopies. *J. Phys. Chem. C*, **115**, 17009-17019 (2011).
33. Compton, O. C.; Jain, B.; Dikin, D. A.; Abouimrane, A.; Amine, K.; Nguyen, S. T., Chemically Active Reduced Graphene Oxide with Tunable C / O Ratios. *ACS Nano*, **5**, 4380-4391 (2011).
34. Buchsteiner, A.; Lerf, A.; Pieper, J., Water Dynamics in Graphite Oxide Investigated with Neutron Scattering. *J. Phys. Chem. B*, **110**, 22328-22338 (2006).
35. Park, S.; Ruoff, R. S., Chemical Methods for the Production of Graphenes. *Nature Nanotechnol.*, **4**, 217-224 (2009).

Table 4-1. Oxygen atm% and content of each oxygenated functions of GO treated by photoreduction

	C-C,C=C, C-H (%)	C-OH (%)	C-O-C (%)	C=O (%)	COOH (%)	O/(C+O) (atm%)
GO (0 h)	49.5	6.0	28.3	8.4	7.9	33.9
GO in water with ethanol (48 h)	73.1	15.9	3.9	0	7.1	18.0
GO in water with propanol (48 h)	72.7	16.4	2.7	0.8	7.3	20.7
GO in water with phenol (48 h)	74.9	18.4	2.9	2.8	0.9	16.8
GO in water with hydrazine(48 h)	75.2	9.6	5.2	1.3	6.1	16.6

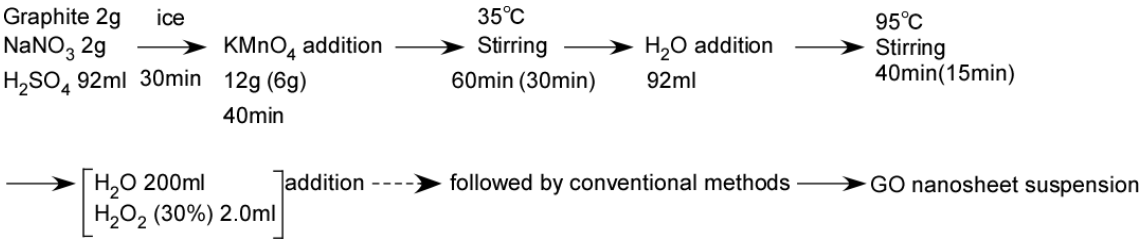

Figure 4-1. Conventional Hammers' method to prepare graphene oxide. Conditions in the parenthesis are for the preparation case of GO nanosheets with low oxidation degree. This GO is used as the starting sample for the photoreaction tests shown in Figure 4-5.

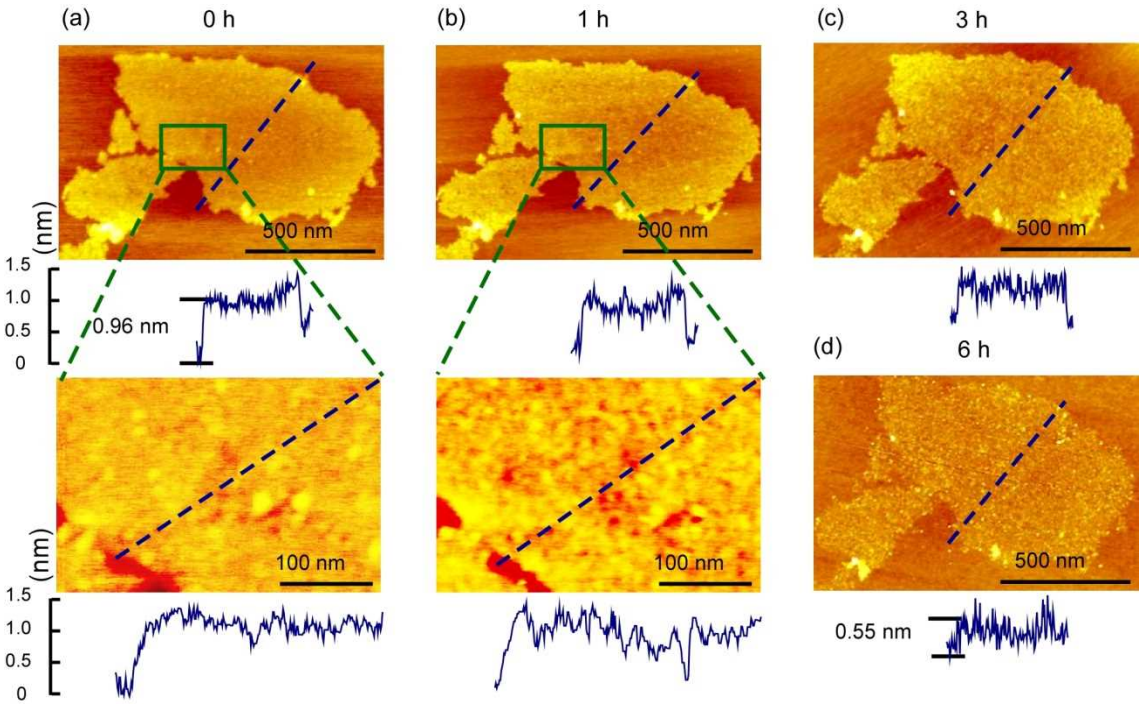

Figure 4-2. AFM images of the GO nanosheet after the photoreaction in O_2. The images are for the same sheet after irradiation for (a) 0 h, (b) 1 h, (c) 3 h, and (d) 6 h. The pores were produced after about 1 h. Height profiles are also shown for each image.

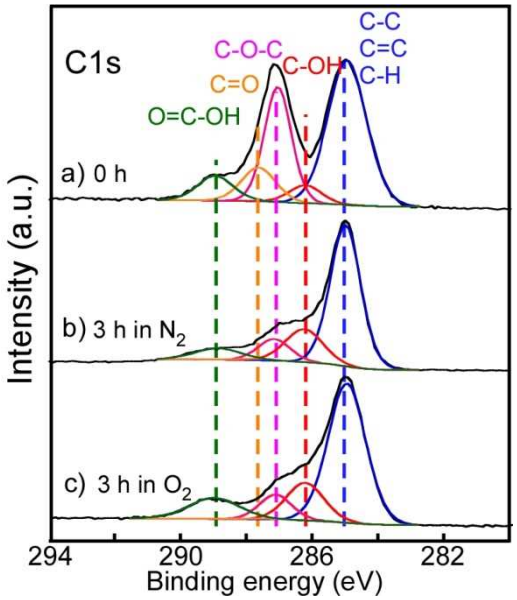

Figure 4-3. XPS spectra of C1s for GO before (a) and after the photoreaction in N_2 (b) and O_2 (c) for 3 h.

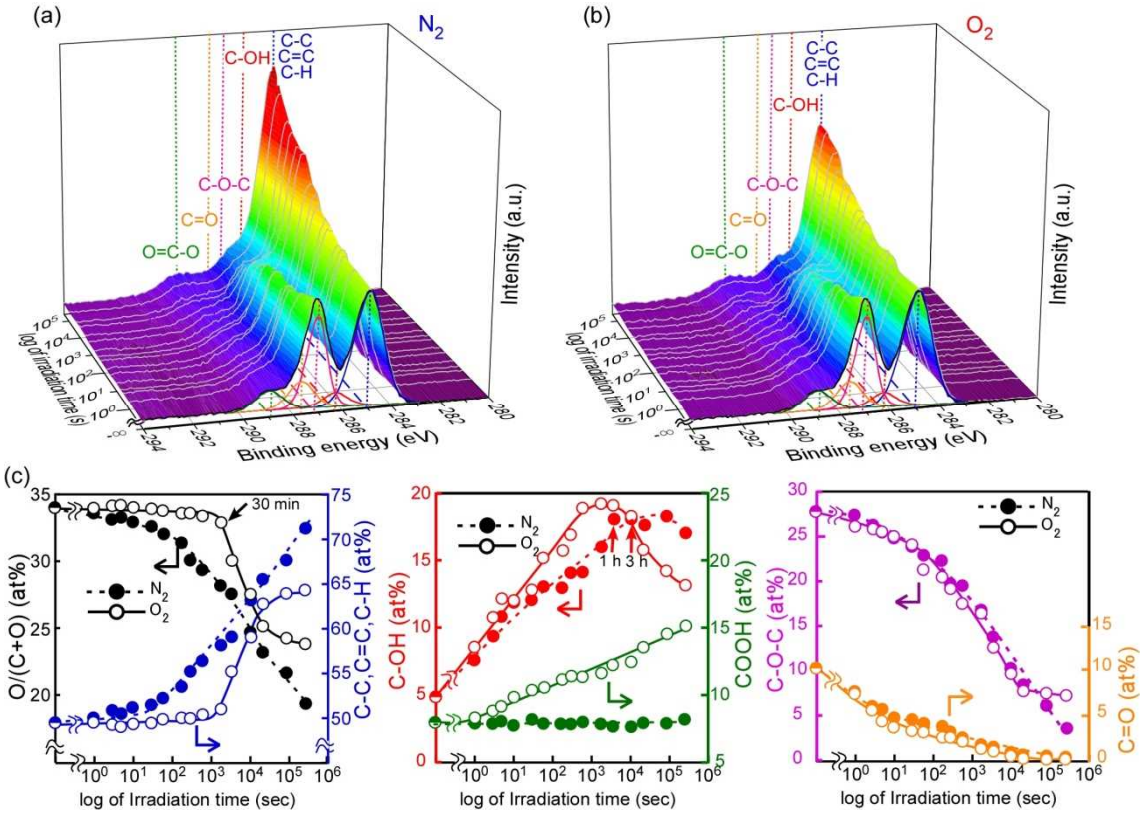

Figure 4-4. Time dependence of XPS spectra of rGO by UV irradiation in (a) N_2 and O_2. (c) Oxygenated group content for the GO as a function of irradiation time in N_2 and O_2.

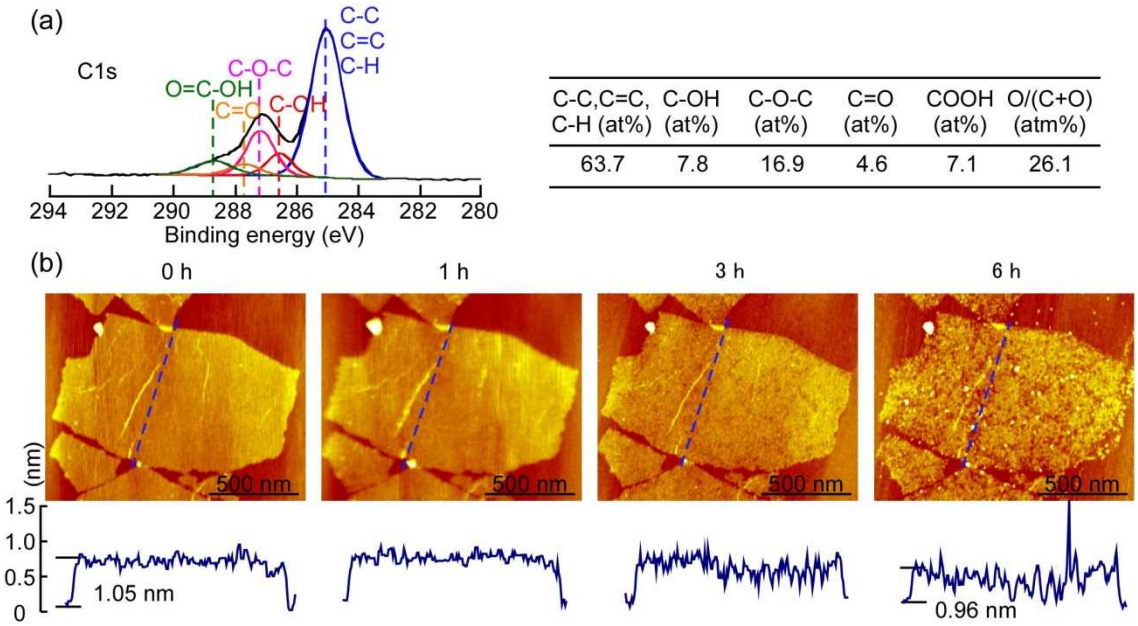

C-C,C=C, C-H (at%)	C-OH (at%)	C-O-C (at%)	C=O (at%)	COOH (at%)	O/(C+O) (atm%)
63.7	7.8	16.9	4.6	7.1	26.1

Figure 4-5. (a) XPS spectrum of C1s of starting GO with low degree oxidation and its compositions, and (b) AFM images after photoreaction in O_2. The pores were produced at irradiation time over about 3 h.

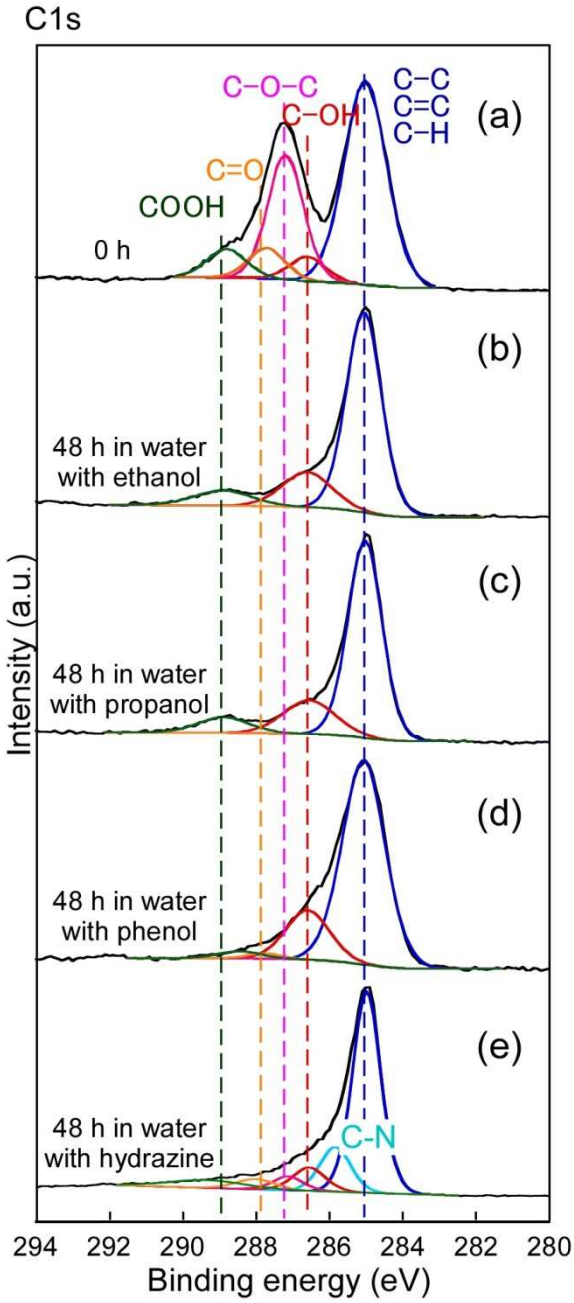

Figure 4-6. XPS spectra of C1s of GO prepared by photoreaction in various aqueous solutions. (a) starting GO, (b) in water with ethanol (0.5%), (c) propanol (0.5%), (d) phenol (0.5%), and (e) hydrazine (0.01%).

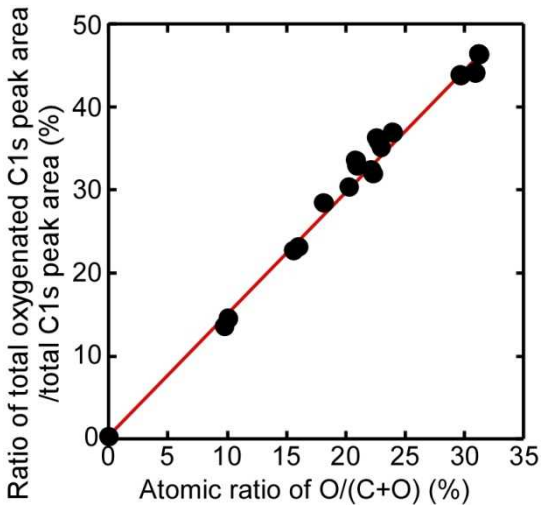

Figure 4-7. The calibration curve which denotes the relationship between the C1s peak area (%) of all the oxygenated groups and oxygen atomic percent (O / (O + C)), based on the XPS elemental analysis (all the GO samples on Pt substrates were photoreduced for a controlled irradiation time).

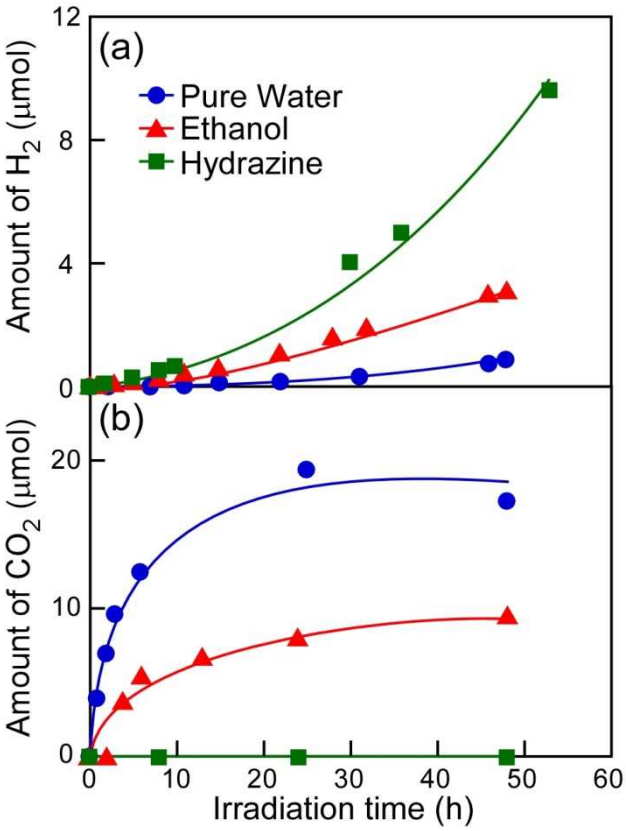

Figure 4-8. Amounts of H_2 and CO_2 evolved from water suspension of GO as a function of irradiation time. The GO suspension was 35 mL pure water containing 1.5 mg GO. The light source is 500 W xenon lamp. The experimental method and conditions are the same as chapter 3. Additions of ethanol and hydrazine were 0.5 and 0.01% in amount, respectively.

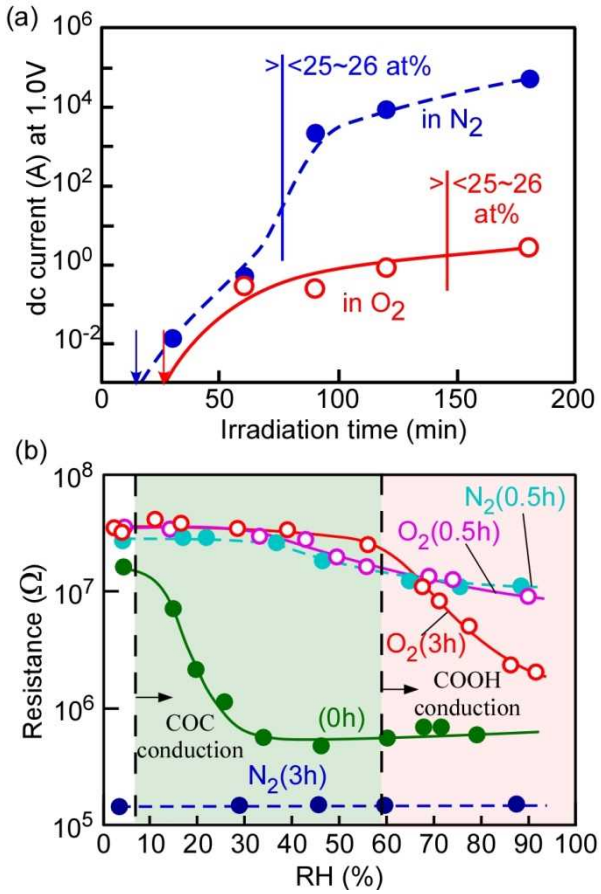

Figure 4-9. Electron and proton conductivities of the GO samples before and after the photoreaction in N_2 and O_2. (a) Currents at 1.0 V (electron conductivities) of the samples as a function of irradiation time. (b) Resistance as a function of relative humidity (RH), where the samples were irradiated in N_2 and O_2.

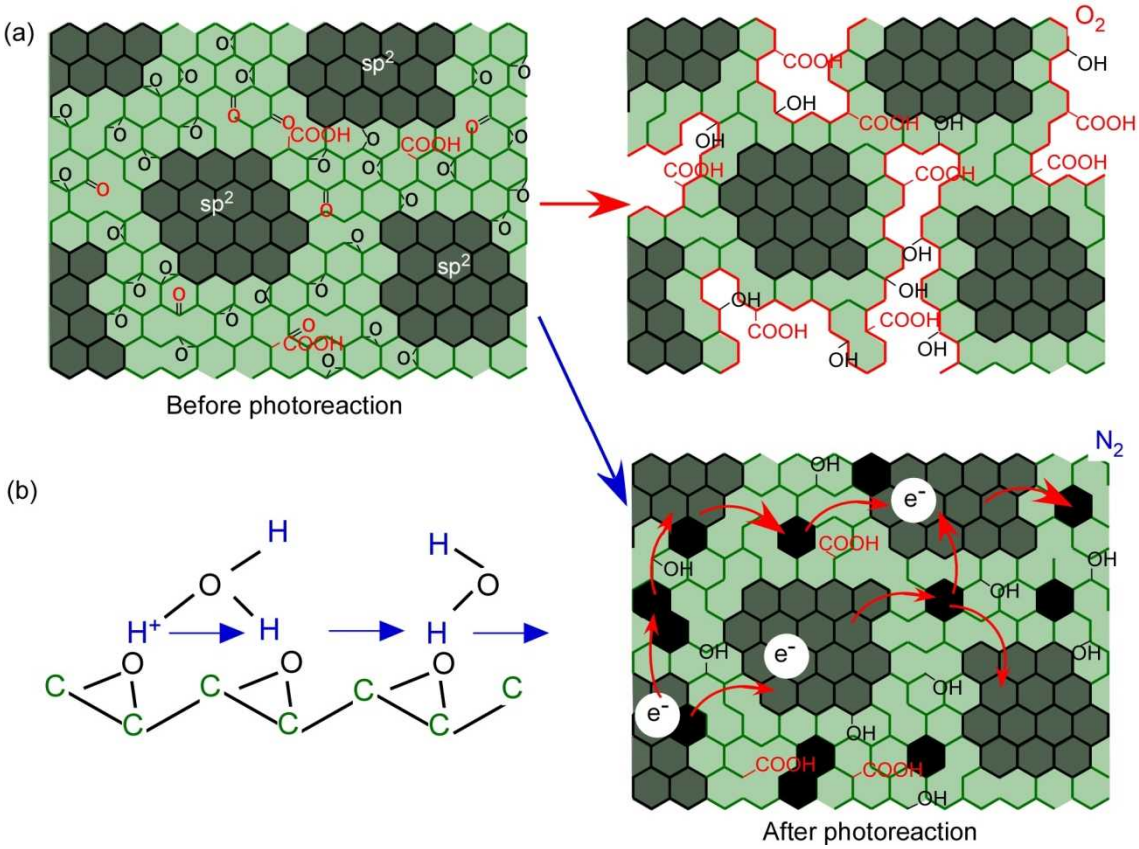

Figure 4-10. (a) Models of the pore production by the photoreaction of GO in N_2 and O_2. (b) Model of proton conduction at epoxide groups.

Chapter 5

Proton Conduction of Graphene Oxide

5.1. Introduction

Chemical networks for rapid propagation of protons are constantly being researched worldwide since Rogers and Ubbelohde reported the phenomenon in 1950[1]. A wide range of applications in biological systems, fuel cells, sensors, and chemical filters are the pertinent reason behind the worldwide research on designing inert and faster proton conductors[2-4]. As a result, proton conductors based on organic and coordination polymers, such as hydrocarbon ionomers, acid-doped polymers, inorganic/organic nanohybrids, superprotonic solid acids, and acid/base ionic liquids, have been developed to date, and the typical conductivity ranges reported for Nafion, phosphates, carboxylic acids, and imidazoles are 10^{-1}–10^{-5}, 10^{-1}–10^{-4}, 10^{-5}–10^{-6} and 10^{-6}–10^{-8} Scm^{-1}, respectively[5-10]. Some ceramic materials with outstandingly high conductivities have been reported as well[11]. However, for fuel cell applications, besides high conductivity, it is vital that the material possesses constant activity under humid, hot, and acidic conditions[12]. Thus, an inert polymeric matrix is usually preferred as the foundation for designing an ionic conductor. In this chapter, we consider the possibility of graphene oxide (GO) as a potential vehicle to transport protons, as its stability is very high and it contains closely located oxygenated functional groups (COC, COH, C=O and COOH) that extend outward from the flat two-dimensional carbon network and seem to assemble into one-dimensional hydrogen-bonded channels for proton transport[13-15]. Previously, Jung *et al.*[16] used bulk graphite oxide (GO') as a filler for different polymer electrolytes, while Zarrin *et al.*[17] observed higher conductivity in a sulfonic acid-functionalized GO' / Nafion composite than in powdered GO'. Later, Ravikumar and Scott developed sulfonated GO' paper with appreciable conductivity[18]. However, all of these studies involved bulk samples, and the in-plane ionic conductivity of pure GO nanosheets is still unknown. In this chapter, we for the first time successfully measured the in-plane ionic conductivity of single and multilayer GO. Moreover, the dependence of conductivities on the film thickness and modification (ethylenediamine (enGO) and H_2SO_4 (sGO)) is demonstrated.

Only a few number of layered materials has been found to function as solid electrolyte. The conventional sampling limits the conductivity, as the rigidity of the particles, inter-particle distances, and orientation of tiny particles in pellet is difficult to control. In this respect, this study demonstrates not only the super-ionic conductivity of GO, and sGO, but also a novel multilayer fabrication technique, which we believe is affordable to improve the conductivities of other solid electrolytes.

4.2. Experiment

Graphite oxide (GO') was prepared through modified Hummers' method[19] using graphite powder, $NaNO_3$, H_2SO_4, $KMnO_4$, and H_2O_2 solutions (Wako Pure Chemical Industries Ltd). The graphite oxide was suspended in distilled water by ultrasonication for 2 h, and the suspension was centrifuged to remove heavier particles. The enGO was prepared by stirring GO solution (10 mL, 0.6 g / L), and ethylenediamine (20 mL) for 34 h at room temperature. The mixture was washed three times with distilled water by centrifugation (50000 rpm, 10 min.). Two different samples of single-layer GO were fabricated on comb electrode (width 2 μm, interval 2 μm, and 65 pairs; BAS Ltd.; Figure 5-1a) surfaces, using the Langmuir Blodgett (LB) assembly, and drop-cast method (Figure 5-2a and b). In drop-cast method, single-layer GO was prepared by dropping, and quickly swabbing of dilute GO dispersion on the electrodes followed by 2 h drying under vacuum. Single-layer LB film was synthesized by reported procedure[20]. In short, the water trough for LB film forming equipment (USI, USI-3-22) was cleaned with acetone, and distilled water. It was then filled by deionized water. A mixture of 1.8 mL GO solution (1 g / L) and 9 mL methanol was then added dropwise on the water surface from the minimum distance in a very slow rate (40 minutes duration). Then the floated GO fragments were gathered with a barrier speed of 0.17 mm / sec. The pressure increased gradually, and at 23 mN / m, the comb electrode was pulled into the trough with a speed of 0.017 mm / sec (Figure 5-3).

Multilayer GO films, enGO, and GO walled tubes loaded by electrolytes (H_2SO_4, Na_2SO_4, and HCl) were fabricated by drop-cast method only (Figure 5-2c). Thicknesses of the GO films were regulated by controlling the concentration of GO solution. The multilayer GO films with variable thickness (60, 200, and 1000 nm), and enGO film (160 nm) were prepared from 0.15 μL GO (0.3, 0.6, and 6 g / L), and enGO (0.5 g / L) solutions respectively. The sGO films were prepared by mixing GO (10 mL, 0.6 g / L), and H_2SO_4 solutions (0.12, 0.24, and 0.60 mL; 0.19 mol / L), and were dropped on comb electrodes. Other electrolytes were also loaded by similar method. To obtain GO, and sGO paper (thickness about 18 μm), 20 mL of the GO solution (4 g / L), and sGO solution (10 mL, S / C = 0.08) respectively was filtrated using a membrane filter (0.4 μm pore size, Merck Millipore) under reduced pressure for overnight followed by vacuum drying. The morphology, and thickness of the samples on the comb electrodes were evaluated by AFM (Atomic force microscope, Bruker, Digital Instruments Nanoscope V). Interlayer distances within the films were measured by PXRD (powder X ray diffractometer, Rigaku, RINT2500) using Cu Kα (λ = 0.154 nm) radiation. SEM (scanning electron microscope) measurements were performed using a field-emission SEM (Hitachi High-Tech, SU-8000). EDS (elemental dispersive spectra) were obtained using an attached EDAX (coupled with Hitachi High-Tech SU-8000) spectrometer. The elemental compositions, and assignments of the carbon peaks of the samples were analyzed by XPS (X ray photoelectron spectrometer, Thermo Scientific, Sigma Probe). TGA (Thermo gravimetric analysis) curves were

generated in a thermal analyzer (Seiko Instruments, EXSTAR 6000) at scan rate 10 °C / min. The FT-IR (Fourier transform infrared) spectra were recorded using a FT-IR spectrometer (Perkin-Elmer, Frontier IR / FIR) with KBr pellets. The proton conductivities of the films were measured by an impedance/gain phase analyzer (Solartron 1260) in the frequency range from 1 MHz to 1 Hz with a perturbation voltage amplitude of 50 mV. The measured resistance of bare comb electrode was very high, (> 10^8 Ω) which confirmed the absence of any parasitic impedance contribution. The dominance of ionic conductivity was confirmed from isotope effect using D_2O humid condition. To calculate the conductivities, we used the formula $\sigma = L / (R \times T \times D)$. R is a variable quantity, which varied with respect to % RH and was calculated from the diameter of corresponding cole-cole plot (Figure 5-4). L is the film width, which was fixed for all the samples as 2×10^{-4} cm (the distance between two electrodes). T is the thickness of nanosheet and was measured from AFM height profile. D is the length of nanosheets connecting the two electrodes and was measured by observing the geometric shape of nanosheet by microscope. D and T are fixed quantity for a sample during a series of measurement at various % RH. However, the complexity and difficulties was associated with the measurement of the D values. The techniques for measurement of D values were different for single layer GO and multilayer GO films. In all cases the geometric shape of the film or nanosheet assembly using charge-coupled device (CCD) (multilayer GO film) or SEM (single-layer GO film) images were taken under consideration. The methods for calculation of D and area for are described below:

Measurement of areas for multilayer samples

For multilayer assembly, we would like to explain the measurement of D value for 60 nm GO film as an example. The location of a typical GO film on comb electrode is presented by Figure 5-1a. At first, from CCD image (Figure 5-1c and f), the area occupied by GO film on comb electrodes was calculated to be 3.24×10^{-3} cm^{-2}. This value is the sum of areas of GO film on the comb electrode teeth and the areas of GO film connecting pairs of opposite electrode's teeth. However, the fraction of area on the comb electrode teeth is insignificant for proton conductivity measurement, as it doesn't signify proton transportation within two opposite electrode. Therefore, to calculate the σ value, we only considered the part of GO film connecting two neighboring teeth. As both the teeth width and distance between two opposite electrodes are the same (2 μm), the area of GO film locating between two electrodes is 1.6×10^{-3} cm^{-2}, which is half of the total area of the GO film (Figure 5-1d and g). Dividing this value by 2×10^{-4} cm (the value of L) we have found the value of D as 8.1 cm. Finally the quantity, T × D was calculated as:

$$60 \text{ nm} \times 8.1 \text{ cm} = (6.0 \times 10^{-6} \times 8.1) \text{ cm}^2 = 4.8\times10^{-5} \text{ cm}^2.$$

Measurement of areas for single-layer samples.

In case of single layer GO, there exists two types of nanosheet: (1) interior nanoseets, which are located on a single electrode and (2) bridging nanosheets, which connect two neighboring

electrodes (Figure 5-1h and i). As the interior nanoseets have no contribution to the displayed conductivity, we excluded this type from our calculation. For bridging nanosheets, the overall D value was calculated from the summation of lengths of all the small GO nanosheet observed by SEM. We observed 50 random spots, throughout the whole assembly. Corresponding to every spot D_{xT} was calculated as.

$$D_{xT} = (D_1 + D_2 + D_3 + D_4 + D_5 + \ldots + D_y) \times S_{total} / S_{xT}.$$

Here, y is the total number of bridging nanosheets at a spot, S_{total} is the area of comb electrodes (1.04×10^{-2} cm^{-2}) and S_{xT} is the projected area of that spot. D_{xT} is the estimated D value based on the projected spot. Finally, statistically the most accurate D value was calculated from the average as, $D = (D_{1T} + D_{2T} + D_{3T} + D_{4T} + D_{5T} + \ldots + D_{50T}) / 50$. In this way, D was calculated to be 9.3 and 7.8 cm for the drop cast and LB assembly, respectively.

The proton conductivity of GO paper was measured by a four-probe DC method using a potentiostat with a function generator (IVIUM TECHNOLOGIES, Compact Stat)[21].

5.3. Results and Discussion

Assembly, and proton conductivities of single-layer GO, multilayer GO, and enGO.

The single and multilayer nature of the films were confirmed from AFM, and SEM images (Figure 5-5). The relative humidity (RH) dependent in-plane proton conductivities of single-layer GO, multilayer GO films, and enGO at 25 °C temperature are represented in Figure 5-6a. The conductivities were calculated by measuring resistances from the diameter of semicircles in corresponding Cole–Cole plots (Figure 5-4). For all samples the σ values increase almost linearly with RH. The conductivity of single-layer GO increased from 6×10^{-7} Scm^{-1} at 55% RH to 2×10^{-4} Scm^{-1} at 90% RH. Other samples behaved almost similarly. The dominance of the conductivity was confirmed by the isotope effect at low temperature (<300 °C). The conductivity of H_2O-humidified GO was ~1.25 times higher than that of D_2O-humidified GO (Figure 5-7a). Though this value is low, it agrees with the results of some previous works, where this ratio was reported to be 1.1−1.4 and 2−3.5 as evidence for proton-oriented conduction at low (<300 °C) and high temperature (>300 °C), respectively[22-26]. The conductivities increase with respect to membrane thickness. At 60% RH, the σ value for single-layer GO is 1×10^{-6} Scm^{-1}, which increases to 1×10^{-4}, and 4×10^{-4} Scm^{-1} for 60, and 200 nm thick films respectively. Following this trend a thicker GO membrane should display a higher conductivity. Therefore, the σ value (2×10^{-3} Scm^{-1}) that we reported for a 18 μm thick GO paper (Figure 5-6a), complies with present observation[21]. In contrast, the 160 nm thick enGO film exhibits a sudden fall in conductivity. Though the thickness of enGO film is much higher, its typical conductivity values as, 1×10^{-8}, 7×10^{-6}, and 6×10^{-4} Scm^{-1} at 30, 60, and 90% RH are lower than the 60 nm GO film at least by single order. The increment rates for RH dependent conductivities of different GO films are not the same. The related divergence of the lines in Figure 5-6a at low RH (<

40%) indicates that the thickness dependency of σ values is more prominent when the water content in the film is low. Figure 5-6b represents that σ has the lowest value for single-layer GO which increases gradually with a very sharp steep upto 200 nm thickness, beyond which a saturated state with σ value around 4×10^{-4} Scm^{-1} is attained. The variation in conductivities with temperature (10–40 °C), and related Arrhenius plots with activation energy (E_a) are presented in Figures 5-8 and 5-9. Figure 5-6c represents the thickness dependent E_a values at 60% RH. The E_a value is the maximum (0.28 eV) for single-layer GO, and decreases sharply with film thickness upto 200 nm, beyond which a stable value around 0.08 eV is existed. The E_a value for proton conduction on enGO film is 0.26 eV, which is almost double than that for GO film with similar thickness. The E_a value also increases with RH (inset of Figure 5-6c). The E_a value for the 150 nm thick GO film increases from 0.08 eV at 30% RH to 0.2 eV at 90% RH. Figure 5-6d represents that the σ value for LB single-layer is ≈ 5 times higher than that for the single-layer assembled by drop-cast method.

The in-plane, and through-plane conductivity of a proton conducting membrane are not necessarily the same, the in-plane conductivity of GO is higher than the through-plane conductivity[21, 27]. According to Meyer's hypothesis, a very thin film (less than 4 times the Debye length) should exhibit very high ionic conductance[28, 29]. Therefore, the increase in σ value for nanometer ranged GO nanosheet is as per the expectation. Bur, as for both the single, and multilayer assembly, the displayed conductivities are in-plane, the variation in σ values with respect to number of overlapped layer is supposed to be governed by water content and hydration behavior. The related hydration phenomenon, and water dynamics for oxidized graphitic materials were reported previously by several groups[30-32]. GO contains both the hydrophobic, and hydrophilic domains. The hydrophobic part is the graphene basement whereas, the hydrophilic part includes OH, and COOH groups (located at the edges), and COC groups extends from some interior sp^3 hybridized carbon atoms[33, 34]. The thin GO nanosheets support both the upstream, and downstream fluxes of protons along the adsorbed water film which also results higher conductivity. In case of multilayer assembly, the film takes the shape of a compact bundle of numerous two dimensional conductive channels. In comparison with single-layer GO, both the water adsorbing capacity, and hydration dynamics in such bundle are improved by several ways. First of all, the space between two layers contains increased amount of hydrophilic groups extended from both the GO walls, and supports higher water content which results increased conductivity. Besides, the higher amount of adsorbed water within interlayer of GO was reported to generate a larger, and flexible interlayer distances[35]. We suggest that these modifications promote proton propagation, as the larger size, and flexibility of the cavity support the translational movement, and hydrogen bond reformation in a faster way. From the viewpoint of hydration dynamics, the rate of hydrogen bond reformation is also higher, as it is accelerated by two opposite GO walls. Also, we suggest that in multilayer channels the propagating protons have the option to change the conduction track (Figure 5-10a). The GO walls have numerous

nanopores, using which the mobilized protons can change the track from one layer to the surrounding layers. These wide, and alternative conduction pathways accelerate the ionic movement. The divergence of lines at low RH in Figure 5-6a is significant. From thermo gravimetric analysis (TGA) we found that the water content in the 18 μm thick GO paper at 30, and 90% RH is about 21, and 31 wt% respectively (Figure 5-11d). The variation of water content with respect to film thickness is higher at low RH, which results increased variation in σ values, and related divergence at low RH. Besides, excessive population of water molecule at the interlayer might be a fact behind the convergence effect at higher RH. Although, the increased amount of water provides a faster track for proton propagation, excessive water results higher intermolecular interaction, and some suppression, which is negligible at low RH. This fact is also supported by the increase in E_a values with respect to RH (inset of Figure 5-6c). The decrease in E_a value with respect to film thickness (Figure 5-6c) complies with the increased σ value for thicker film.

The lower conductivity of enGO (Figure 5-6a) due to the distraction of some epoxy groups during chemical bond formation with ethylenediamine confirms the epoxide groups as the major contributor for proton transportation. The XPS spectra (Figure 5-12) revel that during chemical transformation significant amount of COC groups of GO has been converted to OH group in enGO, but the decrease in σ value confirms that OH groups are insignificant for proton transportation. The high E_a value (Figure 5-6c) also confirms the difficulties for proton transportation through enGO. The higher conductivity in LB single-layer (Figure 5-6d) is resulted from a continuous, and wider pathway assembled from edge to edge joining of small GO fragments in LB film. The low E_a values for all the samples (< 0.3 eV) suggest that proton is transported by Grotthuss mechanism[36], which is the usual phenomenon for proton conduction through H_2SO_4 solution[37], and Nafion[38, 39].

Optimization of proton conductivity in graphene oxide by filling sulfate ions.

The AFM, and SEM images, EDS analysis, and PXRD patterns in Figure 5-11 confirm the presence of sulfate ions (H_2SO_4, SO_4^{2-}, and HSO_4^-) in sGO. AFM images (Figure 5-11a) indicate the presence of some veins (3–100 nm), and hills (400–800 nm, not wrinkles) in the sGO samples. These swelled spots seem to be occupied by H_2SO_4 or related dissociated ions. However, the EDS mapping with SEM images (Figure 5-11b) for GO, and sGO sample confirm the presence of excess sulfur in these veins, and hills. In addition, XPS spectra shows that the average ratio of SO_4^{2-} ion to H_2O in the sGO samples is within the range of 0.08–0.3 (Figure 5-12). Figure 5-11c represents the XRD patterns of GO, and sGO. For GO the layer distance is 0.85 nm whereas, those for sGO are 1.7, and 1.2 nm with S / C (sulfur to carbon) atomic ratio as 0.41, and 0.08 respectively. The random distribution of sulfate ions is also confirmed from the non-uniform interlayer separation indicated from the broad diffraction peaks for sGO. Figure 5-11d represents the TGA data for sGO, and GO (18 μm paper for both) at high, and low RH. For sGO (with S / C ratio as 0.08) the water content is about 18, and 46 wt% at 30, and 90% RH respectively, whereas for GO at similar RH conditions, the

respective values are 21, and 31 wt%.

Figure 5-14a represents the conductivities of Nafion[40, 41] multilayer GO films loaded by H_2SO_4, Na_2SO_4, and HCl. At high RH (> 40%), the conductivities of sGO films increase significantly. HCl incorporation results a lower conductivity, while the Na_2SO_4 loaded sample displays σ values almost equal to sGO samples at comparatively higher RH condition. Though some sGO films (120, and 170 nm) are thinner than a multilayer GO film (200 nm), the conductivities (≈ 10^{-1} Scm^{-1}) are significantly higher. The conductivity for sGO films at high RH are almost equal to that for Nafion at 30 °C[27]. Even the conductivity can be considered to be higher than Nafion at high RH considering the difference in experimental temperature (25 °C for sGO films, and 30 °C for Nafion). At low RH the conductivities of sGO films are lower than those for GO films. Figure 5-14b shows that E_a values decrease for proton conduction through Nafion, and sGO films, whereas a reverse trend is followed by multilayer GO film. These results clearly indicate the maximization of conductivities by loading sulfate ion into the GO walled cavities in multilayer assembly. We suggest several reasons behind this observation. Firstly in sGO films, at high RH both the GO nanosheet, and sulfate ion function as water adsorbing material. As a result, the overall water content is increased, which is supported by the TGA data as well (Figure 5-11d). In reverse, at low RH the amount of water in sGO samples is small, and sufficient enough to be adsorbed on the functional sites of GO only. Hence, instead of participating in proton transportation, the sulfate ions attribute some barrier within the conduction pathway which results the lower conductivities[35]. Secondly, at low water content, the intercalated acid molecules dissociate, and the H^+ ion blocks the fraction of some epoxy functional sites of GO, which ultimately damages the continuity of the conduction channels. However, at high RH this phenomenon becomes insignificant as the H^+ ions find available water molecules to form H_3O^+ ions, and release the GO functional sites. The low conductivity of HCl loaded sample also complies with this issue. The Na_2SO_4 loaded sample also exhibits higher conductivity due to the presence of sulfate ions. These sulfate ions behave as dilute sulfuring acid solution after reacting with adsorbed water. As the Na^+ ion blocks some of the epoxy sites of GO, a higher RH (ca 60%) is needed to solvolyse Na^+ ion for freeing the epoxy sites. Almost a similar σ values for Na_2SO_4, and H_2SO_4 loaded GO while a lower conductivity for HCl loaded sample confirms that in sGO films the sulfate ions plays the major role to increase the conductivity. Sulfuric acid is a well-known proton conductor which transfers protons through hydrogen-bonded network of water at low concentrations[35]. The structure of sGO film is comparable with Nafion. In Nafion some hydrophilic $–SO_3^-$ functional groups are present[36], whereas in sGO, there exist some oxygenated functional sites, and intercalated sulfate ion. Therefore, the sGO films can be considered as the parallel assembly of some dilute sulfuric acid filled GO walled cavities. The protons run with the fastest way through these cavities with the support of both the sulfuric acid solution, and the fundamental advantages provided by multilayer GO.

Figure 5-10 represents a perspective proton conduction mechanism through single and multilayer GO and sGO. In multilayer GO films there exist numerous nanopores in the GO walls (Figure 5-10a), through which the mobilized proton can change track from one layer to the surrounding layers, and the conductivity increases significantly. In case of single-layer GO and multilayer GO films, proton mobility and hydrogen bond reformation is supported by single, and double GO walls respectively (Figure 5-10b and c). Figure 5-10d shows the presence of sulfate ion, at the interlayer in sGO. Conductivity here is influenced by hydronium ions. In sGO, protons mainly move through the veins, and hills. The maximum conductivity is resulted from both the support of dilute sulfuric acid solution within the GO walled cavities, and the fundamental advantages provided by multilayer GO films. We also studied the effect of H_2SO_4 concentration on the conductivities of sGO films. With relatively large amounts of H_2SO_4, the proton conductivities remarkably increased beyond 40% RH (Figure 5-14a). For GO, the increment in E_a value with RH is consistent with the proton conduction behavior of graphite oxide reported previously[31]. But for sGO films, the E_a value decreases with RH, and matches with that for Nafion[40, 42].

5.4. Conclusions

In conclusion, we fabricated multilayer GO films, which resemble with bundles of GO walled cavities. The proton conductivities were measured for single-layer GO, multilayer GO films, enGO, and GO films loaded by various electrolytes. A gradual trend in conductivity is observed due to the improvement of conduction pathway, and stepwise increment in water content. The conductivities follow the trend as: GO' < single-layer GO nanosheet (drop-cast film < LB film) < multilayer GO (thin film < thick film < GO paper[21]) < sGO. The proton conductivities of multilayer GO films are higher than that for single-layer GO by two to three orders. The proton conductivities of sGO films at high RH increased significantly, and at 25 °C, the σ value exceeded that of Nafion (10^{-2} to 10^{-1} Scm^{-1}). Proton conductivity increased with the thickness of multilayer GO film, probably because of the increment in water adsorbing capacity, improvement of hydration dynamics, and the option of ion propagation from layer to layer through the nanopores. In enGO, the proton conductivity drastically decreased due to the formation of chemical bond between the epoxy groups of GO, and ethylenediamine. This observation indicates that the epoxy groups are the major contributor for proton transportation. The highest proton conductivity was achieved by incorporating sulfuric acid molecules within the GO walled cavities. The protons run in the fastest way through these cavities with the support of both the dilute sulfuric acid solution, and the fundamental advantages provided by multilayer GO. For all the samples, the displayed σ values represent the in-plane conductivity. The law E_a values indicate the possibility of the materials for practical application. The multilayer fabrication process, and acid loading technique that we employed here are facile, quick, and reproducible. We propose that these methods can be utilized to maximize the

proton conductivity in other layered materials.

References

1. Rogers, S. E.; Ubbelohde, A. R., Melting and Crystal Structure. III.—Low-melting Acid Sulphates. *Trans. Faraday Soc.*, **46**, 1051-1061 (1950).
2. Voth, G. A., Computer Simulation of Proton Solvation and Transport in Aqueous and Biomolecular Systems. *Acc. Chem. Res.*, *39*, 143-150 (2006).
3. Royant, A.; Edman, K.; Ursby, T.; Pebay-Peyroula, E.; Landau, E. M.; Neutze, R., Helix Deformation is Coupled to Vectorial Proton Transport in the Photocycle of Bacteriorhodopsin. *Nature*, **406**, 645-648 (2000).
4. Kreuer, K. D., Proton Conductivity: Materials and Applications. *Chem. Mater.*, **8**, 610-641 (1996).
5. Bose, S.; Kuila, T.; Thi Xuan Lien, N.; Kim, N. H.; Lau, K.-t.; Lee, J. H., Polymer Membranes for High Temperature Proton Exchange Membrane Fuel Cell: Recent Advances and Challenges. *Prog. Polym. Sci.*, **36**, 813-843 (2011).
6. Yang, L.; Tang, J.; Li, L.; Chen, X.; Ai, F.; Yuan, W. Z.; Wang, L.; Zhang, Y., High Quality Pristine Perfluorosulfonated Ionomer Membranes Prepared from Perfluorinated sulfonyl Fluoride Solution. *RSC Adv.*, **2**, 5950-5953 (2012).
7. Vilciauskas, L.; Tuckerman, M. E.; Bester, G.; Paddison, S. J.; Kreuer, K.-D., The Mechanism of Proton Conduction in Phosphoric Acid. *Nature Chem.*, **4**, 461-466 (2012).
8. Woundenberg, R. C.; Yavuzcetin, O.; Tuominen, M. T.; Coughlin, E. B., Intrinsically Proton Conducting Polymers and Copolymers Containing Benzimidazole Moieties: Glass Transition Effects. *Solid State Ionics*, **178**, 1135-1141 (2007).
9. McKeen, J. C.; Yan, Y. S.; Davis, M. E., Proton Conductivity of Acid-Functionalized Zeolite Beta, MCM-41, and MCM-48: Effect of Acid Strength. *Chem. Mater.*, **20**, 5122-5124 (2008).
10. Kreuer, K. D., On the Development of Proton Conducting Polymer Membranes for Hydrogen and Methanol Fuel Cells. *J. Membr. Sci.*, **185**, 29-39 (2011).
11. Pergolesi, D.; Fabbri, E.; D'Epifanio, A.; Di Bartolomeo, E.; Tebano, A.; Sanna, S.; Licoccia, S.; Balestrino, G.; Traversa, E., High Proton Conduction in Grain-Boundary-Free Yttrium-Doped Barium Zirconate Films Grown by Pulsed Laser Deposition. *Nature Mater.*, **9**, 846-852 (2010).
12. Zhang, H.; Shen, P. K., Recent Development of Polymer Electrolyte Membranes for Fuel Cells. *Chem. Rev.*, **112**, 2780-2832 (2012).
13. Mkhoyan, K. A.; Contryman, A. W.; Silcox, J.; Stewart, D. A.; Eda, G.; Mattevi, C.; Miller, S.; Chhowalla, M., Atomic and Electronic Structure of Graphene-Oxide. *Nano Lett.*, **9**, 1058-1063 (2009).
14. Szabo, T.; Berkesi, O.; Forgo, P.; Josepovits, K.; Sanakis, Y.; Petridis, D.; Dekany, I., Evolution of Surface Functional Groups in a Series of Progressively Oxidized Graphite Oxides. *Chem. Mater.*, **18**, 2740-2749 (2006).

15. Dreyer, D. R.; Park, S.; Bielawski, C. W.; Ruoff, R. S., The Chemistry of Graphene Oxide. *Chem. Soc. Rev.*, **39**, 228-240 (2010).
16. Jung, J. H.; Jeon, J. H.; Sridhar, V.; Oh, I. K., Electro-Active Graphene-Nafion Actuators. *Carbon*, **49**, 1279-1289 (2011).
17. Zarrin, H.; Higgins, D.; Jun, Y.; Chen, Z. W.; Fowler, M., Functionalized Graphene Oxide Nanocomposite Membrane for Low Humidity and High Temperature Proton Exchange Membrane Fuel Cells. *J. Phys. Chem. C*, **115**, 20774-20781 (2011).
18. Ravikumar; Scott, K., Freestanding Sulfonated Graphene Oxide Paper: A New Polymer Electrolyte for Polymer Electrolyte Fuel Cells. *Chem. Commun.*, **48**, 5584-5586 (2012).
19. Hummers, W. S.; Offemen, R. E., Preparation of Graphitic Oxide. *J. Am. Chem. Soc.*, **80**, 1339 (1958).
20. Cote, L. J.; Kim, F.; Huang, J., Langmuir-Blodgett Assembly of Graphite Oxide Single Layers. *J. Am. Chem. Soc.*, **131**, 1043-1049 (2009).
21. Tateishi, H.; Hatakeyama, K.; Ogata, C.; Gezuhara, K.; Kuroda, J.; Funatsu, A.; Koinuma, M.; Taniguchi, T.; Hayami, S.; Matsumoto, Y., Graphene Oxide Fuel Cell. *J. Electrochem. Soc.*, **160**, F1175-F1178 (2013).
22. Aoki, Y.; Habazaki, H.; Nagata, S.; Nakao, A.; Kunitake, T.; Yamaguchi, S., Finite Size Effect of Proton-Conductivity of Amorphous Silicate Thin Films Based on Mesoscopic Fluctuation of Glass Network. *J. Am. Chem. Soc.*, **133**, 3471-3479 (2011).
23. Kitamura, N.; Amezawa, K.; Tomii, Y.; Yamamoto, N., Protonic Conduction in Rare Earth Orthophosphates with the Monazite Structure. *Solid State Ionics*, **162**, 161-165 (2003).
24. Nowick, A. S.; Vaysleyb, A. V., Isotope Effect and Proton Hopping in High-Temperature Protonic Conductors. *Solid State Ionics*, **97**, 17-26 (1997).
25. Bonanos, N., Transport Properties and Conduction Mechanism in High-Temperature Protonic Conductors. *Solid State Ionics*, **53**, 967-974 (1992).
26. Shin, S.; Huang, H. H.; Ishigame, M.; Iwahara, H., Protonic Conduction in the Single Crystals of $SrZrO_3$ and $SrCeO_3$ Doped withY_2O_3. *Solid State Ionics*, **40-41**, 910-913 (1990).
27. Soboleva, T. Y.; Xie, Z.; Shi, Z. Q.; Tsang, E.; Navessin, T. C.; Holdcroft, S., Investigation of the Through-Plane Impedance Technique for Evaluation of Anisotropy of Proton Conducting Polymer Membranes. *J. Electroanal. Chem.*, **622**, 145-152 (2008).
28. Maier, J., Defect Chemistry and Ionic Conductivity in Thin Films. *Solid State Ionics*, **23**, 59-67 (1987).
29. Maier, J., Defect Chemistry and Ion Transport in Nanostructured Materials: Part II. Aspects of Nanoionics. *Solid State Ionics*, **157**, 327-334 (2003).
30. Cerveny, S.; Barroso-Bujans, F.; Alegria, A.; Colmenero, J., Dynamics of Water Intercalated in Graphite Oxide. *J. Phys. Chem. C*, **114**, 2604-2612 (2010).

31. Buchsteiner, A.; Lerf, A.; Pieper, J., Water Dynamics in Graphite Oxide Investigated with Neutron Scattering. *J. Phys. Chem. B*, **110**, 22328-22338 (2006).
32. Lerf, A.; Buchsteiner, A.; Pieper, J.; Schottl, S.; Dekany, I.; Szabo, T.; Boehm, H. P., Hydration Behavior and Dynamics of Water Molecules in Graphite Oxide. *J. Phys. Chem. Solids*, **67**, 1106-1110 (2006).
33. Yan, J. A.; Xian, L. D.; Chou, M. Y., Structural and Electronic Properties of Oxidized Graphene. *Phys. Rev. Lett.*, **103**, 086802 (2009).
34. Lerf, A.; He, H. Y.; Forster, M.; Klinowski, J., Structure of Graphite Oxide Revisited. *J. Phys. Chem. B*, **102**, 4477-4482 (1998).
35. Gun'ko, V. M.; Turov, V. V.; Whitby, R. L. D.; Prykhod'ko, G. P.; Turov, A. V.; Mikhalovsky, S. V., Interactions of Single and Multi-Layer Graphene Oxides with Water, Methane, Organic Solvents and HCl Studied by ^{1}H NMR. *Carbon*, **57**, 191-201 (2013).
36. Agmon, N., The Grotthuss Mechanism. *Chem. Phys. Lett.*, **244**, 456-462 (1995).
37. Choe, Y. K.; Tsuchida, E.; Ikeshoji, T., First-Principles Molecular Dynamics Study on Aqueous Sulfuric Acid Solutions. *J. Chem. Phys.*, **126**, 154510 (2007).
38. Mauritz, K. A.; Moore, R. B., State of Understanding of Nafion. *Chem. Rev.*, **104**, 4535-4585 (2004).
39. Choe, Y. K.; Tsuchida, E.; Ikeshoji, T.; Yamakawa, S.; Hyodo, S., Nature of Proton Dynamics in a Polymer Electrolyte Membrane, Nafion: a First-Principles Molecular Dynamics Study. *Phys. Chem. Chem. Phys.*, **11**, 3892-3899 (2009).
40. Dong, B.; Gwee, L.; Salas-de la Cruz, D.; Winey, K. I.; Elabd, Y. A., Super Proton Conductive High-Purity Nafion Nanofibers. *Nano Lett.*, **10**, 3785-3790 (2010).
41. Sone, Y.; Ekdunge, P.; Simonsson, D., Proton Conductivity of Nafion 117 as Measured by a Four-Electrode AC Impedance Method. *J. Electrochem. Soc.*, **143**, 1254-1259 (1996).
42. Chen, L.; Hallinan, D. T.; Elabd, Y. A.; Hillmyer, M. A., Highly Selective Polymer Electrolyte Membranes from Reactive Block Polymers. *Macromolecules*, **42**, 6075-6085 (2009).
43. Smirnov, M. Y.; Kalinkin, A. V.; Pashis, A. V.; Sorokin, A. M.; Noskov, A. S.; Kharas, K. C.; Bukhtiyarov, V. I., Interaction of Al_2O_3 and CeO_2 Surfaces with SO_2 and SO_2 + O_2 Studied by X-ray Photoelectron Spectroscopy. *J. Phys. Chem. B*, **109**, 11712-11719 (2005).

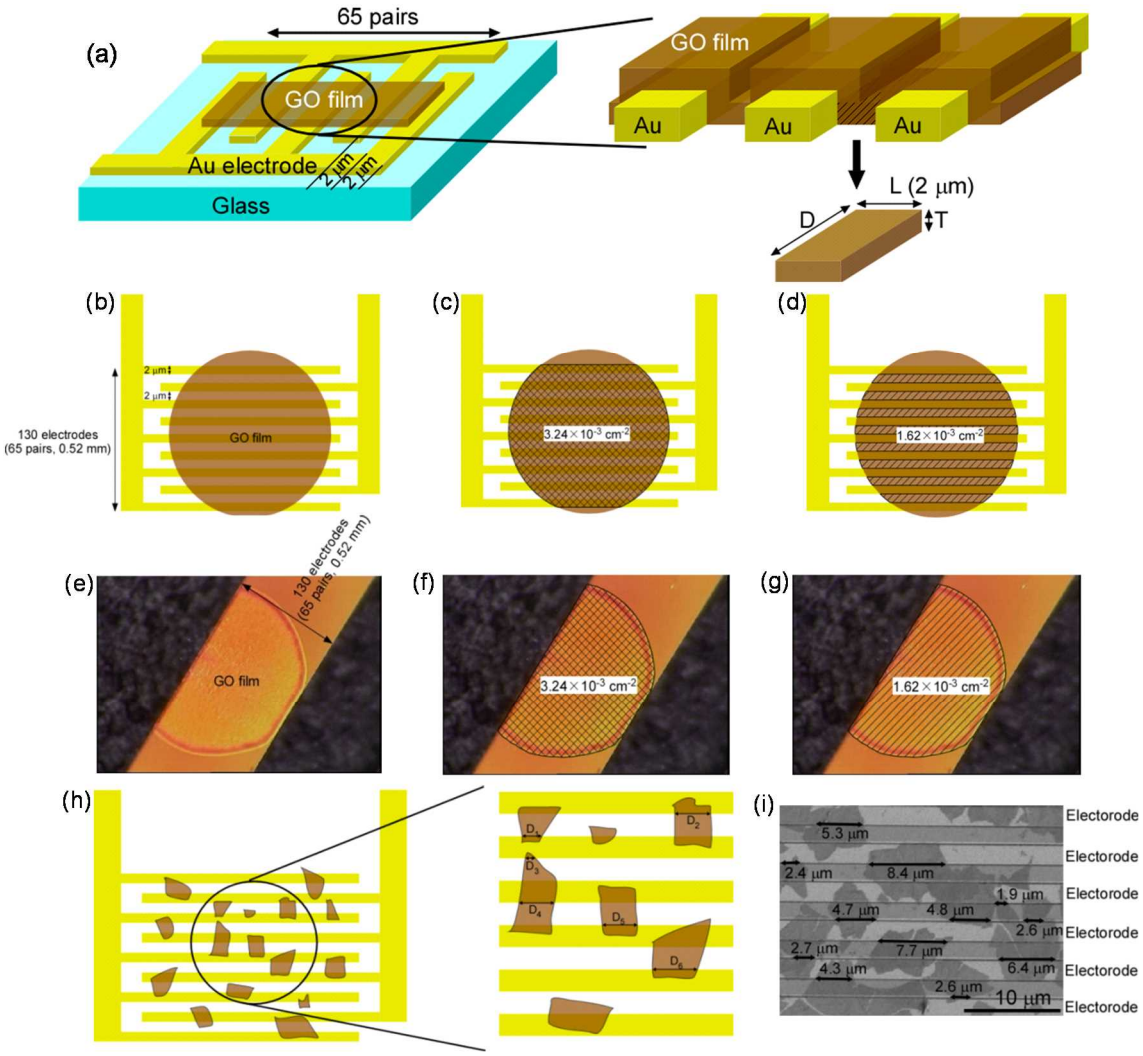

Figure 5-1. (a) Schematic for GO film on face to face assembled comb electrode pair with related parameters (L, D and T). The part of GO film bent toward the gap between two electrodes, which is evidenced from AFM height profile (Figure 5-5). (b) Schematic for 60 nm multilayer GO film on comb electrode. (c) Marked area signifies total area of the film combined from the area on comb teeth and between the teeth. (d) Marked area signifies the area between comb teeth. (e) CCD images of 60 nm multilayer GO film on comb electrodes. (f) Marked area signifies combination of areas on comb teeth and between the teeth. (g) Marked area signifies the area between comb teeth. (h) Schematic of single-layer GO films on comb electrodes and (i) Typical SEM image of single-layer GO films on comb electrodes.

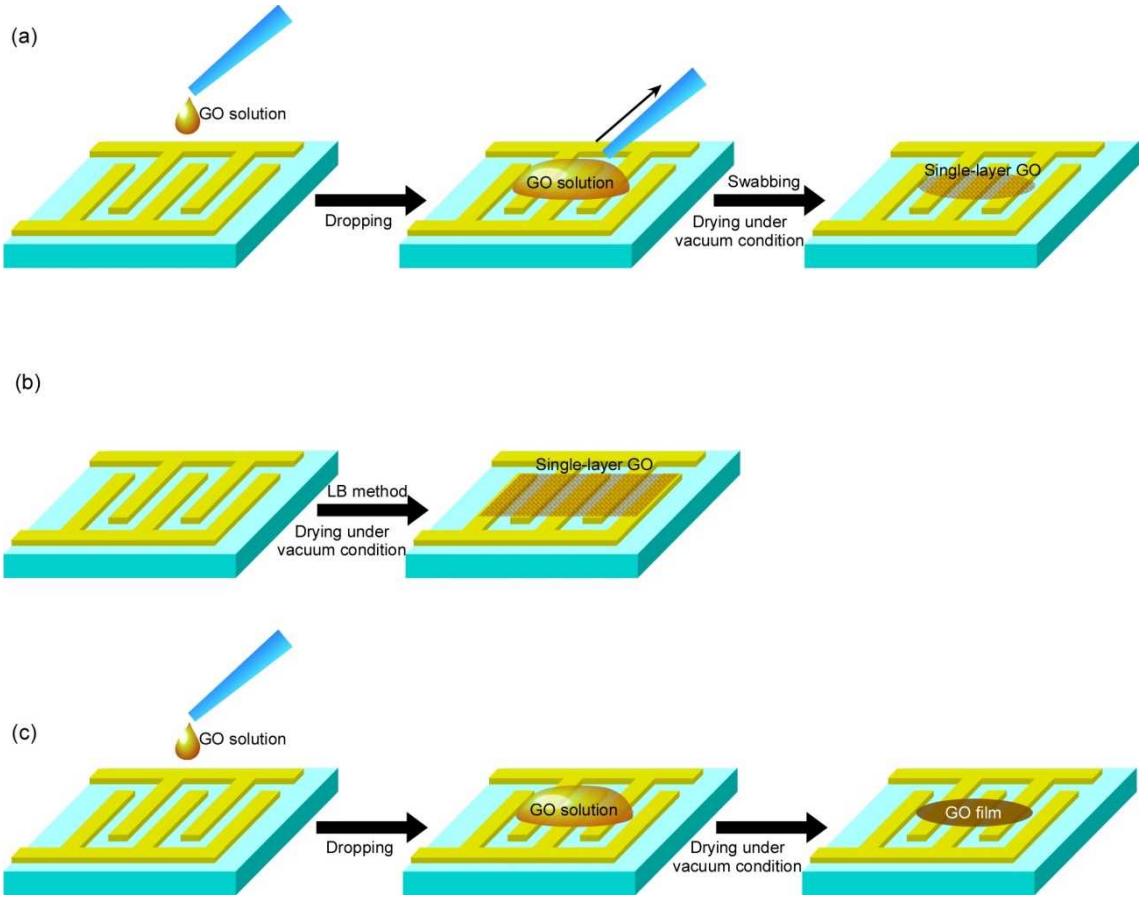

Figure 5-2. Schematic of sample preparation methods. (a), (c) GO single nanosheet samples by drop-cast and LB methods, respectively. (c) Film sample.

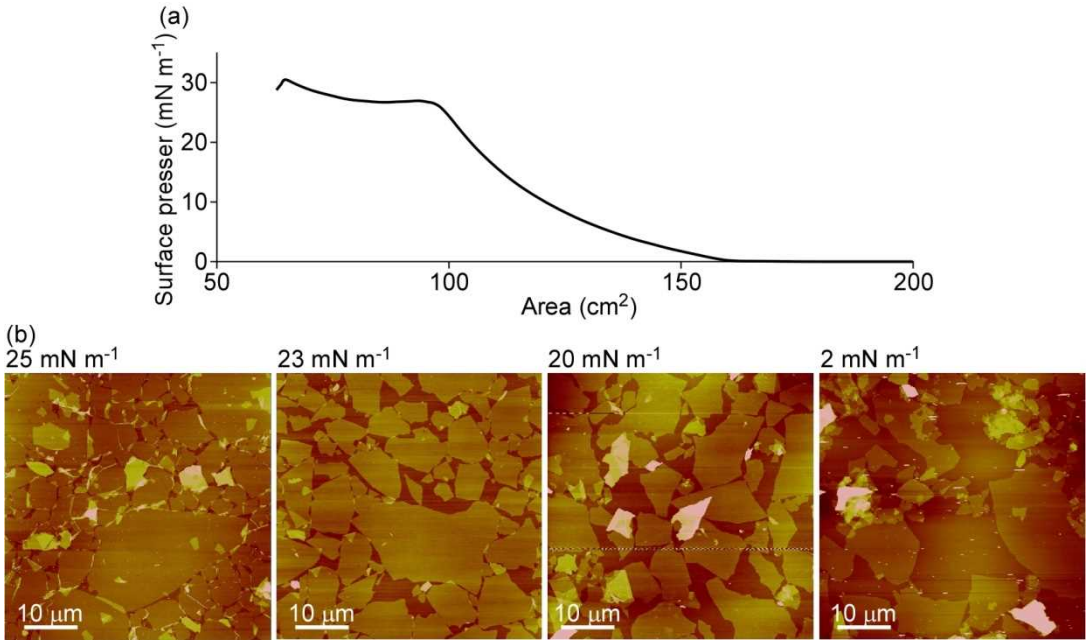

Figure 5-3. LB assembly of GO on silicon substrate. (a) Surface pressure / area plot. (b) AFM images of GO nanosheets under various surface pressers. The density of GO nanosheets increases with surface presser. GO nanosheets overpacked at 25 mN m^{-1} surface presser.

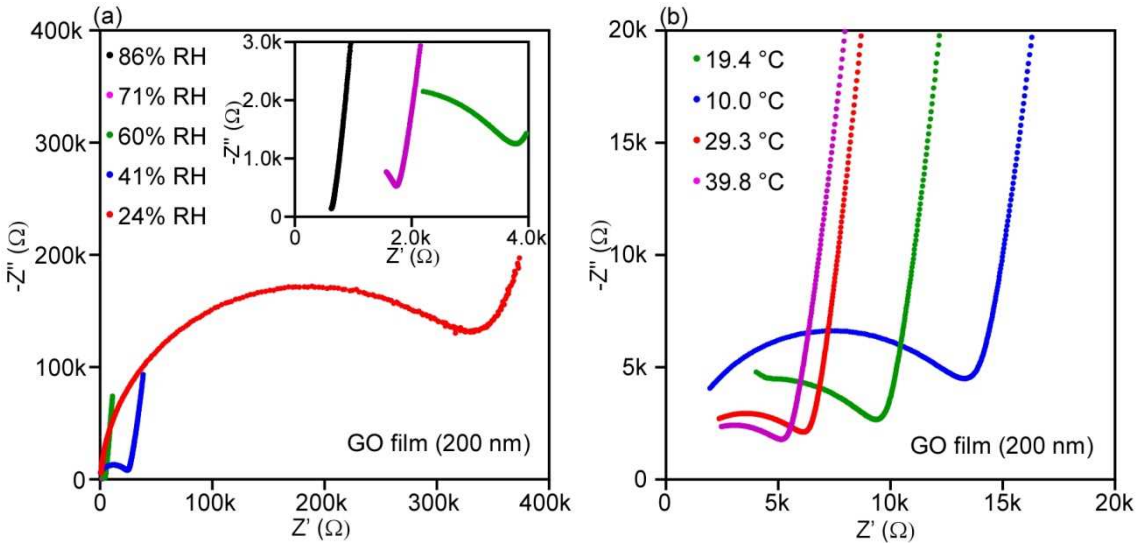

Figure 5-4. Typical impedance spectra (Cole-Cole plots) of the GO film (200 nm). (a) Dependence of RH (values at high frequency region are magnified in the inset). (b) Dependence on temperature. Measurements were carried out in the frequency range from 1 MHz to 1 Hz with a perturbation voltage amplitude of 50 mV.

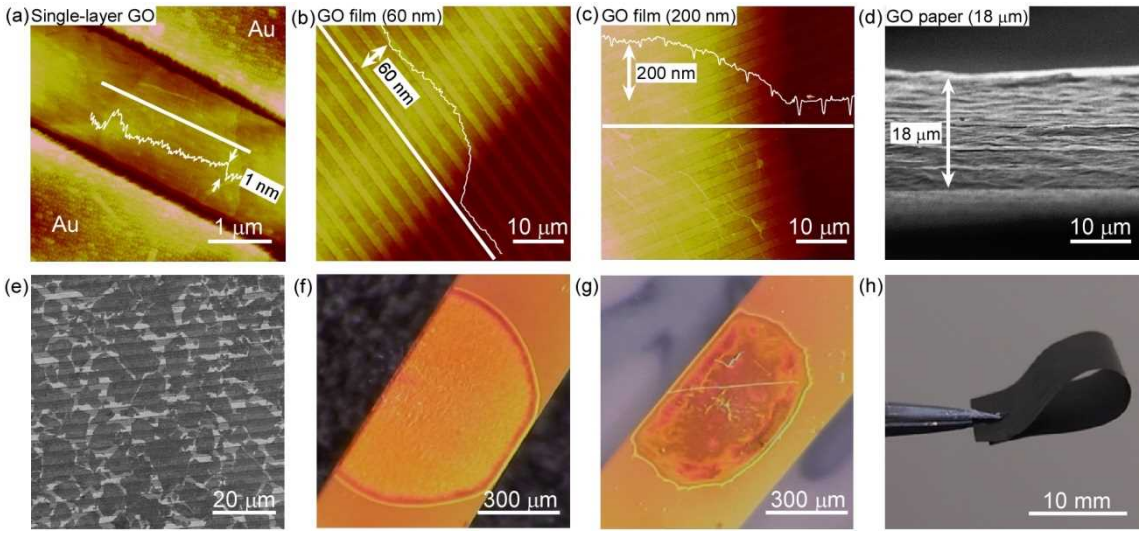

Figure 5-5. (a), (b), and (c) AFM images, and height profiles for single-layer GO (generated by LB film), 60, and 200 nm multilayer GO films (generated by drop-cast method) respectively. (d), and (e) SEM images for 18 μm thick GO paper, and LB assembly of single-layer GO film. (f), and (g) CCD images of 60, and 200 nm thick GO films respectively on comb electrode surface. (h) Photograph of GO paper.

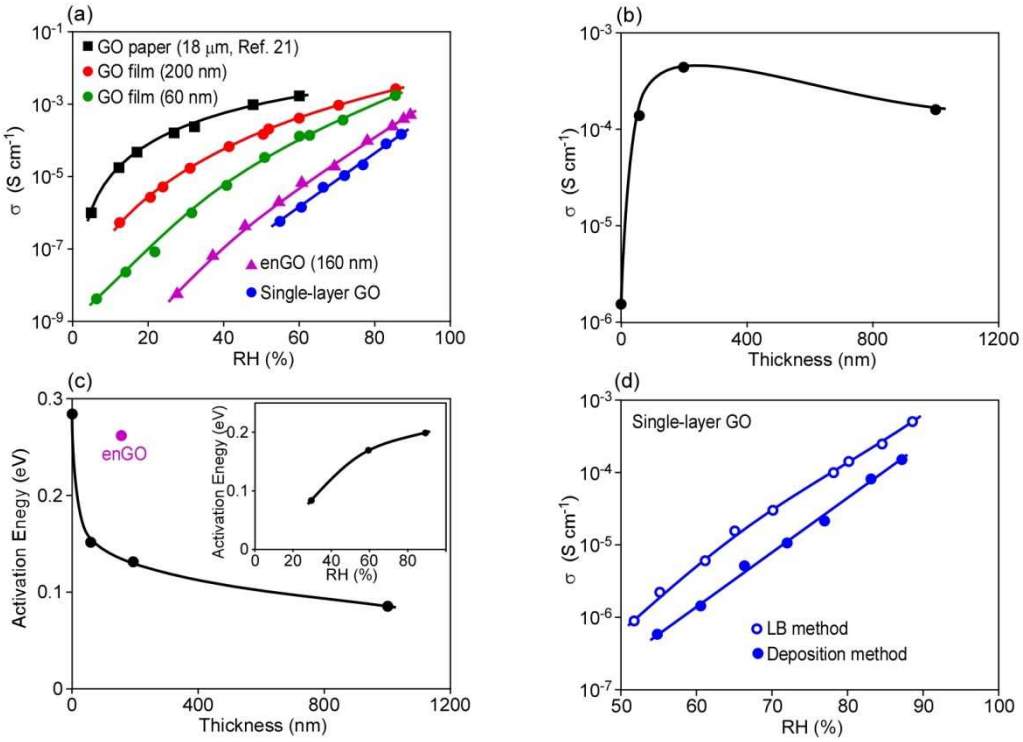

Figure 5-6. (a) Dependence of proton conductivities of various GO films on RH (thicknesses of the GO films are described in parentheses). (b) Dependence of conductivities on film thickness. (c) Dependence of E_a values on the thickness of the GO films at 60% RH. (Inset) Dependence of the E_a values of GO film (thickness is 150 nm) on RH. (d) RH dependent conductivities of single-layer GO produced by LB, and drop-cast method.

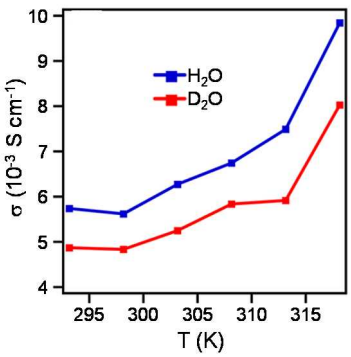

Figure 6-7. Temperature-dependent conductivities of GO humidified by H_2O (blue) and D_2O (red) at 95% RH.

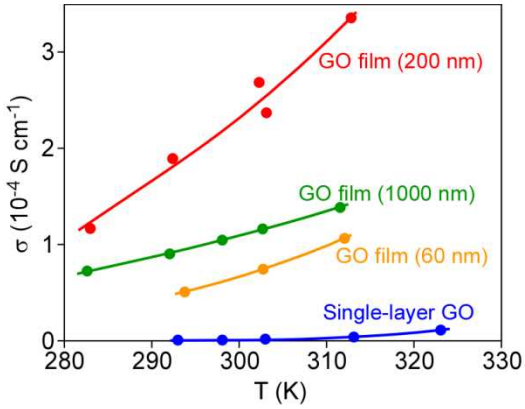

Figure 5-8. Temperature-dependent conductivities of GO films with variable thickness under 60% RH. The thicknesses of the GO films are described in parentheses.

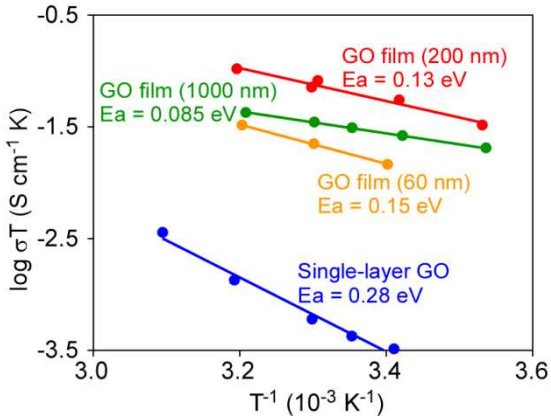

Figure 5-9. Arrhenius plots for proton conduction on the GO films under 60% RH. The thicknesses of the GO films are described in parentheses.

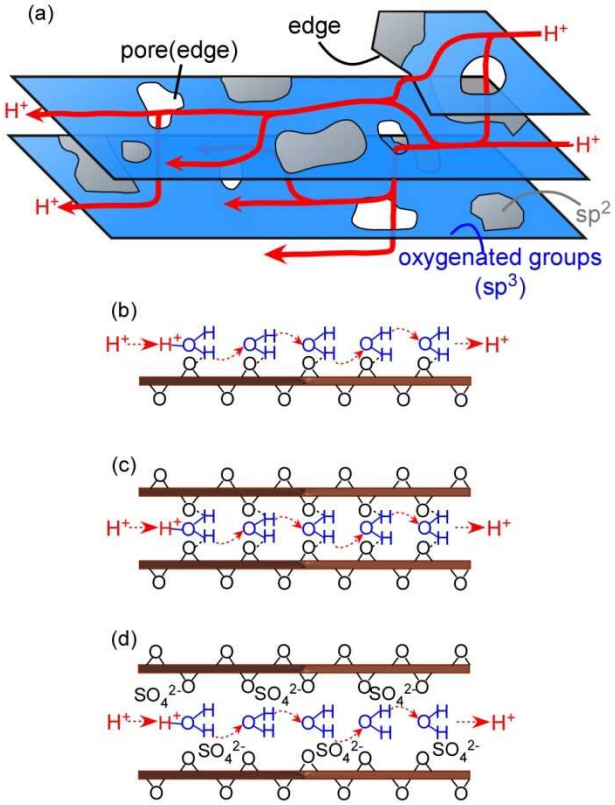

Figure 5-10. Perspective mechanism for proton conduction in single-layer GO, multilayer GO films, and sGO. (a) In multilayer assembly proton have the option to change the conduction track from one layer to the surrounding layers through numerous nanopores. The sp^3 oxygenated group, and sp^2 areas are denoted by blue, and gray colors, respectively. (b), and (c) Proton conduction supported by single and double GO walls. (d) Location of sulfate ions at the interlayer and, proton mobility via H_3O^+ networks in sGO film.

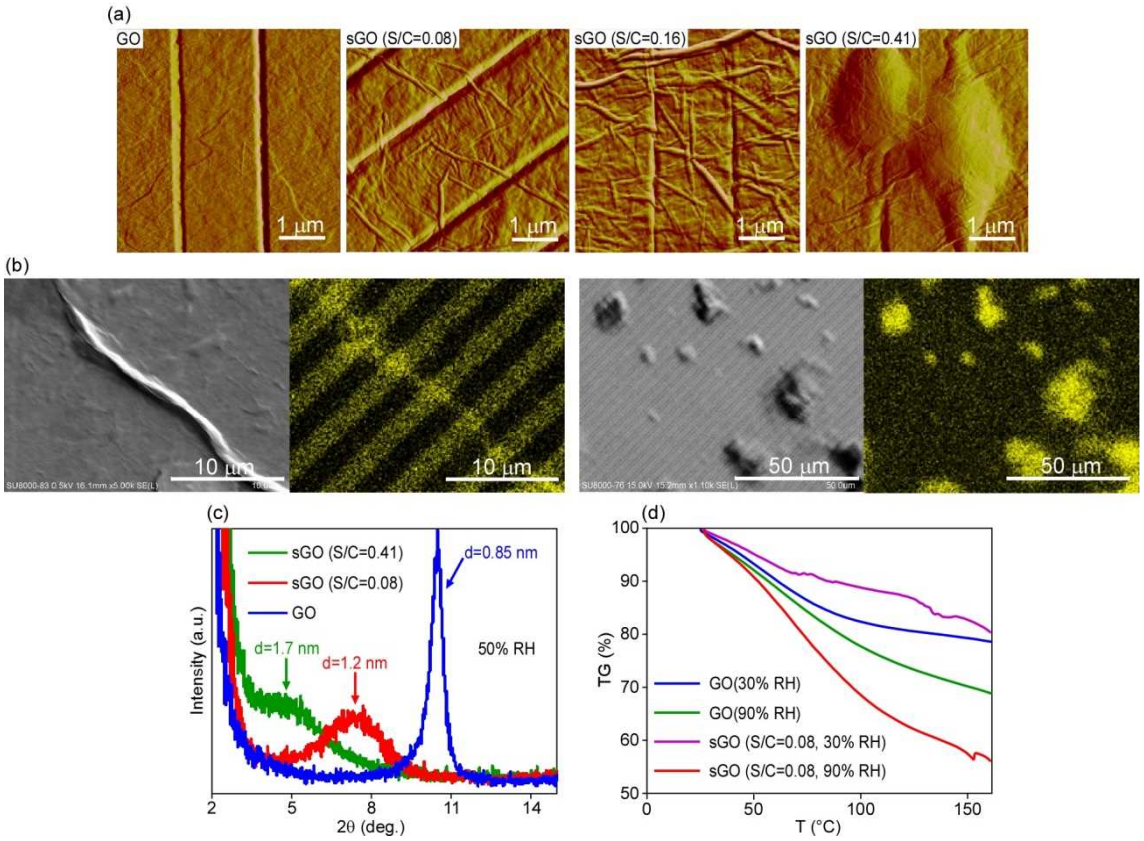

Figure 5-11. (a) AFM images of multilayer GO, and sGO films on the comb electrode surfaces (S / C atomic ratios of the sGO are described in parentheses). (b) SEM, and EDS sulfur atom mapping images of sGO (S / C=0.41). Sulfate (SO_4^{2-}) is concentrated in the veins, and hills. (c) XRD patterns of multilayer GO, and sGO films under 50% RH (S / C atomic ratios of the sGO films are described in parentheses) (d) Weight losses due to the release of the intercalated water of GO (18 μm), and sGO (S/C=0.08) samples. Before measurement the samples were incubated under 30, and 90% RH.

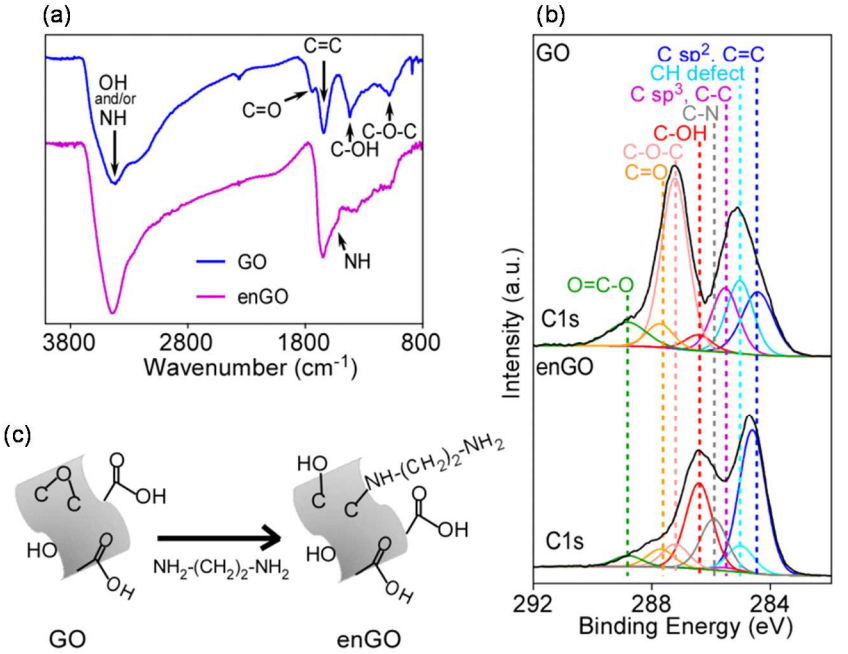

(d)

	Relative intensity of functional groups (at%)				
	C-OH	C-O-C	C=O	O=C-O	O/(C+O)
GO	3.5	37.4	5.2	7.4	30.6
enGO	23.6	6.4	4.9	3.2	19

Figure 5-12. (a) FTIR, (b**)** XPS spectra. (c) schematic of the reaction between ethylenediamine and GO. (d) Relative amount of various oxygenated functional groups in GO and enGO. The FTIR and XPS results show that the amount of the epoxide groups in GO have decreased after reaction with ethylenediamine.

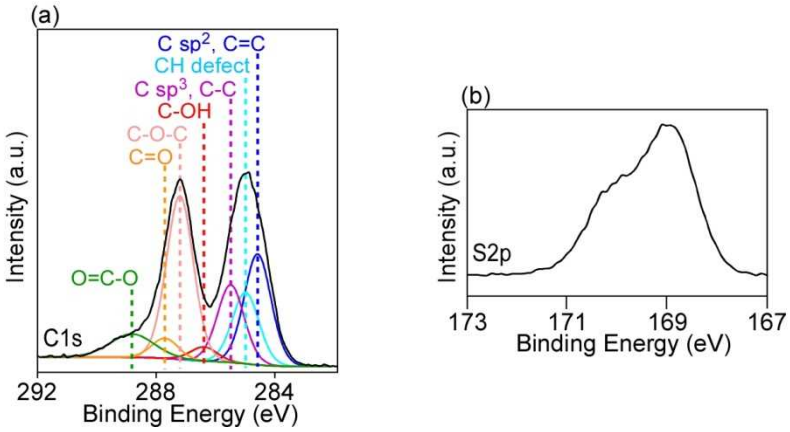

Figure 5-13. XPS spectra of C1s and S2p of the sGO film (S / C = 0.08). The peak around 169 eV corresponds to sulfate ion[43].

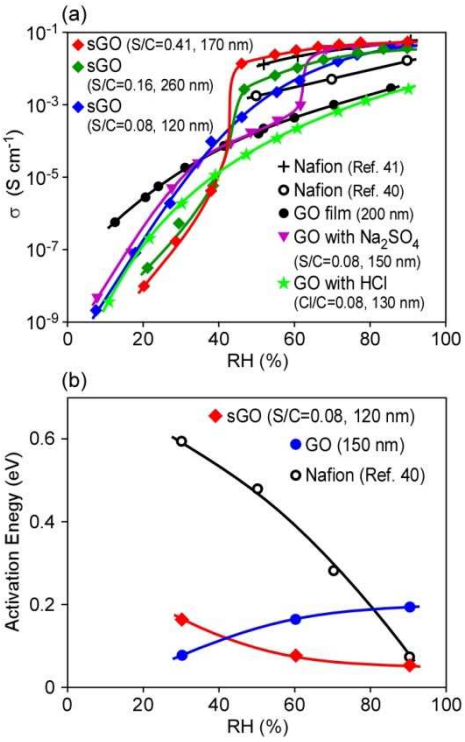

Figure 5-14. Proton conductivities of the multilayer GO films loaded by H_2SO_4, Na_2SO_4, and HCl at 25 °C (conductivities of the multilayer GO film at 25 °C, and Nafion at 30 °C are displayed for comparison). (a) Dependence of proton conductivities on RH (film thicknesses, and S / C atomic ratios of the sGO films are described in parentheses). (b) dependence of the E_a values on RH (film thicknesses S / C atomic ratios of the sGO films are described in parentheses).

Chapter 6

Tunable Graphene Oxide Proton / Electron Mixed Conductor that Function at Room Temperature

6.1. Introduction

Several interesting results regarding molecule- and ion-selective transport have been reported for multilayered graphene oxide (GO) films[1-6]. The high proton conductivity of GO is one of its most attractive properties due to its unique proton conduction mechanism, which involves the movement of protons via epoxide groups through nanofluidic channels in the interlayers, its strong dependence on the film thickness[6-8], and the fact that it makes GO suitable as a solid-state electrolyte for various types of batteries[9-12] and supercapacitors[13, 14]. In practical applications, GO is superior to Nafion when used as a solid electrolyte because it is inexpensive and easily fabricated[15]. For fuel cells, the ability of GO paper to also serve as a gas barrier is an additionally important property, because it prevents the crossover of O_2 and H_2[2, 3, 16]. With respect to the proton conduction mechanism of GO, epoxide groups that exist in the interlayers of GO films have been proved to be important for proton transport[7, 17]. However, this unique mechanism for proton conduction in GO films may be unsuitable when GO is used as an electrolyte under reducing conditions because the epoxide groups are readily decomposed under these conditions[18]. On the other hand, the reduction (to produce reduced GO (rGO)) induces in-plane electron conduction (or hole, but electron instead of hole is assumed in this paper for the conduction except for proton conduction) through the GO nanosheets[15]. The probable rough relationship between the proton and electron conductivities of GO are shown in Figure 6-1, where the mixed conductor area is also indicated. Based on this data, a clear understanding of how the proton and electron conductivity change during the reduction process is needed to enable the use of GO films as hydrogen separation membranes, solid-state electrolytes, and / or electrode materials, which are very important potential applications for GO[2, 3, 13, 19].

When both the electronic and protonic conductivities are relatively high, materials can function as excellent mixed conductors with properties that are very useful for H_2 separation or purification membranes[20, 21] and electrodes for electrochemical devices, such as fuel cells and supercapacitors[22, 23]. In general, the latter devices are operated at <150 °C. There are several metal oxides, such as perovskite-type and related oxides with electron and proton mixed conduction properties, but these materials only function at a high temperature (>250 °C)[20, 21, 24]. For example, the proton conductivity of tungsten bronze was $<10^{-12}$ Scm^{-1} when both the electron and proton conductivities were measured at room temperature[25].

A few studies have been reported regarding proton and electron mixed conductors with relatively high conductivities that have functioned at room temperature[26-28]. However, these materials consist of heterogeneous mixtures of electron and proton conductors. Considering the

electron conductor / electrolyte (proton conductor) interface at the electrode surface in an aqueous solution, molecular, and/or nano-level interactions are ideal, because a very high electrode surface is obtained at the interface. In addition, the uniform molecular and / or nano-level interactions that occur in electrodes based on single components, but not mixtures, are also preferable for H_2 separation and purification membranes because many molecular and / or nano-level pathways for the electrons and protons that are necessary for H_2 transformation are created without the occurrence of gas crossover. Thus, single-component conductors, rather than mixtures of electron and proton conductors, are highly preferable as electrodes and membranes.

Reduced graphene oxide (rGO) with an appropriate reduction degree should be a very suitable single-component mixed conductor if high protonic and electronic conductivities with nearly the same values can be achieved. In fact, the ability of rGO to function as a supercapacitor electrode with high capacitance[14, 29, 30] suggests that it should be a good mixed conductor. However, the protonic and electronic conductivities of rGO with various degrees of oxidation (or reduction) are yet to be simultaneously measured.

In this chapter, photo and thermal methods for the reduction of GO were selected because the degree of reduction could be readily controlled by varying the irradiation time and temperature, respectively. Both the protonic and electronic conductivities of GO and rGO samples prepared via photo and thermal reduction were measured. As a result, the most suitable level of reduction for rGO with mixed conductivity was demonstrated. In addition, the conduction mechanisms were investigated.

6.2. Experiment

A GO dispersion with a concentration of 0.8 mg / mL was prepared via the modified Hummers' method[31] and using the exfoliation process described previous chapters. A comb electrode (width: 2 μm, interval: 2 μm, 65 pairs; BAS Ltd.; Figure 6-2a) for the AC and DC measurements and the GO dispersion was dropped onto and dried on the comb electrode (Figure 6-2a). The samples for the X-ray photoelectron spectroscopy (XPS), Fourier transform infrared spectroscopy (FT-IR) and X-ray diffraction (XRD) measurements were prepared via the same process on a glass substrate. The ^{13}C solid-state nuclear magnetic resonance (SSNMR) samples were prepared by filtering the GO dispersion using a membrane filter (0.4 μm pore size, Merck Millipore) under reduced pressure. Photoreduction of the samples was performed using a 500 W high-pressure mercury lamp (USHIO, SX-U1501HQ) in air. Thermal reduction of the samples was performed using an incubator (ESPEC, SH-221) from 70 °C to 150 °C for 1 h at RH = 100%. The morphology and thickness of the samples on the comb electrodes were evaluated via atomic force microscopy (AFM; Bruker, Digital Instruments Nanoscope V; Figure 6-2c and e). The layer distances in the samples were measured via XRD (Rigaku, RINT2500) using Cu Kα (λ = 0.154 nm) radiation with scanning from 3 ° to 20 °.

The oxygenated functional groups (COC, C=O, COH, and COOH) and non-oxygenated functional groups (sp^3 C–C, C-H defect, and sp^2 C=C bonds) in the GO films were analyzed via XPS (Thermo Scientific, Sigma Probe). The FT-IR data were recorded by an FT-IR spectrometer (Perkin-Elmer, Frontier IR / FIR) with KBr pellets. The ^{13}C SSNMR analyses were performed with an NMR spectrometer (Varian; Unity INOVA-400). A GO sample of 50 mg mixed with ZrO_2 powder was spun at 4000 Hz in 7 mm double-bearing ZrO_2 rotors. The AC impedances of the GO films were measured using an impedance / gain phase analyzer (Solartron 1260) in the frequency range from 1 MHz to 1 Hz using a perturbation voltage amplitude of 50 mV. The DC resistances were measured via the two-probe DC method using a potentiostat with a function generator (IVIUM TECHNOLOGIES, CompactStat). The conductivities (σ) were calculated using the formula $\sigma = L / (R \times T \times D)$, where L is the film width corresponding to the distance between the two electrodes (2×10^{-4} cm), R is the AC impedance calculated from the Cole–Cole plot or DC resistance measured using the two-probe DC method, and T is the thickness of the GO film obtained from the AFM height profile (Figure 6-2c and e), D is the film length between the two electrodes calculated from charge-coupled device camera images (Figure 6-21b and d). Figure 6-2f shows where L, T, and D are located for a GO film on the comb electrode. The details regarding the calculation of conductivity were described in chapter 5. The proton conductivities were calculated using the formula $\sigma_{total} = \sigma_{proton} + \sigma_{electron}$, where σ_{total} is the total conductivity (electron (or hole) and proton conductivities) determined from the AC measurements, σ_{proton} is the proton conductivity, and $\sigma_{electron}$ is the electron conductivity determined from the DC measurements. The DC conductivities ($\sigma_{electron}$) were independent of the RH (Figure 6-14), indicating that the electron conductivities were measured without any contribution from the proton conductivities.

6.3. Results and Discussion

Figure 6-3a presents typical C1s XPS spectra of GO films before and after photoreduction in air. Figure 6-3b shows the content of each oxygenated group and the O atm% of the GO films (O / (C + O)) as a function of the irradiation time. The deconvolution of the present XPS spectra, consisting of COC, C=O, COH, COOH, sp^3 C–C, C–H defect, and sp^2 C=C bonds was made following the procedure proposed in our paper[32] and by Balog *et al.* (especially for the C–H)[33]. The presence of C–H for the rGO prepared by photoreduction is proved by FT-IR analysis (Figure 6-4). The O atm% and content of the epoxide groups generally decreased during photoreduction, whereas those of the hydroxide and carboxylic groups slightly increased with increasing irradiation time. Figure 6-3c depicts the behavior of the concentration of the C–C and C–H defects (which correspond to the C–H bonds at the edges of pores and on the graphene-like domain plane) and C=C bonds as a function of the irradiation time. Notably, the concentration of C–H defects, rather than that of the C=C bonds, increased during the reduction process. This result is similar to that obtained for

electrochemical reduction[32]. The layer distances in the GO films calculated from the diffraction peaks in the XRD patterns (Figure 6-5) decreased with increasing irradiation time due to the decrease in the oxygenated groups' content (Figure 6-3d). Moreover, the broadening of the diffraction peaks upon photoreduction (Figure 6-5) suggested that the layer distances became nonuniform. Thus, the degree of reduction, the composition, and the morphology of GO films were carefully controlled by varying the irradiation time.

Typical the C1s XPS spectra of GO films after thermal reduction at various temperatures and a relative humidity (RH) of 100% can be seen in Figure 6-6a, while the content of each oxygenated group and the O atm% of the GO films (O / (C + O)) are plotted as a function of the reduction temperature in Figure 6-6b. Again, the O atm% and content of the epoxide groups decreased during the reduction process, particularly above 100 °C, and the other oxygenated group's concentration remained nearly constant. The results of the FT-IR (Figure 6-4) and ^{13}C SSNMR (Figure 6-7) analyses are in agreement with those of the XPS spectra. Figure 6-6c presents a plot of the concentration of C–C and C–H defects and C=C bonds as a function of the reduction temperature. Notably, unlike with photoreduction, the concentration of C=C bonds increased during the thermal reduction process. The layer distances in the GO films calculated from the diffraction peaks in the XRD patterns (Figure 6-8) decreased as the reduction temperature increased, once again due to the decrease in the oxygenated groups' content (Figure 6-6d). The sharp diffraction peaks observed after thermal reduction indicated that the layer distances were relatively uniform, unlike in the case of the photoreduced GO. Thus, the degree of reduction of GO films, i.e., their composition and morphology, were also carefully controlled by varying the reduction temperature. Furthermore, the main products in the rGO films prepared via photo and thermal reduction were C–H defects and C=C π-conjugated bonds, respectively. The formation of C–H defects is thought to result in nonuniform layer distances in rGO prepared via photoirradiation, while C=C bond formation leads to uniform layer distances owing to the π interactions between the layers (vide infra).

Representative Cole–Cole plots obtained for various GO films photoreduced at different times are shown in Figure 6-9a. From theses plots, the total conductivity (electron and proton) was determined. The proton conductivity was then obtained by the subtraction of the electron conductivity from the total conductivity. Note that the conductivities obtained from the Cole–Cole plots were largely based on the proton conductivities, except for the near value regions (mixed conduction regions) for both the proton and electron conductivities (see the comparison between parts a and b in Figure 6-10 and 6-11). The electron conductivities were easily measured using the two-probe DC method (Figure 6-12) and were found to be independent of the relative humidity thus indicating no contribution of the proton conductivity (vide infra). On the other hand, the proton conductivities calculated using the above method strongly depended on the RH. The proton conductivities of the photoreduced GO films as a function of the RH percentage are shown in Figure

6-9b. Here, while the proton conductivity clearly decreased after the reduction process, the activation energy (E_a) for proton conductivity scarcely changed (~0.08–0.12 eV), as observed in the Arrhenius plots shown in Figure 6-9c. This result suggests that the proton transport speed is constant in both the GO and rGO films[34]. Consequently, the low proton conductivity of rGO is due to a decrease in the number of proton moving sites in the rGO. As chapter 5, proton conduction in GO is largely attributed to the presence of epoxide groups in the interlayers that act as proton moving sites[7, 17]. The proton conductivity as a function of the epoxide groups' concentration is shown in Figure 6-9d, and it can be clearly seen that the proton conductivity decreased with decreasing epoxide content.

The same plots as presented in Figure 6-9 and those for the thermally reduced GO films are shown in Figure 6-13. Here, the proton conductivity decreased following thermal reduction, and for the films reduced at the same temperature, the proton conductivity strongly depended on the RH (Figure 6-13b). In addition, the conductivity decreased with a decrease in the epoxide content (Figure 6-13d). However, the E_a for proton conductivity in the rGO films prepared via thermal reduction (~0.13–0.14 eV) were slightly higher than those for the rGO films prepared via photoreduction.

The electron and proton conductivities as a function of irradiation time are shown in Figure 6-14a. In contrast to the proton conductivities, the electron conductivities were independent of RH and increased with increasing irradiation time. The same values for both conductivities were ~6×10^{-5} and 2×10^{-6} Scm^{-1} at RH = 90% and 40%, respectively. At this point, mixed conduction could occur. Figure 6-14b presents the electron and proton conductivities for the thermally reduced films as a function of the reduction temperature. The proton and electron conductivities again decreased and increased following reduction, respectively. As a matter of course, the measured electron conductivity was again independent of RH. The same values for both conductivities were ~5×10^{-5} and 9×10^{-8} Scm^{-1} at RH = 90% and 40%, respectively. These values were smaller than those for the photoreduced GO films, particularly at RH = 40%. Consequently, rGO films prepared via photoreduction at an appropriate irradiation time have the optimum properties for mixed conductor films.

To investigate the conduction mechanisms, the relationships between the conductivities, oxygen content, and layer distances were evaluated. Figure 6-15a shows the conductivities as a function of the oxygen content in the GO and rGO. The electron conductivity increased with decreasing oxygen content showing good linearity when the logarithm of the conductivity was plotted against the oxygen content (%) and was independent of the reduction method. This result indicates that both the C–H defects (photoreduction) and C=C bonds (thermal reduction) produced in the rGO equally and importantly contributed to the electron conductivity. The contribution of the C–H defects is counterintuitive because only C=C π-conjugated bonds are believed to facilitate electron conduction. However, similar results have been observed for electrochemical reduction[32].

Theoretical studies are necessary to fully elucidate the electron conduction mechanism in this type of rGO with C–H defects. On the other hand, the proton conductivities were always higher for the rGO films prepared via photoreduction than those for the rGO films prepared via thermal reduction. This difference can be explained by the differences in the layer distances in the two types of rGO films, as discussed below.

The proton conductivity is plotted as a function of the layer distance in the GO or rGO films in Figure 6-15b. A good linear relationship between the logarithm of the conductivity and the layer distance was observed, independent of the reduction method. This result indicates that the layer distance as well as the epoxide content strongly influences proton conduction. The relationship between the layer distance and the oxygen content is also shown in Figure 6-15c although the main contributors to the oxygen content are the epoxide oxygen atoms. The layer distances in the rGO films prepared via photoreduction were always larger than those prepared via thermal reduction (Figure 6-15c). This result is obvious given that the main products formed during thermal reduction of GO films are C=C π-conjugated domains (Figure 6-6c) that participate in strong π interactions between the layers in the rGO films, resulting in shorter interlayer distances. On the other hand, the C–H defects formed during the photoreduction of GO films (Figure 6-3c) can only participate in relatively weak interactions between the layers, resulting in a relatively large interlayer space in the resultant rGO films compared to that in thermally reduced GO films. The larger interlayer distances in the rGO films prepared via photoreduction afford higher proton conduction compared to those of rGO films that are prepared via thermal reduction and thus lead to higher mixed conductivities, as shown in Figure 6-14. The larger space in the photoirradiated rGO films provides flexibility for the movement of water molecules attached to the epoxides, resulting in higher proton conduction. In fact, the activation energies for the rGO films prepared via photoreduction were always lower than those for the rGO films prepared via thermal reduction, as stated previously (Figure 6-9c and 6-13c).

The proton and electron mixed conductor described herein is the first mixed conductor consisting of a single component that functions at room temperature. Moreover, the literature contains no reports on the ready tunability of the mixed proton and electron conductivities of rGO by varied preparation conditions. Thus, the rGO prepared here exhibited unique conductivity properties. Such a mixed proton and electron conductor should be very useful as an electrode material for electrochemical devices that use aqueous solutions because it enables the fabrication of electrodes with very large surface areas that can form nano- and/or molecular-level interactions with proton-containing solutions. Photoreduction for ~3 h was found to be the most suitable method for the preparation of mixed-conducting rGO films; both the electron and proton conductivities were $\sim 10^{-4}$ Scm^{-1} at 90% RH for the rGO film prepared using this irradiation time. This value corresponds to a resistance of 100 Ω when the rGO film was ~1 μm thick; therefore, an ~1 μm-thick rGO film can be used as an electrode for fuel cells and supercapacitors if the current densities are

below ~10^2 mA cm^{-2} and the IR drop is less than ~0.1 V. An rGO electrode with much lower resistance, i.e., a superior electrode with mixed proton–electron conductivity, can be fabricated if the thickness of the film is less than ~1 μm.

In practical applications of this mixed conductor as an electrode, suitable conditions are limited to high humidity and from room temperature to 150 °C, because the mixed conductivity is low under low humidity conditions, as shown in Figure 6-14, and proton conduction will decrease at higher temperatures due to the degree of high reduction that causes a decrease in the epoxide content. Therefore, it can be useful in applications such as the electrodes in a polymer electrolyte fuel cell (PEFC) and a supercapacitor using aqueous electrolytes that operate under the above conditions; however, it cannot be used under harsh conditions such as high temperatures. Due to its relatively high mixed conductivity even at room temperature, this mixed conductor can also be used as a purification film for separating H_2 from mixed gases comprising H_2 content if the above conditions are satisfied. This is a superior aspect of this mixed conductor, since high temperatures (>250 °C) are usually necessary for similar operations with metal oxides[20, 21, 24] due to their very low mixed conductivity at room temperature.

6.4. Conclusions

In summary, we measured both the proton and electron conductivities and other properties of rGO films subjected to photo and thermal reduction. The proton conductivity decreased with irradiation time and reduction temperature due to a decrease in the oxygenated groups' concentration, particularly epoxide groups, which act as proton moving sites. The interlayer distance within the rGO films was also observed to affect proton conduction, with larger spaces promoting proton movement. As a result, the proton conductivities of the rGO films prepared via photoreduction were higher than those of the rGO films prepared via thermal reduction, leading to higher mixed conductivities for the photoreduced films. On the other hand, the electronic conductivity increased with irradiation time and reduction temperature due to an increase in the concentration of C–H defects and C=C bonds, as well as a decrease in the oxygen content. The rGO films prepared via reduction, using an appropriate irradiation time or temperature, were thus good mixed conductors with both proton and electron conductivities under high RH conditions. For the photoreduction conditions used in this study, both the proton and electron conductivities of the rGO film prepared using an irradiation time of 3 h were ~10^{-4} Scm^{-1} at 90% RH. This rGO sample with good mixed conductivity has excellent potential for use as fuel cell and supercapacitor electrodes as well as H_2 separation and/or purification membranes that can function at room temperature.

References

1. Joshi, R. K.; Carbone, P.; Wang, F. C.; Kravets, V. G.; Su, Y.; Grigorieva, I. V.; Wu, H. A.; Geim, A. K.; Nair, R. R., Precise and Ultrafast Molecular Sieving Through Graphene Oxide Membranes. *Science*, **343**, 752-754 (2014).
2. Kim, H. W.; Yoon, H. W.; Yoon, S. M.; Yoo, B. M.; Ahn, B. K.; Cho, Y. H.; Shin, H. J.; Yang, H.; Paik, U.; Kwon, S.; Choi, J. Y.; Park, H. B., Selective Gas Transport Through Few-Layered Graphene and Graphene Oxide Membranes. *Science*, **342**, 91-95 (2013).
3. Li, H.; Song, Z. N.; Zhang, X. J.; Huang, Y.; Li, S. G.; Mao, Y. T.; Ploehn, H. J.; Bao, Y.; Yu, M., Ultrathin, Molecular-Sieving Graphene Oxide Membranes for Selective Hydrogen Separation. *Science*, **342**, 95-98 (2013).
4. Sun, P. Z.; Zheng, F.; Zhu, M.; Song, Z. G.; Wang, K. L.; Zhong, M. L.; Wu, D. H.; Little, R. B.; Xu, Z. P.; Zhu, H. W., Selective Trans-Membrane Transport of Alkali and Alkaline Earth Cations through Graphene Oxide Membranes Based on Cation-π Interactions. *ACS Nano*, **8**, 850-859 (2014).
5. Sun, P. Z.; Zhu, M.; Wang, K. L.; Zhong, M. L.; Wei, J. Q.; Wu, D. H.; Xu, Z. P.; Zhu, H. W., Selective Ion Penetration of Graphene Oxide Membranes. *ACS Nano*, **7**, 428-437 (2013).
6. Raidongia, K.; Huang, J. X., Nanofluidic Ion Transport through Reconstructed Layered Materials. *J. Am. Chem. Soc.*, **134**, 16528-16531 (2012).
7. Hatakeyama, K.; Karim, R., Mohammad; Ogata, C.; Tateishi, H.; Funatsu, A.; Taniguchi, T.; Koinuma, M.; Hayami, S.; Matsumoto, Y., Proton Conductivities of Graphene Oxide Nanosheets: Shingle, Multilayer and Modified Nanosheets. *Angew. Chem., Int. Ed.*, **53**, 6997-7000 (2014).
8. Karim, M. R.; Hatakeyama, K.; Matsui, T.; Takehira, H.; Taniguchi, T.; Koinuma, M.; Matsumoto, Y.; Akutagawa, T.; Nakamura, T.; Noro, S.; Yamada, T.; Kitagawa, H.; Hayami, S., Graphene Oxide Nanosheet with High Proton Conductivity. *J. Am. Chem. Soc.*, **135**, 8097-8100 (2013).
9. Tateishi, H.; Koga, T.; Hatakeyama, K.; Funatsu, A.; Koinuma, M.; Taniguchi, T.; Matsumoto, Y., Graphene Oxide Lead Battery (GOLB). *ECS Electrochem. Lett.*, **3**, A19-A21 (2014).
10. Tateishi, H.; Hatakeyama, K.; Ogata, C.; Gezuhara, K.; Kuroda, J.; Funatsu, A.; Koinuma, M.; Taniguchi, T.; Hayami, S.; Matsumoto, Y., Graphene Oxide Fuel Cell. *J. Electrochem. Soc.*, **160**, F1175-F1178 (2013).
11. Zarrin, H.; Higgins, D.; Jun, Y.; Chen, Z. W.; Fowler, M., Functionalized Graphene Oxide Nanocomposite Membrane for Low Humidity and High Temperature Proton Exchange Membrane Fuel Cells. *J. Phys. Chem. C*, **115**, 20774-20781 (2011).
12. Ravikumar; Scott, K., Freestanding Sulfonated Graphene Oxide Paper: A New Polymer Electrolyte for Polymer Electrolyte Fuel Cells. *Chem. Commun.*, **48**, 5584-5586 (2012).

13. Gao, W.; Singh, N.; Song, L.; Liu, Z.; Reddy, A. L. M.; Ci, L.; Vajtai, R.; Zhang, Q.; Wei, B.; Ajayan, P. M., Direct Laser Writing of Micro-Supercapacitors on Hydrated Graphite Oxide Films. *Nature Nanotechnol.*, **6**, 496-500 (2011).
14. Wu, Z. S.; Parvez, K.; Feng, X. L.; Mullen, K., Graphene-Based In-Plane Micro-Supercapacitors with High Power and Energy Densities. *Nature Commun.*, **4**, 2487 (2013).
15. Pei, S. F.; Cheng, H. M., The Reduction of Graphene Oxide. *Carbon*, **50**, 3210-3228 (2012).
16. Nair, R. R.; Wu, H. A.; Jayaram, P. N.; Grigorieva, I. V.; Geim, A. K., Unimpeded Permeation of Water Through Helium-Leak-Tight Graphene-Based Membranes. *Science*, **335**, 442-444 (2012).
17. Koinuma, M.; Ogata, C.; Kamei, Y.; Hatakeyama, K.; Tateishi, H.; Watanabe, Y.; Taniguchi, T.; Gezuhara, K.; Hayami, S.; Funatsu, A.; Sakata, M.; Kuwahara, Y.; Kurihara, S.; Matsumoto, Y., Photochemical Engineering of Graphene Oxide Nanosheets. *J. Phys. Chem. C*, **116**, 19822-19827 (2012).
18. Kim, S.; Zhou, S.; Hu, Y. K.; Acik, M.; Chabal, Y. J.; Berger, C.; de Heer, W.; Bongiorno, A.; Riedo, E., Room-Temperature Metastability of Multilayer Graphene Oxide Films. *Nature Mater.*, **11**, 544-549 (2012).
19. Gao, W.; Wu, G.; Janicke, T., Michael; Cullen, A., David; Mukundan, R.; Baldwin, K., Jon; Brosha, L., Eric; Galande, C.; Ajayan, M., Galande; More, L., Karren; Dattelbaum, M., Andrew; Zelenay, P., Ozonated Graphene Oxide Film as a Proton-Exchange Membrane. *Angew. Chem., Int. Ed.*, **53**, 3588-3593 (2014).
20. Escolastico, S.; Somacescu, S.; Serra, J. M., Solid State Transport and Hydrogen Permeation in the System $Nd_{5.5}W_{1-x}Re_xO_{11.25-\delta}$. *Chem. Mater.*, **26**, 982-992 (2014).
21. Escolastico, S.; Solis, C.; Scherb, T.; Schumacher, G.; Serra, J. M., Hydrogen Separation in $La_{5.5}WO_{11.25-\delta}$ Membranes. *J. Membr. Sci.*, **444**, 276-284 (2013).
22. Tripathi, B. P.; Schieda, M.; Shahi, V. K.; Nunes, S. P., Nanostructured Membranes and Electrodes with Sulfonic Acid Functionalized Carbon Nanotubes. *J. Power Sources*, **196**, 911-919 (2011).
23. Rolison, D. R.; Hagans, P. L.; Swider, K. E.; Long, J. W., Role of Hydrous Ruthenium Oxide in Pt-Ru Direct Methanol Fuel Cell Anode Electrocatalysts: The Importance of Mixed Electron / Proton Conductivity. *Langmuir* , **15**, 774-779 (1999).
24. Wang, T. H.; Henderson, C. N.; Draskovic, T. I.; Mallouk, T. E., Synthesis, Exfoliation, and Electronic / Protonic Conductivity of the Dion-Jacobson Phase Layer Perovskite $HLa_2TiTa_2O_{10}$. *Chem. Mater.*, **26**, 898-906 (2014).
25. Huo, L. H.; Zhao, H.; Mauvy, F.; Fourcade, S.; Labrugere, C.; Pouchard, M.; Grenier, J. C., Synthesis and Mixed Conductivity of Ammonium Tungsten Bronze with Tunneling Structures. *Solid State Sci.*, **6**, 679-688 (2004).
26. Ijeri, V.; Cappelletto, L.; Bianco, S.; Tortello, M.; Spinelli, P.; Tresso, E., Nafion and Carbon

Nanotube Nanocomposites for Mixed Proton and Electron Conduction. *J. Membr. Sci.*, **363**, 265-270 (2010).

27. Swider, K. E.; Merzbacher, C. I.; Hagans, P. L.; Rolison, D. R., Synthesis of Ruthenium Dioxide Titanium Dioxide Aerogels: Redistribution of Electrical Properties on the Nanoscale. *Chem. Mater.*, **9**, 1248-1255 (1997).
28. Aragaw, B. A.; Su, W. N.; Rick, J.; Hwang, B. J., Highly Efficient Synthesis of Reduced Graphene Oxide-Nafion Nanocomposites with Strong Coupling for Enhanced Proton and Electron Conduction. *RSC Adv.*, **3**, 23212-23221 (2013).
29. Wang, Y.; Shi, Z. Q.; Huang, Y.; Ma, Y. F.; Wang, C. Y.; Chen, M. M.; Chen, Y. S., Supercapacitor Devices Based on Graphene Materials. *J. Phys. Chem. C*, **113**, 13103-13107 (2009).
30. Zhu, Y. W.; Murali, S.; Stoller, M. D.; Ganesh, K. J.; Cai, W. W.; Ferreira, P. J.; Pirkle, A.; Wallace, R. M.; Cychosz, K. A.; Thommes, M.; Su, D.; Stach, E. A.; Ruoff, R. S., Carbon-Based Supercapacitors Produced by Activation of Graphene. Science 2011, 332, 1537-1541.
31. Hummers, W. S.; Offemen, R. E., Preparation of Graphitic Oxide. *J. Am. Chem. Soc.*, 80, 1339 (1958).
32. Koinuma, M.; Tateishi, H.; Hatakeyama, K.; Miyamoto, S.; Ogata, C.; Funatsu, A.; Taniguchi, T.; Matsumoto, Y., Analysis of Reduced Graphene Oxides by X-ray Photoelectron Spectroscopy and Electrochemical Capacitance. *Chem. Lett.*, **42**, 924-926 (2013).
33. Balog, R.; Andersen, M.; Jorgensen, B.; Sljivancanin, Z.; Hammer, B.; Baraldi, A.; Larciprete, R.; Hofmann, P.; Hornekaer, L.; Lizzit, S., Controlling Hydrogenation of Graphene on Ir(111). *ACS Nano*, **7**, 3823-3832 (2013).
34. Agmon, N., The Grotthuss Mechanism. *Chem. Phys. Lett.*, **244**, 456-462 (1995).
35. Acik, M.; Lee, G.; Mattevi, C.; Pirkle, A.; Wallace, R. M.; Chhowalla, M.; Cho, K.; Chabal, Y., The Role of Oxygen during Thermal Reduction of Graphene Oxide Studied by Infrared Absorption Spectroscopy. *J. Phys. Chem. C*, **115**, 19761-19781 (2011).
36. Chu, P. K.; Li, L. H., Characterization of Amorphous and Nanocrystalline Carbon Films. *Mater. Chem. Phys.*, **96**, 253-277 (2006).
37. Wang, L.; Zhu, S. J.; Wang, H. Y.; Qu, S. N.; Zhang, Y. L.; Zhang, J. H.; Chen, Q. D.; Xu, H. L.; Han, W.; Yang, B.; Sun, H. B., Common Origin of Green Luminescence in Carbon Nanodots and Graphene Quantum Dots. *ACS Nano*, **8**, 2541-2547 (2014).
38. Qu, S. N.; Wang, X. Y.; Lu, Q. P.; Liu, X. Y.; Wang, L. J., A Biocompatible Fluorescent Ink Based on Water-Soluble Luminescent Carbon Nanodots. *Angew. Chem., Int. Ed.*, **51**, 12215-12218 (2012).
39. Zhu, S. J.; Meng, Q. N.; Wang, L.; Zhang, J. H.; Song, Y. B.; Jin, H.; Zhang, K.; Sun, H. C.; Wang, H. Y.; Yang, B., Highly Photoluminescent Carbon Dots for Multicolor Patterning, Sensors,

and Bioimaging. *Angew. Chem., Int. Ed.*, **52**, 3953-3957 (2013).

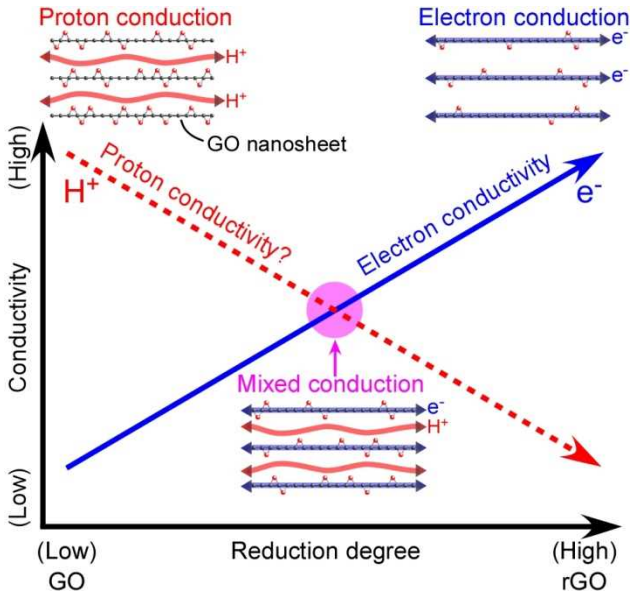

Figure 6-1. Relationships between the reduction degree and electron and proton conductivities of GO. Electron conductivity increased with increasing reduction degree. The proton conductivity likely decreases with the increasing reduction degree, however the depicted relationship is assumed, not measured.

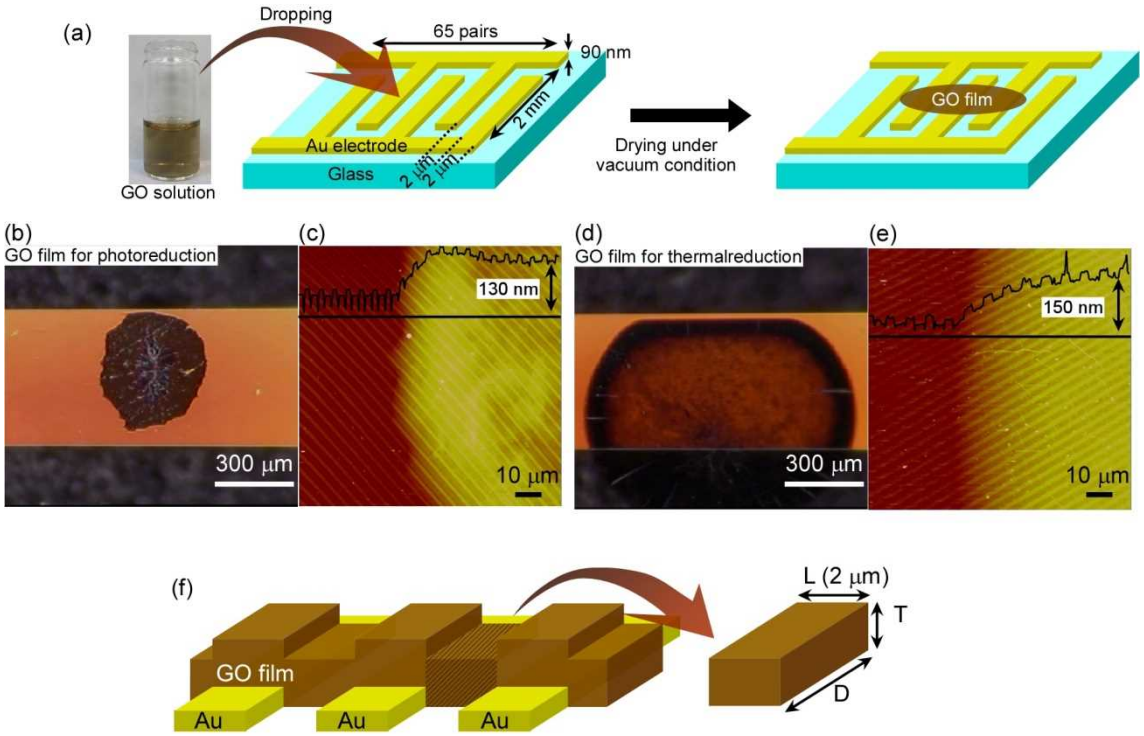

Figure 6-2. (a) Schematic illustration of the fabrication process of the GO films on comb electrodes. The comb electrode (width: 2 μm, interval: 2 μm, 65 pairs) was used for AC and DC measurement. (b) Charge-coupled device (CCD) camera image and (c) AFM image and height profile of GO film for photoreduction on comb electrode. (d) CCD camera image and (e) AFM image and height profile of GO film for thermal reduction on comb electrode. (f) Schematic of GO film on comb electrode and L, D and T (in the formula $\sigma = L / (R \times T \times D)$) positions.

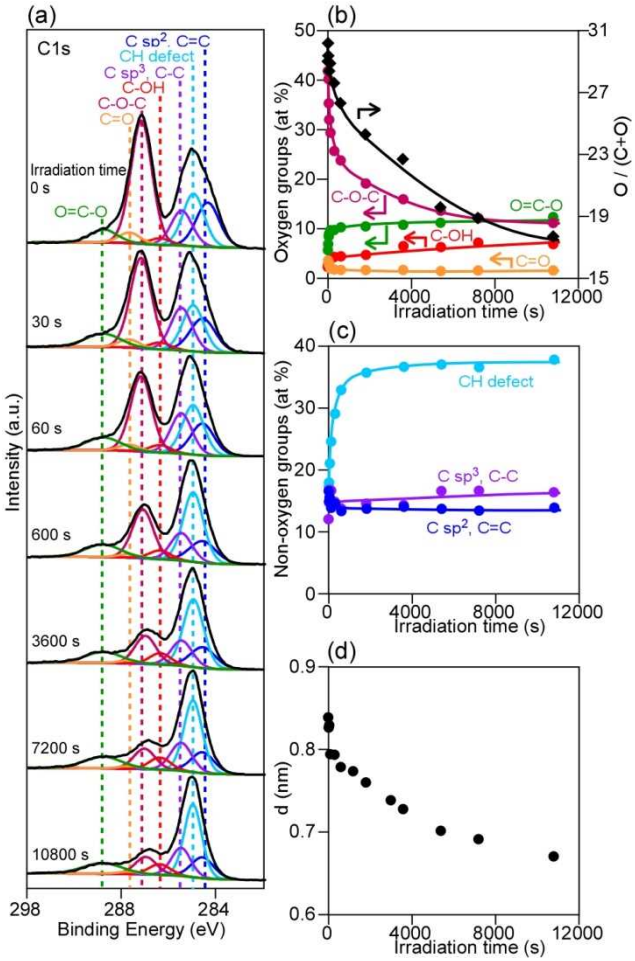

Figure 6-3. (a) C1s XPS profiles of GO films prepared at various irradiation times. Concentration of the (b) oxygenated groups and (c) non-oxygenated groups in GO films as a function of the irradiation time as determined from the C1s XPS peaks. The epoxide groups and C–H defects decreased and increased during photoreduction, respectively. (d) Layer distances in the GO films calculated from the XRD diffraction peaks (Figure 6-5) as a function of the irradiation time.

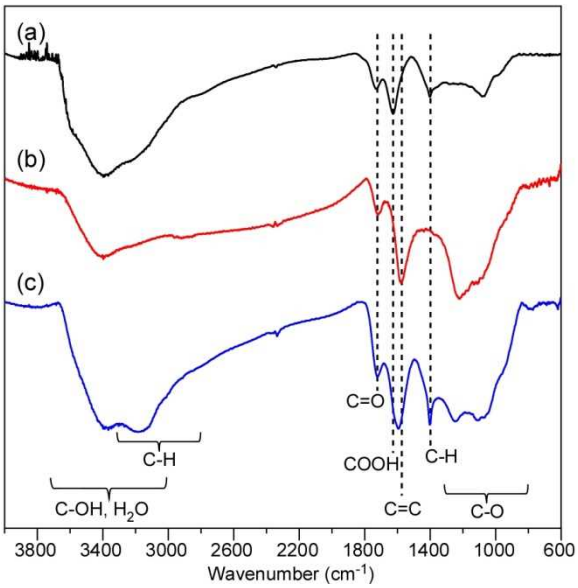

Figure 6-4. FT-IR spectra of (a) GO, (b) thermally reduced rGO (at 150 °C), and (c) photoreduced rGO (after 3 h). There are stretching vibrations of COH and H_2O at 3000–3700 cm^{-1},[35] C–H stretching at 2800–3300 cm^{-1},[36] C=O vibrations at 1750–1850 cm^{-1},[35] COOH vibrations at 1600–1750 cm^{-1},[35] in-plane stretching of C=C at 1500–1600 cm^{-1},[35] C–H bending vibrations at 1375–1480 cm^{-1},[36-39] and the C–O region (COC, COH, etc.) at 800–1330 cm^{-1}.[35] The absorption bands of 3200 cm^{-1} and 1400 cm^{-1} are based on the C–H that disappeared due to thermal reduction, but are relatively increased by the photoreduction in intensity. These results relating to C–H are in good agreement with those of the XPS analysis in Figures 6-3 and 6-6.

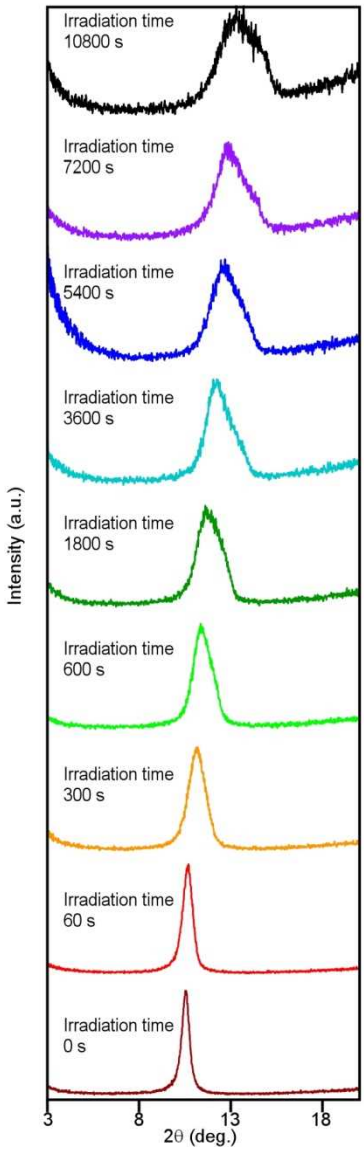

Figure 6-5. XRD patterns of the GO films prepared using various irradiation times. The diffraction peaks shifted to higher angles and broadened after the photoreduction process. The layer distances of the GO films decreased from 0.84 before photoreduction to 0.67 nm after photoreduction.

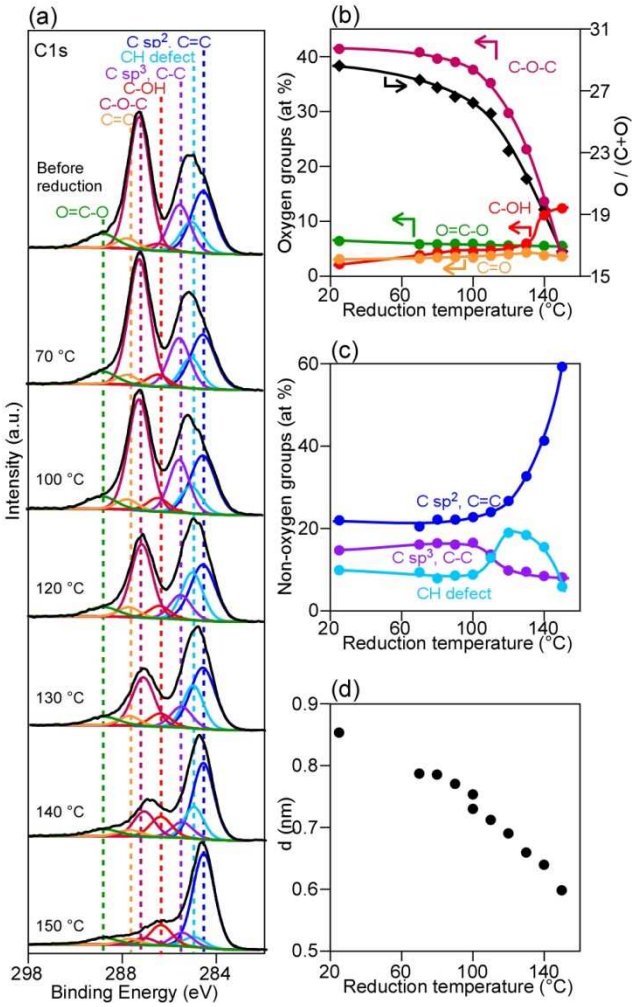

Figure 6-6. (a) C1s XPS profiles of GO films prepared at various reduction temperatures. Concentration of the (b) oxygenated groups and (c) non-oxygenated groups in the GO films as a function of the reduction temperature as determined from the C1s XPS peaks. The epoxide groups and C=C bonds decreased and increased during thermal reduction, respectively. (d) Layer distances in the GO films calculated from the XRD diffraction peaks (Figure 6-8) as a function of the reduction temperature.

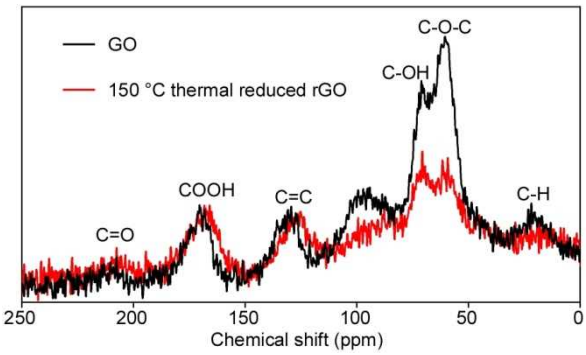

Figure 6-7. ^{13}C SSNMR spectra of GO and thermally reduced rGO. The peak intensities of COC decreased by thermal reduction. These results are in agreement with those of the XPS analysis in Figure 6-6.

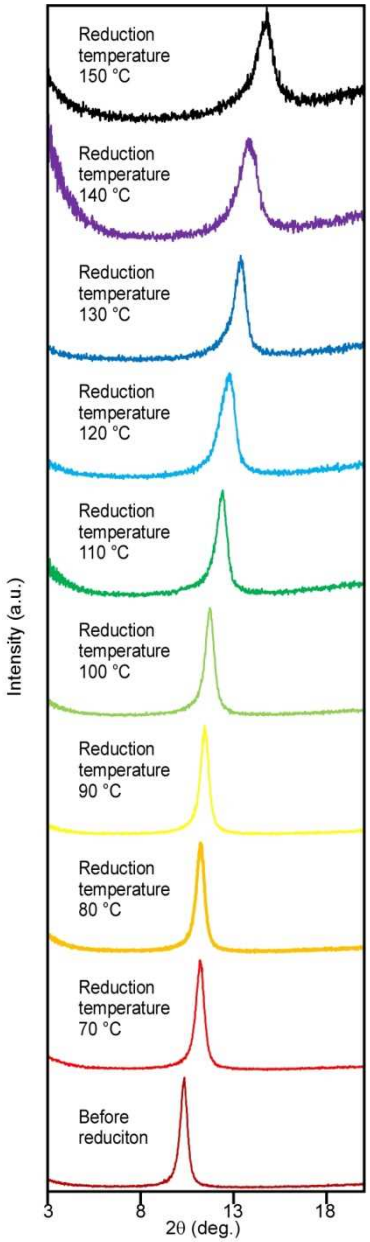

Figure 6-8. XRD patterns of the GO films prepared using various reduction temperatures. The diffraction peaks shifted to higher angles keeping sharp peaks after the thermal reduction process. The layer distances of the GO films decreased from 0.85 before thermal reduction to 0.60 nm after thermal reduction.

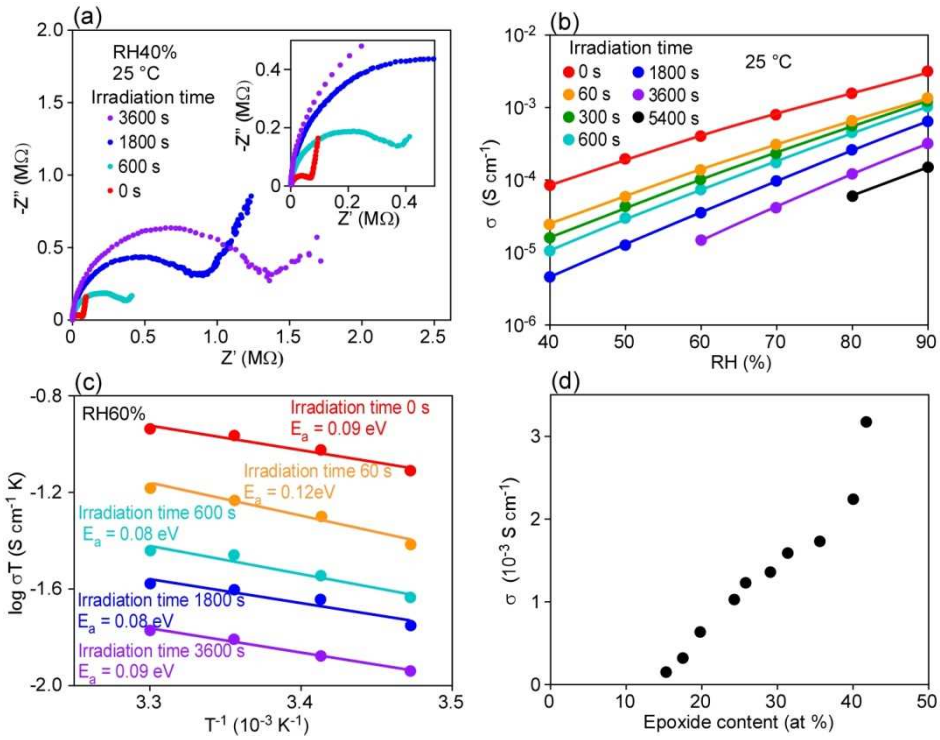

Figure 6-9. (a) Typical Cole–Cole plots of selected GO films prepared at various irradiation times. The inset shows a magnified view of the high-frequency region. (b) RH dependence of the proton conductivities of GO films prepared at various irradiation times. (c) Arrhenius plots of the proton conductivities of photoreduced GO films at 60% RH. The E_a values calculated from the Arrhenius plots are also shown. (d) Proton conductivities of photoreduced GO films as a function of the epoxide groups' concentration.

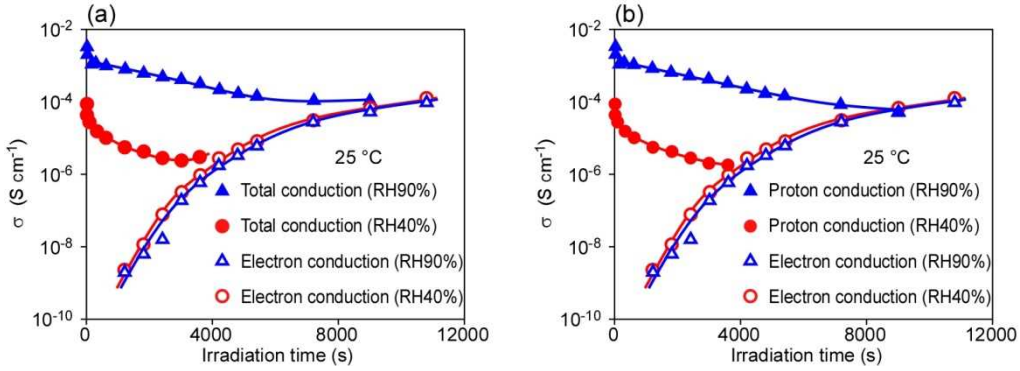

Figure 6-10. (a) Total and electron conductivities as a function of irradiation time. Total conductivities were obtained from Cole-Cole plots. (b) Proton and electron conductivities as a function of irradiation time (same as Figure 6-14a). Proton conductivities were calculated using the formula $\sigma_{total} = \sigma_{proton} + \sigma_{electron}$, where σ_{total}, σ_{proton} and $\sigma_{electron}$ are the total, proton and electron conductivities, respectively.

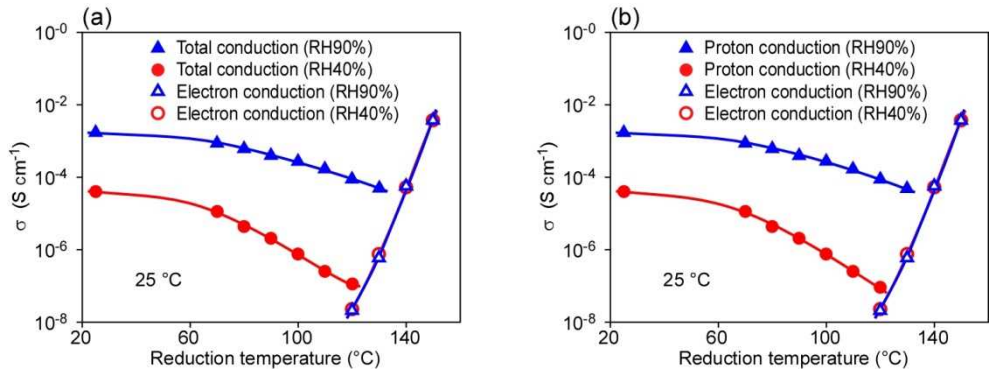

Figure 6-11. (a) Total and electron conductivities as a function of the reduction temperature. Total conductivities were obtained from Cole-Cole plots. (b) Proton and electron conductivities as a function of the reduction temperature (same as Figure 6-14b). Proton conductivities were calculated using the formula $\sigma_{total} = \sigma_{proton} + \sigma_{electron}$.

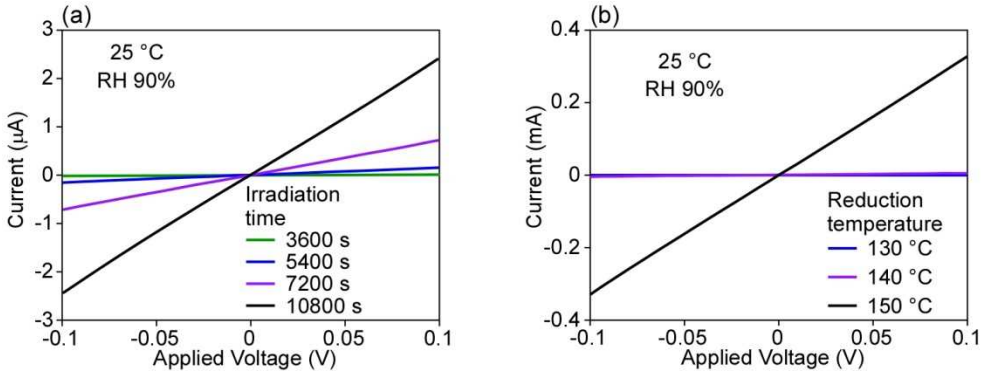

Figure 6-12. Typical *I-V* curves of (a) photo and (b) thermally reduced rGO films obtained by a two-probe DC method. The linear relationships between *I* and *V*, and independent on RH (Figure 6-10 and 6-11) indicate the obtained resistances are based on only the electron conductivity.

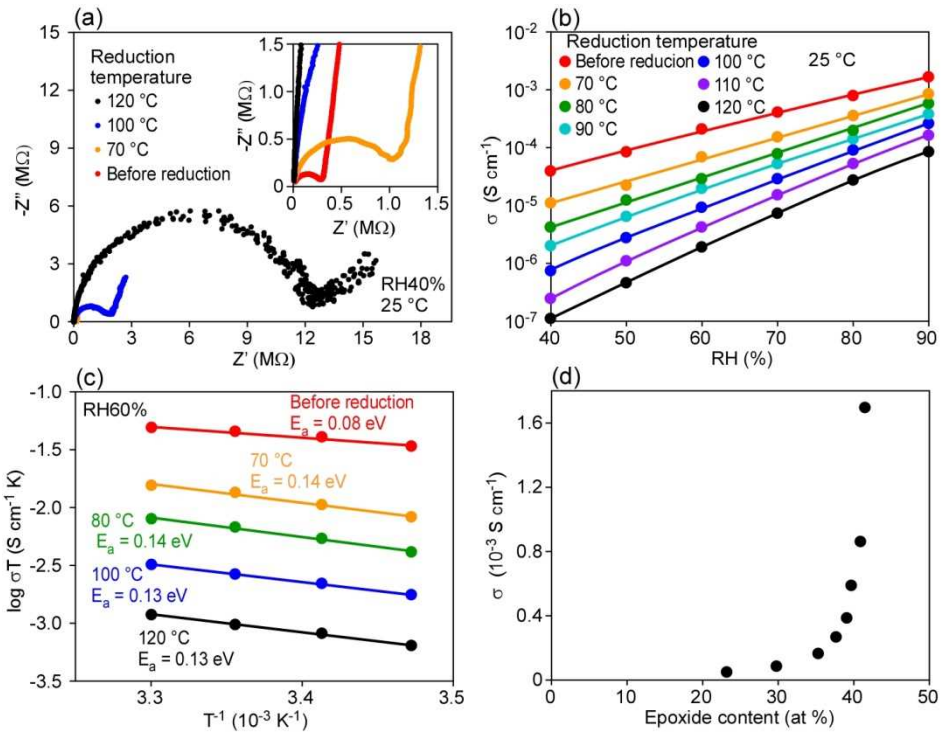

Figure 6-13. (a) Typical Cole–Cole plots of some GO films prepared at various reduction temperatures. The inset shows a magnified view of the high-frequency region. (b) RH dependence of the proton conductivities of GO films prepared at various reduction temperatures. (c) Arrhenius plots of the proton conductivities of thermally reduced GO films at 60% RH. The E_a values calculated from the Arrhenius plots are also shown. (d) Proton conductivities of thermally reduced GO films as a function epoxide groups' concentration.

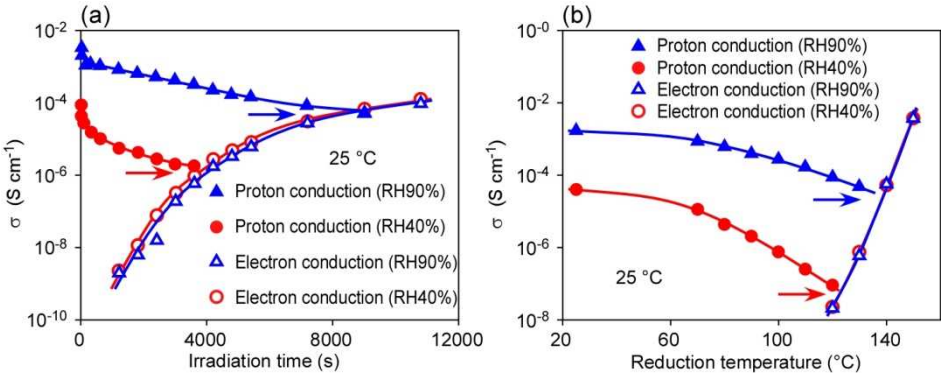

Figure 6-14. Proton and electron conductivities as a function of the (a) irradiation time and (b) reduction temperature at 40% and 90% RH. The electron conductivities drastically increased with increasing irradiation time and reduction temperature, independent of the RH; in contrast, the proton conductivities decreased with increasing irradiation time and reduction temperature, largely dependent on the RH.

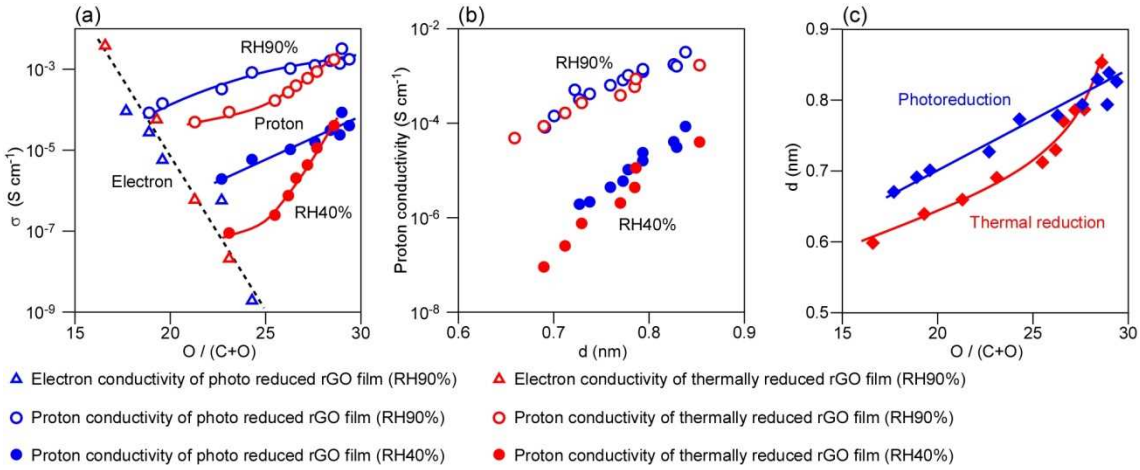

Figure 6-15. (a) Proton (90% and 40% RH) and electron (90% RH) conductivities as a function of the oxygen content. (b) Proton conductivities (90% and 40% RH) as a function of the layer distance. (c) Layer distance as a function of the oxygen content.

Chapter 7

Conclusions

In this thesis, we researched the photoreaction and proton conduction of graphene oxide and reported that GO has a lot of interesting properties ahead of the world. The summary of each chapter is described as follows.

Chapter 1

Introduction

In this chapter, the general background, physical and chemical properties, and synthesis of GO were demonstrated.

Chapter 2

Simple Photoreduction of Graphene Oxide Nanosheet under Mild Conditions

GO were reduced by UV irradiation in H_2 or N_2 under mild conditions (at room temperature) without a photocatalyst. Photoreduction proceeded even in an aqueous suspension of nanosheets. The GO nanosheets reduced by this method were analyzed by XPS and Raman spectroscopy. It was found that epoxy groups attached to the interiors of aromatic domains of the GO nanosheet were destroyed during UV irradiation to form relatively large sp^2 islands resulting in a high conductivity. *I-V* curves were measured by conductive atomic force microscopy (AFM; perpendicular to a single nanosheet) and a two-electrode system (parallel to the nanosheet). They revealed that photoreduced GO nanosheets have high conductivities, whereas non-reduced GO nanosheets are nearly insulating. Ag^+ adsorbed on GO nanosheets promoted the photoreduction. This photoreduction method was very useful for photopatterning a conducting section of micrometer size on insulating GO. The developed photoreduction process based on a photoreaction will extend the applications of GO to many fields because it can be performed in mild conditions without a photocatalyst.

Chapter 3

Photoreaction of Graphene Oxide Nanosheets in Water

In this chapter, we reported new photoreactions similar to photocatalytic reactions in which H_2 and CO_2 are evolved from an aqueous suspension of GO nanosheets under UV irradiation; these reactions are based on the photoreactions of oxygen-containing functional groups and carbon. As a result, rGO nanosheets with many holes and defects were produced. We conjectured that some carbons in the holes belonged to zigzag edges, CH bonds, or both and that the rGO nanosheets therefore had ferromagnetic properties. In photoelectrochemical measurements of a GO nanosheet

electrode, a large anodic photocurrent was generated by the CO_2 evolution reaction and a small cathodic photocurrent was generated by reduction of oxygen-containing functional groups and the H_2 evolution reaction. The mechanism of the photoreaction between GO nanosheets and water was also discussed in terms of band energy levels estimated from experimental results.

Chapter 4

Photochemical Engineering of Graphene Oxide Nanosheets

In this chapter, the photoreaction process was demonstrated to be very useful to control the oxygenated functional groups and morphologies of GO. We reported the fast, simple production of nanopores in porous GO via photoreaction in O_2 under UV irradiation at room temperature. Quantitative analysis using XPS showed that nanopores were produced in areas of oxygenated groups (sp^3 carbon bonds), creating porous rGO. The photoreaction mechanism was proposed on the basis of changes in the number of oxygenated groups. Proton conduction occurred at the basal plane of epoxide groups in virgin GO, even at low humidity, and at carboxyl groups for porous rGO at high humidity. Thus, GO and rGO samples with various morphologies, oxygenated functional groups, and conduction types can be easily fabricated by controlling the photoreaction conditions.

Chapter 5

Proton Conduction of Graphene Oxide

In this chapter, we showed high proton conductivities in bundles of parallelly assembled GO walled cavities. The conductivities of multilayer GO films (assembled by drop-cast method) were larger than single-layer (assembled by both the drop-cast method, and Langmuir-Blodgett film) by several orders, meaning that protons move more easily in the interlayers than the surfaces. At 60% RH, the σ value increased from 1×10^{-6} Scm^{-1} in single-layer GO nanosheet to 1×10^{-4}, and 4×10^{-4} Scm^{-1} for 60, and 200 nm thick multilayer films, respectively. The conductivity suffered a sudden fall (7×10^{-6} Scm^{-1} at 60% RH) in ethylenediamine modified GO where the epoxy groups of GO was engaged in chemical bond formation with ethylenediamine. This observation confirms the epoxide group as the major contributor in proton transportation mechanism. The conductivity was possible to maximize by loading H_2SO_4 into the GO walled cavities (sGO). At 25 °C, the conductivity of sGO ($\approx 10^{-1}$ Scm^{-1}) was found to exceed that of Nafion. The gradual increase in conductivity was supposed to result from the increment in water content, and improved hydration dynamics due to the layer by layer assembly of conduction channels, and loading of hydrophilic precursors.

Chapter 6

Tunable Graphene Oxide Proton / Electron Mixed Conductor that Function at Room Temperature

In this chapter, we reported the successful control of the proton and electron conductivities of GO using the photoirradiation and thermal reduction processes. The proton conductivity decreased when the epoxide content and layer distance decreased, whereas the electron conductivity drastically increased with decreasing oxygen content. Both the electron and proton conduction mechanisms for GO were discussed based on the concentrations of various functional groups and defects, changes in the interlayer distance, and the activation energy associated with proton conduction. We also determined the most suitable degree of reduction for obtaining a good mixed conductor useful as an electrode material and a hydrogen separation membrane that functions at room temperature.